Optimization and Model-predictive Control for Overload Mitigation in Resilient Power Systems

by

Mads R. Almassalkhi

A dissertation submitted in partial fulfillment
of the requirements for the degree of
Doctor of Philosophy
(Electrical Engineering: Systems)
in The University of Michigan
2013

Doctoral Committee:

>Professor Ian Hiskens, Chair
>Professor Göran Andersson, ETH Zürich
>Professor Amy Ellen Mainville Cohn
>Professor Heath Hofmann
>Professor Jing Sun

To my mother and father, who taught me the value of education.

ACKNOWLEDGEMENTS

TABLE OF CONTENTS

LIST OF FIGURES

LIST OF TABLES

LIST OF APPENDICES

Appendix

LIST OF ABBREVIATIONS

AC   Alternating current

ACSR   Aluminum conductor steel reinforced

AGC   Automatic generation control

AIMD   Additive increase and multiplicative decrease

AMI   Advanced metering infrastructure

CHP   Combined heat and power

CUP   Central utility plant

DC   Direct current

ED   Economic dispatch

ES   Energy storage

FACTS   Flexible AC transmission system

GSF   Generation shift factor

IPT   In-phase transformer

ISO   Independent System Operator

LMP   Locational marginal pricing

LP   Linear programming

MIDM   Mixed-integer disjunctive model

MIL   Mixed-integer linear

MILP   Mixed-integer linear programming

MIP   Mixed-integer programming

MIQP   Mixed-integer quadratic programming

MP	Multi-period
MPC	Model-predictive control
MPMIQP	Multi-period mixed-integer quadratic programming
MPODF	Multi-period optimal dispatch formulation
NEMESS	Network model of energy-services supply systems
NLP	Non-linear programming
PCT	Programmable communicating thermostat
PEV	Plug-in electric vehicle
PST	Phase-shifting transformer
PTDF	Power transfer distribution factor
PWL	Piece-wise linear
QP	Quadratic programming
RHMPC	Receding-horizon model-predictive control
RTS	Reliability test system
SHMPC	Shrinking-horizon model-predictive control
SOC	State-of-charge
STE	Short-term emergency
TCL	Thermostatically-controlled load
TCT	Tap-changing transformer
TES	Thermal energy storage
TLR	Transmission load relief
UC	Unit commitment
VERA	Versatile energy resource allocation

ABSTRACT

Optimization and Model-predictive Control for Overload Mitigation in Resilient
Power Systems
by
Mads R. Almassalkhi

Chair: Ian A. Hiskens

The National Academy of Engineering named the electric power grid the greatest
engineering achievement of the 20th century. However, as recent large-scale power
grid failures illustrate, the (electro-mechanical) electric grid is being operated closer
and closer to its limits. Specifically, the electric grid of the 20th century is aging
and congested. Due to the protracted and cost-intensive nature of upgrading energy
infrastructures, major research initiatives are now underway to improve the utility
of the existing infrastructure. One important topic is contingency management. Ac-
cordingly, this dissertation comprises of practical, yet rigorously justified, feedback
control algorithms that are suitable for power system contingency management. The
main goals of the algorithms are to prevent or mitigate overloads on network elements
(e.g. lines and transformers).

   In this dissertation, a coupling of energy infrastructures is examined as a method
for improving system reliability and a simple cascade mitigation approach highlights
the role of model-predictive control and energy storage in improving system response
to severe disturbances (e.g. line outages). The ideas of balancing economic and safety
criteria are developed and implemented with a receding-horizon model-predictive con-
troller (RHMPC) for electric transmission systems with energy storage and renew-
ables. The novel RHMPC scheme employs a lossy "DC" power flow model and is
proven to alleviate conductor temperature overloads and returns the system to an
economically optimal state. Finally, an incentive-based distributed predictive-control
algorithm is developed to prevent overloads in the distribution network caused by
overnight charging of PEVs. In addition, Matlab-based simulations are included to
illustrate the performance and behavior of all proposed overload mitigation schemes.
The automatic schemes presented in this dissertation are, essentially, "closing the
loop" in contingency management, and will help bring the electric power grid into
the 21st century.

CHAPTER I

Introduction

1.1 Motivation & Overview

"In the 20th century, widespread electrification gave us power for our cities, factories, farms, and homes - and forever changed our lives. Thousands of engineers made it happen, with innovative work in fuel sources, power generating techniques, and transmission grids. From street lights to supercomputers, electric power makes our lives safer, healthier, and more convenient."

The National Academy of Engineering (quoted above) named the electric power grid the greatest engineering achievement of the 20th century [3]. However, as recent large-scale power grid failures illustrate, the (electro-mechanical) electric grid is being operated closer and closer to its limits. Specifically, the electric grid of the 20th century is aging and congested. Furthermore, it will not be able to meet future demands without operational changes and significant capital investments over the next decades [4]. Thus, the electric grid of the 21st century represents an open problem for the research community and industry. With the development of new technologies, such as, flexible AC transmission devices (FACTS), phasor measurement units (PMUs), renewable and distributed generation, flexible loads, and energy storage solutions, the tools are available to enable a paradigm shift for the electric grid (and general energy delivery systems).

To overcome the limitations of today's power grid, two main approaches are considered by engineers and scientists. The first approach investigates improvements to energy-delivery systems subject to boundary conditions given by today's grid structures. The second approach seeks to develop and design a new paradigm for optimal future energy delivery systems, which takes into account novel emerging technologies. By treating the second approach (i.e. the greenfield approach) as the forecasted optimal 'target' system, the first approach can be considered a coordinated effort to bridge today's aging and congested system with the optimal future target system, as Figure 1.1 illustrates.

The design and development of the greenfield approach can be considered the long-term goal of power systems engineers and scientists, while the bridging approach can
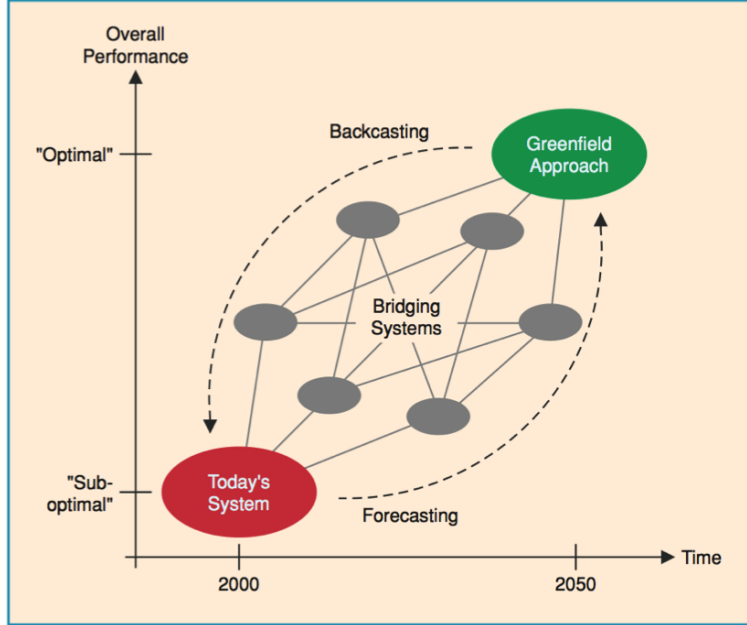
Figure 1.1: Designing a future greenfield approach allows us to move from today's aging and congested power system to the future optimal system. Figure is borrowed from [1]

be considered a series of short-term projects. It is within this framework that we focus our research. Namely, we build upon the ETH Zürich project "Vision for Future Energy Networks," which focused on a synergistic interconnected energy systems model as their greenfield approach. To accomplish the interconnection of energy systems, the ETH project developed tools such as the 'energy hub' and multi-energy carriers and analyzed many scenarios under the new multi-energy context, see [1, 5, 6].

This dissertation expands upon the ETH project by designing a standardized format to describe general energy hub systems and developing optimization tools to automatically and quickly analyze the performance of interconnected energy delivery systems (i.e. the greenfield systems). These tools enable formulation of a novel model-predictive control scheme that ensures efficient operation of energy systems and mitigates the effects of severe disturbances through automated control. In addition, the research described herein extends beyond the long-term goals of the greenfield systems and also tackles short-term problems associated with the effects of uncoordinated charging of plug-in electric vehicles (PEVs) on today's distribution networks. The coordinated charging scheme is achieved within a non-centralized model-predictive control framework.

Our interdisciplinary research lies at the intersection of power systems, optimization, and controls and the following sections discuss related work from literature on the different topics.

2

1.2 Background & Related Work

1.2.1 Energy Hubs

> *"An energy hub generally represents an interface between energy producers, consumers, and the transportation infrastructure. From a system point of view, an energy hub provides the functions of input and output, conversion, and storage of multiple-energy carriers."* [7]

The energy hub can be viewed as a generalization of a node in an electric network and is modeled as a multi-input/multi-output black-box where energy enters, is stored, and exits according to well-defined conversion and storage processes. As illustrated by Figures 1.2a and 1.2b, it is straightforward to model physical energy processes and storage devices with the energy hub formulation. For example, in Figure 1.2a, natural gas and electricity are inputs to the hub. Electricity flows into the (futuristic) heat-recovery enabled power transformer, which converts high-voltage electricity to low-voltage electricity at some loss. In addition, a heat-recovery mechanism can capture transformer heat and transport it to district heating loads or inject into thermal energy storage. Natural gas is dispatched to a furnace or a combined heat and power plant (CHP) to generate a mix of steam for district heating and electricity depending on available energy and customer demand. In Figure 1.2b, we model a wind-generating turbine with local hydrogen storage, where the turbine converts wind energy to electric energy which can be converted to and stored as hydrogen. The hydrogen storage device can be charged via electrolysis and discharged with fuel cells, which allows an operator to mitigate the intermittency inherent to wind energy. The energy hub modeling framework is a flexible and powerful tool that enables a plethora of combinations of energy storage and conversion processes.

(a) Combined heat and power plant with heat-recovery transformer

(b) Wind turbine with hydrogen storage
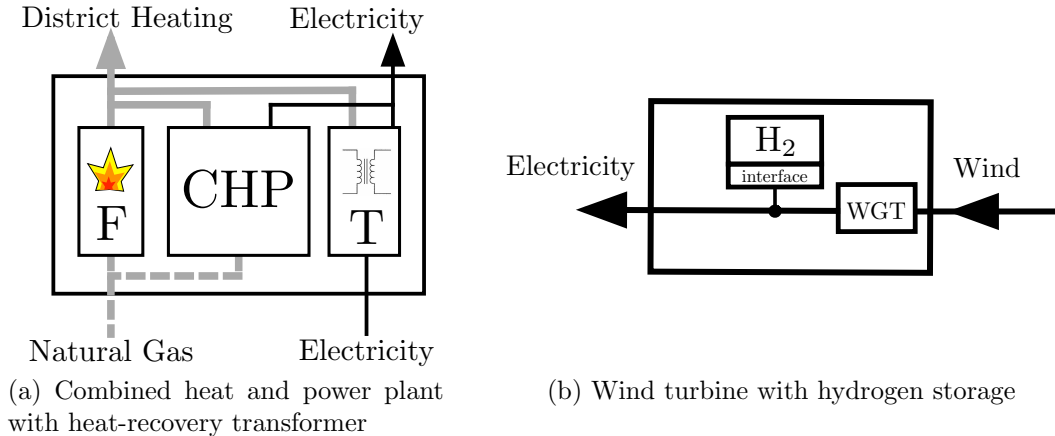
Figure 1.2: Simple examples of energy hub models of physical systems.

The first example of a steady-state multi-input/multi-output energy process model appeared in 1989, see [8], in the analysis and optimization of exergy in industrial energy settings. Their work focused on calculating energy losses from steady-state material flows by thermodynamic analysis. Then in 1995, the same authors applied

data-flow network models to formalize their work within a model framework called NEMESS (NEtwork Model of Energy-services Supply Systems) [9]. NEMESS aided in the decision-making process for developing regional energy systems by allowing for analysis and optimization of various combinations of energy objectives. Their framework simplified the notion of power flows by considering all flows as simple network flows with no physical dependencies between network elements (such as electric voltage, phase angle, and natural gas pipeline pressure) and considered only losses between energy interfaces. This simplification of power flows limited the ability to analyze multiple energy carrier networks. To this effect, authors in [10, 11, 12] proposed optimization schemes for multiple energy carrier networks including relevant physical network parameters. Independently, the authors developed a combined natural gas and electric optimal power flow (GEOPF) to investigate the coupling of energy systems through gas-powered electric generator costs. Their work illustrated that coupling energy carriers may reveal minimum cost solutions, and also vulnerabilities, that are not apparent when each energy system is treated separately. In [12], the author included storage devices and renewable generation and eventually called his energy-services systems planning framework "eTransport" [13].

The flexible and general framework proposed by NEMESS and the GEOPF tools were combined and further improved by Andersson's group project "Vision for Future Energy Networks" at ETH Zürich, see [5, 14, 15], to explicitly model the couplings and interactions between different energy infrastructures. This resulted in a general modeling and optimization framework based on the concept of the "Energy Hub." The ETH group expanded the application-base of the energy hub via numerous publications in the areas of power market economics [16], distributed predictive control [17, 18, 19], and plug-in electric vehicles [20]. In addition, energy hub concepts can be applied within the micro-grid and central energy plant context for planning and optimization purposes as in [6]. Finally, the same group developed a new version of the energy hub, the 'Power Node,' which is designed to emphasize the modeling of storage devices within a power network context [21]. For a general overview of the energy hub formulation, see [22].

The main short-coming in the energy hub literature has been the absence of implementation and analysis of large-scale energy hub systems (i.e. 100's to 1000's of energy hubs). In the literature, the systems of interest have largely represented 3-4 hub systems, as the focus of the work has been more on the hub formulation rather than on large-scale network implications. Also, implementation of even a small network of interconnected energy hubs has proven rather tedious due to the coding effort needed to set up the energy hub system. Furthermore, once a system is implemented, making relatively small changes to the network topology can involve time-consuming revisions of the code. In fact, a genuine need was identified by [23] for developing tools that implement and simulate large-scale coupled energy systems. The best tools available for simulating multiple energy carrier systems focus on small-scale networks where a drag-and-drop interface allows users to manually construct energy-hub networks using blocks and connector lines, such as "eTransport" [13] and Honeywell's "VERA" (Versatile Energy Resource Allocation) [24].

To that effect, this work has developed tools for automatically constructing and

simulating optimal economic operation of arbitrarily large systems of general energy hubs. To accomplish this, a succinct ASCII-based text format is developed, which contains the information necessary to fully describe the energy hub system (i.e. elements and interconnections) and then interfaces with Matlab and optimization libraries to perform required simulations. This has allowed us to investigate systems with hundreds of energy hubs and analyze the use of energy storage for cascade mitigation, for example. Further details of our work with energy hubs is provided in Chapter III.

1.2.2 Combinatorial Optimization & Reliability in Power Systems

"Operating reliability is the ability of the electric system to withstand sudden disturbances such as electric short circuits or unanticipated loss of system components." - North American Electric Reliability Corporation

Mathematical optimization has held a significant role within the power systems community. For example, the power systems community has utilized linear, non-linear, and mixed-integer programming tools for analyzing various Optimal Power Flow problems [25]. The objectives of the Optimal Power Flow problems generally take one of these forms: minimize active power losses or minimize active power generation fuel cost. The Optimal Power Flow problem generally ensures some measure of reliable and secure operation by taking into account the (AC or DC) power flow equations and network element limits (e.g. voltages and transmission line flows stay within some acceptable region), see [26, 27].

However, large blackouts are often the result of an unexpected exogenous disturbance (e.g. a storm), which initially disables only a small number of transmission lines but develops into a system-wide collapse. In the canonical August 14, 2003, blackout of the U.S. and Canada, it was merely three transmission lines, which tripped within 40 minutes of one another that initiated the blackout process [28]. Thus, to avoid severe blackouts, it is necessary to ensure that the system is in a secure state even if a small set of elements undergo failure. This leads to the concept of $N - k$ security, which ensures that no element is overloaded in case of a k-element failure, where N is the number of network elements (e.g. buses, lines, and/or generators). Determining which k-combination failures of elements cause overloads in the network is usually accomplished via exhaustive enumerations of all one-element (N-1) and, for smaller networks, two-element (N-2) failures. However, for $k > 1$ and a practicable network, the combinatorial nature of this problem renders the enumeration approach intractable. On the other hand, for k large enough, it becomes relatively simple to find a combination of k-element failures which cause a system-wide blackout. Therefore, the interesting failures are related to sets of elements with cardinality $k \in \{2, 3, 4, 5\}$. To this effect, [29] employed DC power flows and a bilevel optimization framework (via a Global Bender's Decomposition) with mixed-integer programming (MIP) to solve an electric power grid interdiction problem. In their work, an adversary is essentially given the means to disable k lines that would maximize long-term post-contingency costs to operators. The method scales well but only allows large networks to be investigated for the worst-case attacks. In [30, 31], a similar but more general

adversarial approach is formulated as a linear mixed-integer program that explicitly models a 'game' between a fictional attacker seeking to disable the network, and a controller who tries to prevent a collapse by selecting which generators to operate and adjusting generator outputs and demand levels. In addition, their work proposes a continuous nonlinear programming formulation which compactly captures the interaction between the underlying physics and the network structure. The nonlinear formulation models an adversary who can modify reactances on transmission lines to approximate the effect of the $N - k$ problem and cause overloaded lines. Within their optimization framework, the authors can handle models an order of magnitude larger than those previously. Taking advantage of network structure and power flow physics is also highlighted by authors in [32], who apply structural properties of feasible solutions to a nonlinear mixed-integer $N - k$ flow problem to develop a simple mixed-integer linear programming (MILP) problem. This simplified problem finds the minimal number of lines to disable (i.e. k) to partition a network into generation-rich and load-rich regions, which are interconnected via insufficient capacity (i.e. interdicts the load-rich region). While this method employs powerful mathematical tools and can handle larger problems than generic MIP techniques, it only approximates the $N - k$ problem, which results in successful attacks on the network that are larger than necessary.

While the above works focus on vulnerability *detection*, there is also a body of literature on network reinforcement problem (i.e. vulnerability *prevention*). In these problems there is a fixed set of fault scenarios and in each scenario a subset of edges is deleted. The objective is to selectively add to the capacity of existing power lines, so that in every possible fault scenario the resulting failure cascade is immediately arrested (i.e. no further outages). In [33], the authors propose a DC power flow reinforcement problem that sustains a given set of scenarios via minimum-cost reinforcement of the network. Their work constitutes a conservative model, but with the advantage that it can be tackled using standard MILP optimization techniques. Furthermore, [33] extends and adapts a dynamic transmission blackout model developed by [34], but do not require that each potential cascade be immediately stopped. Instead, the authors in [33] allow rounds of cascading failures to occur and require only that the network *eventually* becomes stabilized without incurring a large loss of demand. That is, they assume no control action is taken during cascade and seek a reinforcement plan that can passively ride out cascades produced by a given set of scenarios.

The above description of literature highlights the difficulty of solving the $N - k$ problem. There is an astronomically large number of contingencies that could theoretically arise, but only a very small fraction of those are both realistic and capable of causing a catastrophic cascade. In fact, the above methodologies either find a salient subset of critical outages, the smallest interdiction that leads to a large loss of load, or the worst-case performance of the grid given a fixed number of lines to disable. In the vernacular sense, these methods are searching for a needle in a haystack. That is, the computation of a non-conservative *a-priori* robust control algorithm that can respond well to *all* potentially damaging faults becomes non-trivial (intractable). However, if we now assume the initial fault has already taken place, the uncertainty surrounding

the initial fault and its immediate consequence has been revealed. One can, thus, devise a meaningful control algorithm - 'on the fly' - that takes advantage of the particular nature of the fault contingency. In our work, we employ a post-disturbance model-predictive controller to mitigate effects of disturbances in the electric grid and prevent cascading failures.

1.2.3 Model-predictive control in Power Systems

Currently, abnormal conditions are handled either through operator intervention or protectionoperation, depending onthe severity ofthe abnormality. In the former case, where conditions do not immediately threaten the integrity of plant or loads, operators institute corrective procedures that may include altering generation schedules, adjusting transformer tap positions, and switching capacitors/reactors. For more extreme abnormalities, the protection associated with vulnerable components will operate to ensure they do not suffer damage. This myopic response may, however, weaken the network, exacerbating the conditions experienced by other components. They may subsequently trip, initiating an uncontrolled cascade of outages. This pattern was exhibited during the blackout of the U.S. and Canada in August 2003.

As the amount, type and distribution of controllable resources increases, operators will find it even more difficult to determine an appropriate response to unanticipated events. At a minimum, operators will require new tools to guide their decision-making. Given the increased complexity of response actions, a closed-loop feedback process will become indispensable. Model predictive control (MPC) schemes can be particularly useful within this context. MPC was originally developed by the chemical process industry as a tool to optimize the operation of multivariable processes. The following steps describe the basic notion behind MPC:

1. Determine a control schedule that optimizes a cost criterion over a prediction window.

2. Apply this profile until new process measurements become available.

3. When new measurements are available, repeat step (1).

For a technical treatment and overview of MPC, we refer the reader to [2, 35, 36, 37, 38]. Within the context of power systems, model-predictive control can be traced back to static linear programming and sensitivity techniques for voltage control [39, 40]. In [41], the authors employed sensitivity techniques to determine a clustering algorithm to implement local control of active and reactive power injections, voltage, and load-shedding to alleviate overloads. A dynamic multi-period open-loop optimization problem with a model of thermal overload capacity is developed in [42] to compute the necessary rescheduling of active power generation (against ramp-rate limits) and load-shedding to alleviate thermal line overloads. In [43], the authors propose a heuristic feedback algorithm that is a compromise between the static and dynamic optimization mentioned above. The instantaneous control is determined by a static optimization and updated by feedback which continuously varies the performance index in order

to take into account the dynamic constraints. The real-time controller dynamically allocates generation ramping to alleviate line overloads, and the solution retains the basic features of the computationally taxing multi-period open-loop problem above.

The first application of standard MPC to emergency control of power systems can be found in [44], where voltage stability was achieved through optimal coordination of load shedding, capacitator switching, and tap-changer operation. A tree-based search method is employed to obtain optimal control actions from discrete switching events. To circumvent tree-based search methods, authors in [45, 46, 47] employ trajectory sensitivities to develop MPC for voltage stability. However, these methods focus on voltage stability and do not take into account thermal overloads of transmission lines.

The authors in [48, 49] propose electrothermal coordination in power systems and develop predictive temperature-based iterative algorithms that are amenable to day-ahead markets and employ temperature-dependent resistance values in the power flow. Recent work, see [50, 51], on model-predictive contingency operation of electrical energy systems includes an explicit thermal conductor model. Specifically, the authors in [51] extend the ideas of [50] to include a linearized current-based thermal model of conductors and a auto-regressive model of the weather conditions near transmission lines (i.e. wind speed and ambient temperature). This allows [51] to set a hard upper limit on conductor temperature to ensure control objectives and allows the controller to operate the system closer to actual physical limits than if using standard (worst-case weather-based) conductor flow limits. However, under modeling and measurement uncertainties, the hard limit constraint on temperature can cause infeasibility and subsequent instabilities in the cascade mitigation scheme, which can lower performance of the controller significantly. Furthermore, the highlighted works utilize a linearization of I^2R-based losses, which underestimates losses and may not capture temperature-current relationship properly. Of course, due to the absence of a truly centralized operator in large-scale power networks and the natural nonlinearities of actual power systems, distributed MPC is likely required for tractable computational and realistic communication purposes, see [52, 53, 54].

The work presented herein differentiates itself from literature by developing a novel linear DC-based MPC-based contingency management scheme that combines and balances economical and security objectives via a bilevel hierarchical control framework that considers energy storage and renewables. Specifically, a convex relaxation is applied to the AC power flow to develop a piece-wise linear formulation for line losses, which is proven to be sufficient to enable MPC to drive line temperatures below limits. The work herein is shown to alleviate temperature overloads with minimal load shedding by taking advantage of the temporal nature of conductor temperatures and energy storage devices. In addition, the formulation enables utilization of energy storage for overcoming generation ramp-rate limiting constraints. Further details of the model-predictive cascade mitigation scheme is provided in Chapter IV.

1.2.4 Distributed Optimization and Control in Power Systems

The previous discussions have centered on optimization and control techniques for large-scale transmission systems, where an operator can utilize generator ramp-

8

ing, load control, and other grid-controlled elements to achieve various security or economical objectives. However, with the emergence and installment of new technologies, such as advanced metering infrastructure (AMI) and programmable communicating thermostats (PCTs), operators will have the ability to control energy-intensive consumer loads, such as plug-in electric vehicles (PEVs) and thermostatically controlled loads (TCLs), by manipulating local set points rather than directly interrupting power (i.e. direct load control and load shedding). Therefore, this dissertation also develops a model-predictive load-control scheme that is amenable to distribution networks for overload prevention of transformers. This is particularly pertinent as an increased market-penetration of PEVs and uncoordinated overnight-charging can significantly overload distribution-level transformers and cause local blackouts.

For a general background on load control, we refer the reader to [55, 56]. Some of the first PEV load control schemes provided by the literature rely on centralized open-loop scheduling and direct manipulation of PEV charging rates by the network utilities, see [57, 58]. Such approaches typically suffer from a significant need for communication, excessive computational burdens, and robustness issues, however. Other work on PEV scheduling focuses on hierarchical control as a possible means of decreasing complexity [59]. Therein, the distribution-level transformers are treated as static network elements with a given power rating (i.e., a fixed capacity) and the dynamical relationship between transformer loading and winding temperature is ignored. However, perhaps even more problematic than the associated computational complexity, utility-controlled charging may be impractical as PEV owners could be reluctant to relinquish the control of their vehicles to some centralized operator, and they might be unwilling to cooperate with each other if this could affect their own charging performance. Therefore, distributed optimization and control schemes should be pursued. To this effect, PEV owners in [60] and [61] are considered autonomous entities whose actions can only be influenced by providing them with incentives (i.e., a time-varying electricity price) for a certain behavior. A key assumption in [60] is that the PEVs are price takers: individually, their strategies have no significant effect on the aggregate power demand and price. The so-obtained coordinated scheduling scheme lets each vehicle effectively react to the average charging strategy of the total (infinitely large) PEV population and establishes a Nash-optimal, valley-filling net charging profile by encouraging additional charging whenever background demand is low. While [61] achieves the valley-filling effect with any number of PEVs, both [61] and [60] employ utility-centric objectives that essentially sacrifice PEV-owner convenience and access to grid to ensure that the network capacity is minimally utilized over the charging period. Recent work by the authors in [62] employs the internet congestion regulating algorithm AIMD (Additive Increase / Multiplicative Decrease) to design a distributed charging algorithm for arbitrary PEV populations. Rather than utilizing price signals to induce behavioral changes, as in the case of [60, 61], they utilize a PEV-centric objective to enhance owner experience.

Our interests align with the PEV-centric objective of [62], however, in contrast to the above methods, we explicitly account for the substation transformer's thermal limits and dynamics in computing our control actions. Moreover, because prediction errors and fluctuations in background demand can be severe due to a low extent of

9

aggregation in the distribution network, we introduce feedback to disturbances by solving the charging problem in a receding horizon fashion. The resulting centralized linear MPC scheme is then decomposed into a set of local control laws, which determine the charging strategy of each individual electric vehicle, and which are coordinated via a common (pseudo-)price for electrical energy. This price is generated by a centralized agent in such a way that aggregated power demand is kept within operational limits while PEVs are allowed to charge as quickly as possible (i.e. PEV-centric objective). Further details of our distributed PEV load control scheme is provided in Chapter V.

1.3 Original Contributions

The main contributions of this dissertation are:

- A linear formulation of the energy hub model is developed that is amenable to linearly constrained optimization. One such formulation employs binary integers to explicitly enforce non-simultaneous charging and discharging from energy storage. A second formulation represents a strictly (continuous) relaxation without integers, which permits simultaneous charging and discharging, but is also shown to accurately represent energy storage devices under economic objectives.

- "Hubert" is the nickname for a concise ASCII-based format developed herein to describe general energy hubs and enables quick construction, simulation, optimization, and analysis of large energy hub networks.

- A piece-wise linear convex relaxation of AC line losses is described that, together with a receding horizon MPC cascade mitigation scheme, is proven to be locally tight and enables the linear MPC scheme to alleviate overloaded transmission lines.

- A stable bilevel receding-horizon cascade mitigation scheme is developed which optimally balances economic and security (i.e. overload) objectives of power systems to alleviate overloads.

- Simulations of the IEEE Reliability Test System are carried out to demonstrate the performance of the receding horizon cascade mitigation scheme. The simulations highlight the role of energy storage in cascade mitigation.

- A distributed predictive control algorithm is developed to prevent distribution-level transformers from becoming overloaded by coordinating PEV charging.

1.4 Statement of Impact

The developed predictive control algorithms for overload mitigation and prevention in power systems are practical, yet rigorously justified and have real-world implications. The methods developed in this dissertation provide local utilities, ISOs,

and power engineers with a proof-of-concept that further automation of transmission and distribution contingency management can become useful in the near future. In addition, the vital role that energy storage plays in optimally balancing economic and security objectives serves to establish an "energy positioning" operating paradigm and opens the way to a radically different approach to operating power systems that could simultaneously facilitate the integration of massive amounts of renewable generation, reduce the operating cost, improve reliability and decrease the need to build new transmission lines.

1.5   Dissertation Outline

The overarching goal of this work lies with mitigation and prevention of overloads in power and energy systems. Specifically, employment of MPC-based schemes with simple, but sufficient, power system models provide practical, yet rigorously justified, solutions to overload mitigation problems. The chapters of this dissertation are outlined as follows:

Chapter II introduces the basic power system models that make up the basis of this dissertation. Namely, the unified branch model, PWL relaxation of losses, and IEEE Standard conductor temperature models are presented in this chapter.

Chapter III presents the energy hub model and develops a consistent linear model that is amenable to optimization. Then, the concise format "Hubert" is introduced and economic optimization of multi-energy system provides a contextual example.

Chapter IV is a large chapter which fully develops the receding horizon cascade mitigation scheme in detail. First, a multi-energy framework with energy storage is employed to alleviate line overloads, which motivates the notion of optimal balance of economic and security objectives, as well as the role of storage in cascade mitigation. Then, a stabilizing receding horizon MPC scheme is formulated for cascade mitigation in electric transmission systems with energy storage and renewables. It is proven that this scheme can utilize the convex relaxation of losses to alleviate overloads and a case-study of the IEEE RTS-96 system is carried out to highlight cascade mitigation potential.

Chapter V presents a non-centralized MPC-based overload prevention scheme in a distribution system setting. The dual-ascent method is employed with a finite iteration limit to provide control, in a distributed framework, of PEV charging and prevent a distribution-level transformer from being overloaded. A case-study of overnight charging is provided to highlight near-optimal performance.

Chapter VI concludes the dissertation and gives suggestions for future work.

CHAPTER II

Power System Models

2.1 Introduction

This chapter provides a comprehensive system-based description of the power system models employed in the dissertation. The models enable a description of the relationships between power flow, generators, energy storage, and loads. In particular, a unified approach to power flow modeling is described, including a lossy (piece-wise linear) DC power flow model. The lossy DC power flow model is achieved via a convex relaxation of line losses. The flow model is then combined with generators and loads to form the power balance equation. The IEEE Standard 738 for the current-temperature relationship of a transmission line conductor is described in Section 2.5. The models presented here constitute systems-level models that are amenable to linear optimization. Based on the models in this chapter, Chapters III, IV, and V can formulate optimization frameworks for the operation of power systems.

2.2 Basic notation and definitions

2.2.1 Power network as a graph

An electric power network is made up of transmission lines, generators, loads, energy storage, and other network elements (e.g. transformers). In this work, a power network is treated as a graph $\mathcal{G}$, which consists of a set of nodes (e.g. buses) $\mathcal{N}$ and a set of edges (also called feeders, lines, and arcs) $\mathcal{E}$. That is, a network graph is denoted $\mathcal{G} = (\mathcal{N}, \mathcal{E})$, for edges $e = (i, j) \in \mathcal{E}$ and nodes $i, j \in \mathcal{N}$. The cardinality of $\mathcal{E}$ and $\mathcal{N}$ are m and n, respectively. A node j is *adjacent* to i if $(i, j) \in \mathcal{E}$ (i.e. i and j are neighbors). The sets of generators, loads, adjacent nodes, and energy storage devices at node i are defined:

- Ω_i^G - set of generators at node i.

- Ω_i^D - set of loads at node i.

- Ω_i^N - set of adjacent nodes at node i.

- Ω_i^E - set of energy storage devices at node i.

12

The mapping of nodes to lines is accomplished with the adjacency matrix, $A \in \mathbb{R}^{n \times m}$, where the ith row represents node i and e^{th} column represents the eth arc. Matrix A is defined as:

$$A(i,e) = \begin{cases} 1, & \text{if } e = (i,j) \in \mathcal{E} \\ -1, & \text{if } e = (j,i) \in \mathcal{E} \\ 0, & \text{else} \end{cases} . \qquad (2.1)$$

For a thorough discussion of network flows and theory, please see [63].

2.2.1.1 Laplacian of a graph

From the adjacency matrix, the Laplacian of graph $\mathcal{G}$ is defined by

$$L(\mathcal{G}) = AA^{\top} \in \mathbb{R}^{n \times n}. \qquad (2.2)$$

The Laplacian exhibits many fascinating properties, which are detailed in [64]. In this dissertation, the property of interest captures the relationship between L and connectivity of the graph (i.e. the number of islands in the power system). A graph is *connected* if for every node i, there exists a path of edges to any node j. It can be shown that L is symmetric positive-semidefinite, which implies that the eigenvalues of L, $\lambda_i \geqslant 0$, $\forall i \in \mathcal{N}$. For a connected graph (i.e. a one-island network) exactly one eigenvalue is equal to zero. From the definition of A, it is easy to see that $A^{\top}\mathbf{1} = \mathbf{0}$, where $\mathbf{1} = \text{col}(1,\ldots,1) \in \mathbb{R}^n$, which implies that $\mathbf{1}$ is an eigenvector of L associated with eigenvalue $\lambda_1 = 0$. In fact, given a power network formed by W islands the Laplacian has eigenvalues $\lambda_1 = \lambda_2 = \ldots = \lambda_W = 0$. Since L is symmetric, the associated eigenvectors are orthogonal and describe the nodal sets: $\mathcal{N}_w = \{i \in \mathcal{N} \mid i \text{ is in island } w\}$, $\forall w = \{1,\ldots,W\}$.

Thus, if given power network topology (i.e. adjacency matrix A), computation of the eigenvalues of graph Laplacian L enables detection of islanding and the associated eigenvectors of L allows identification of the nodes in each island. This is particularly useful in automatic control since island-detection provides a method for automatically selecting slack buses for the AC power flow. That is, the AC power flow simulations in this dissertation automatically selects slack buses if islanding occurs via the methods described above.

2.2.2 Per unit system

Regardless of base voltage or phases, the per-unit system allows for uniform representation of power systems. From basic circuit analysis, the single-phase system has the following relationship between power ($S^{1\phi}$), current (I), and (line-to-neutral) voltage (V^{ln}):

$$S^{1\phi} = IV^{ln}. \qquad (2.3)$$

Now, consider a three-phase system with a chosen power base, $S_b^{3\phi}$, and nominal line-to-line base voltage, V_b^{ll}. From definitions,

$$V_b^{ll} = \sqrt{3}V_b^{ln} \qquad \text{and} \qquad S_b^{3\phi} = 3S_b^{1\phi}, \qquad (2.4)$$

one can describe base current and impedance in a three-phase system as follows:

$$S_b^{3\phi} = \sqrt{3}V_b^{ll}I_b \qquad (2.5)$$

$$\Rightarrow I_b = \frac{S_b^{3\phi}}{\sqrt{3}V_b^{ll}} \qquad (2.6)$$

$$\Rightarrow Z_b = \frac{(V_b^{ll})^2}{S_b^{3\phi}}. \qquad (2.7)$$

where I_b and Z_b are the base current (A) and base impedance (Ohm). For example, for three-phase base apparent power $S_b^{3\phi} = 100MVA$ and base voltage of $V_b^{ll} = 138$ kV, the base current is $I_b = 418.4$ A and the base impedance of $Z_b = 190.4\Omega$. In addition, if the per-unit bus voltage of 1.05 p.u., the actual voltage is $1.05V_b^{ll} = 144.9$ kV. Finally, if current and line-to-line voltage is expressed in p.u. (i.e. $x_{pu} = x/Z_b$), the following natural relationships hold:

$$S_{pu}^{3\phi} = I_{pu}V_{pu}^{ll} \qquad \text{and} \qquad S_{pu}^{loss} = R_{pu}I_{pu}^2, \qquad (2.8)$$

which highlights the intuitive nature of the per-unit system. That is, power is the product of voltage and current and losses are expressed as the product of the square of the current and resistance.

To represent per-unit values, the abbreviation "pu" is used throughout this dissertation and it should be clear from the context whether pu refers to voltage, current, impedance, or admittance.

2.3 Unified Branch Model

The physical laws that explicitly couple the nodes and the edges of the network must be considered. In any network, the power flowing between two connected nodes (i.e. across a line) in $\mathcal{G}$ depends on the physics of the power flow, which is different for different energy types. For example, the physical laws that describe natural gas flowing through pipelines is different from water flowing downstream to/from a hydro-electric dam. In the case of electrical energy, the telegraphers partial differential equations can be reduced to the standard lumped algebraic π-model [65].

A large power system may consist of multiple interconnected power system areas at different base voltages. This dissertation considers overhead transmission lines and in-phase (IPT) and phase-shifting transformers (PST) models, which are modeled separately in Figure 2.1. However, a special case of the "Unified Branch Model" developed in [66] and illustrated in Figure 2.2 is employed in this dissertation to allow for a single modeling framework. The series impedance, z_{ij}, defines the series

(a) Standard lumped transmission line π-model (b) Standard transformer model
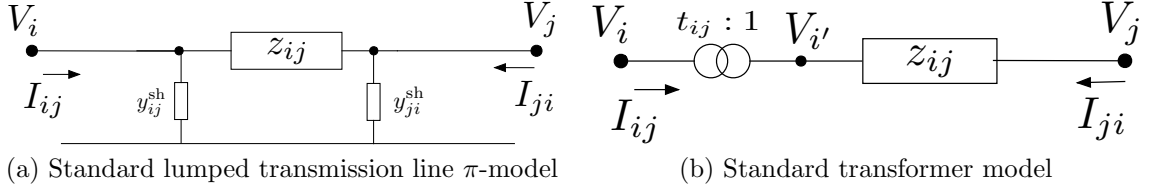
Figure 2.1: Standard branch models.
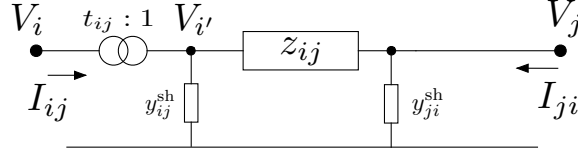
Figure 2.2: The unified branch model (π-model) with complex voltages, currents, taps, admittance, and shunts.

admittance, y_{ij}, as follows:

$$z_{ij} = r_{ij} + \imath x_{ij} \implies y_{ij} = \frac{1}{z_{ij}} = g_{ij} + \imath b_{ij} \tag{2.9}$$

$$g_{ij} = \frac{r_{ij}}{x_{ij}^2 + r_{ij}^2} \quad \text{and} \quad b_{ij} = -\frac{x_{ij}}{x_{ij}^2 + r_{ij}^2} \tag{2.10}$$

where r_{ij}, x_{ij}, g_{ij}, and b_{ij} are line resistance [Ω], reactance [Ω], conductance [S], and susceptance [S], respectively. The shunt admittance term is defined by

$$y_{ij}^{\text{sh}} = g_{ij}^{\text{sh}} + \imath b_{ij}^{\text{sh}} \approx \imath b_{ij}^{\text{sh}}, \tag{2.11}$$

since the shunt conductance value $g_{ij}^{\text{sh}} \sim \mathcal{O}(10^{-8}) << b_{ij}^{\text{sh}}$.

2.3.1   AC power flow

Represent the complex voltage at node i by phasor $V_i = U_i\underline{/\theta_i} = U_i e^{\imath \theta_i}$, the complex current across branch (i, j) by I_{ij}, and denote the complex transformer tap-ratio $t_{ij} = a_{ij}\underline{/\psi_{ij}}$. Note that the tap-ratio phase-angle represents the phase-shift provided by a PST and the tap-ratio magnitude defines the relationship between voltage magnitudes at nodes i and fictitious (non-physical) node i'. Essentially, a tap-changing transformer enables regulation of voltage and power flow.

The relationship between voltage at node i and fictitious (internal) node i' is determined by the complex tap-ratio and described as follows:

$$\left.\begin{array}{rl} U_i &= a_{ij}U_{i'} \\ \theta_i &= \theta_{i'} + \psi_{ij} \end{array}\right\} \Rightarrow V_i = t_{ij}V_{i'}. \tag{2.12}$$

Next, consider the currents entering (I_{ij}) and leaving ($I_{i'j}$) the ideal transformer.

15

From (2.12), the following relates the two currents:

$$V_i I_{ij}^* = t_{ij} V_{i'} I_{ij}^* \tag{2.13}$$

$$\Rightarrow V_i I_{ij}^* I_{i'j}^* = t_{ij} V_{i'} I_{ij}^* I_{i'j}^* \tag{2.14}$$

$$\Rightarrow (V_i I_{ij}^*) I_{i'j}^* = t_{ij} (V_{i'} I_{i'j}^*) I_{ij}^* \tag{2.15}$$

$$\Rightarrow S_i I_{i'j}^* = t_{ij} S_{i'} I_{ij}^* \tag{2.16}$$

$$\Rightarrow I_{i'j}^* = t_{ij} I_{ij}^* \tag{2.17}$$

$$\Rightarrow I_{i'j} = t_{ij}^* I_{ij} \tag{2.18}$$

where $(\cdot)^*$ denotes phasor conjugate and the apparent power $S_i \equiv S_{i'}$ since there are no active or reactive power losses in an ideal transformer. From Figure 2.2, it is now straightforward to derive the unified relationships between currents and voltages.

$$I_{ij} = \frac{I_{i'j}}{t_{ij}^*} = \frac{V_{i'} y_{ij}^{\mathrm{sh}} + (V_{i'} - V_j) y_{ij}}{t_{ij}^*} \tag{2.19}$$

$$= \frac{\frac{1}{t_{ij}} V_i y_{ij}^{\mathrm{sh}} + (\frac{1}{t_{ij}} V_i - V_j) y_{ij}}{t_{ij}^*} \tag{2.20}$$

$$= \frac{1}{t_{ij}^* t_{ij}} V_i y_{ij}^{\mathrm{sh}} + (\frac{1}{t_{ij}^* t_{ij}} V_i - \frac{1}{t_{ij}^*} V_j) y_{ij} \tag{2.21}$$

$$= \frac{1}{a_{ij}^2} V_i y_{ij}^{\mathrm{sh}} + (\frac{1}{a_{ij}^2} V_i - \frac{1}{t_{ij}^*} V_j) y_{ij}. \tag{2.22}$$

Similarly for current I_{ji}:

$$I_{ji} = V_j y_{ji}^{\mathrm{sh}} + (V_j - V_{i'}) y_{ij} \tag{2.23}$$

$$= V_j y_{ji}^{\mathrm{sh}} + (V_j - \frac{1}{t_{ij}} V_i) y_{ij}. \tag{2.24}$$

In matrix form, the relationship between voltages and currents becomes:

$$\begin{bmatrix} I_{ij} \\ I_{ji} \end{bmatrix} = \begin{bmatrix} \frac{1}{a_{ij}^2}(y_{ij}^{\mathrm{sh}} + y_{ij}) & -\frac{1}{t_{ij}^*} y_{ij} \\ -\frac{1}{t_{ij}} y_{ij} & (y_{ji}^{\mathrm{sh}} + y_{ij}) \end{bmatrix} \begin{bmatrix} V_i \\ V_j \end{bmatrix}. \tag{2.25}$$

Remark II.1. The matrix in (2.25) highlights the utility of the unified branch model. Namely, different branch types are captured within a single (unifying) formulation. For example, to model

- a transmission line: set $t_{ij} = 1\underline{/0}$.

- an in-phase transformer (IPT): set $y_{ij}^{\mathrm{sh}} \equiv 0 \equiv y_{ji}^{\mathrm{sh}}$; $t_{ij} = a_{ij}\underline{/0}$.

- a phase-shifting transformer (PST): set $y_{ij}^{\mathrm{sh}} \equiv 0 \equiv y_{ji}^{\mathrm{sh}}$; $t_{ij} = 1\underline{/\psi_{ij}}$.

Note that for transmission lines and IPTs, the matrix is symmetric. However, for a PST, the presence of the tap-ratio t_{ij} yields an asymmetric matrix.

The complex power $S_{ij} = f_{ij} + \imath q_{ij}$ is derived as follows:

$$S_{ij} = V_i I_{ij}^* = V_i \left(\frac{1}{a_{ij}^2} V_i^* y_{ij}^{\text{sh}*} + (\frac{1}{a_{ij}^2} V_i^* - \frac{1}{t_{ij}} V_j^*) y_{ij}^* \right) \tag{2.26}$$

$$= -\imath b_{ij}^{\text{sh}} \frac{U_i^2}{a_{ij}^2} + \frac{U_i^2}{a_{ij}^2}(g_{ij} - \imath b_{ij}) - \frac{U_i U_j e^{\imath(\theta_{ij} - \psi_{ij})}}{a_{ij}}(g_{ij} - \imath b_{ij}) \tag{2.27}$$

$$= -\imath b_{ij}^{\text{sh}} \frac{U_i^2}{a_{ij}^2} + \frac{U_i^2}{a_{ij}^2}(g_{ij} - \imath b_{ij}) - \frac{U_i U_j}{a_{ij}}(\cos\hat{\theta}_{ij} + \imath \sin\hat{\theta}_{ij})(g_{ij} - \imath b_{ij}), \tag{2.28}$$

where voltage phase angles $\hat{\theta}_{ij} := \theta_{ij} - \psi_{ij}$ and $\theta_{ij} := \theta_i - \theta_j$. Re-arranging and separating real (active) and imaginary (reactive) terms, the following define the **unified AC power flow equations**:

$$f_{ij} = \frac{U_i^2}{a_{ij}^2} g_{ij} - \frac{U_i U_j}{a_{ij}}[g_{ij}\cos(\hat{\theta}_{ij}) + b_{ij}\sin(\hat{\theta}_{ij})], \tag{2.29}$$

$$q_{ij} = -\frac{U_i^2}{a_{ij}^2}(b_{ij} + b_{ij}^{\text{sh}}) - \frac{U_i U_j}{a_{ij}}[g_{ij}\sin(\hat{\theta}_{ij}) - b_{ij}\cos(\hat{\theta}_{ij})], \tag{2.30}$$

where f_{ij} and q_{ij} represents the active and reactive power of transmission line (i, j), respectively.

Remark II.2. The standard notation for the active AC power flow is p_{ij} (for "power"); however, this dissertation considers general energy flows and, therefore, employs f_{ij} (for "flow") instead.

The AC model is nonlinear and non-convex and relates voltage magnitude and voltage phase angles at connected nodes to the active and reactive power flowing across the connecting arc. The AC power flow is widely accepted as a valid representation of an electrical physical power system.

2.3.2 DC flow model

A linear approximation of the AC power flow is feasible under reasonable simplifying assumptions, which yields the so-called DC power flow model. The DC model allows for good approximation of active power flows. The modeling simplifications are:

- Voltage magnitudes are generally between $[0.95, 1.05]$ p.u. (even closer to 1 pu, if sufficient var resources are available). Therefore, it is reasonable to set $U_i \approx 1$ p.u.

- Phase angle differences between adjacent nodes are generally less than $\pi/4$. Therefore, a Taylor expansion of $\sin(\hat{\theta}_{ij}) = \hat{\theta}_{ij} - \mathcal{O}(\hat{\theta}^3) \approx \hat{\theta}_{ij}$ reveals a reasonable approximation.

- In transmission systems, reactance values are generally much greater than the resistance values (i.e. $x_{ij} > 4r_{ij}$), which allows approximations $b_{ij} \approx -1/x_{ij}$ and $g_{ij} \approx 0$.

- Ignore reactive power, q_{ij}.

Together, these simplifications reduce the AC power flow equations into **the unified DC power flow equation**:

$$f_{ij} \approx -\frac{b_{ij}}{a_{ij}} \sin(\hat{\theta}_{ij}) \approx \frac{\hat{\theta}_{ij}}{a_{ij}x_{ij}}, \tag{2.31}$$

where x_{ij} is the constant reactance and f_{ij} and θ_{ij} represent the power flow and phase angle difference across arc (i, j), respectively. The term "DC power flow" originates from the resemblance between Ohm's law ($I = V/R$) and (2.31).

Remark II.3. The unified DC power flow model in (2.31) is, in fact, not linear due to the presence of the variable transformer tap ratio a_{ij}. However, under standard operating conditions an on-load tap-changing transformer varies with the load and a_{ij} can, therefore, be considered constant over a fixed time-interval (e.g. ~10-30 minutes). In addition, $a_{ij} \approx 1$ p.u. is generally a valid assumption.

Considering a constant tap ratio a_{ij}, a linear expression for the DC power flow can be derived:

$$f_{ij} \approx \frac{\theta_{ij} - \psi_{ij}}{a_{ij}x_{ij}} = \frac{\hat{\theta}_{ij}}{\hat{x}_{ij}}, \tag{2.32}$$

where $\hat{x}_{ij} := a_{ij}x_{ij}$ is the lumped tap reactance. For different branch types, the DC power flowing across line (i, j) yields:

- a transmission line ($a_{ij} = 1$; $\psi_{ij} = 0$): $f_{ij} = \frac{\theta_{ij}}{x_{ij}}$.

- an in-phase transformer ($\psi_{ij} = 0$): $f_{ij} = \frac{\theta_{ij}}{\hat{x}_{ij}}$.

- a phase-shifting transformer ($a_{ij} = 1$): $f_{ij} = \frac{\hat{\theta}_{ij}}{x_{ij}}$.

Note that the unified DC power flow as presented in (2.32) is similar to the standard DC power flow model [67]. In addition, the unified branch model captures the phase-shift from the PST and is, therefore, amenable to active power flow control schemes, which are discussed in Chapter IV.

2.3.3 Errors in unified DC Approximation

While the standard DC power flow is accepted as a reasonable approximation for (active) AC power flow on transmission lines, the approximation of transformers (IPT and PST) with the (linear) unified DC formulation is less explored in literature. This section provides an informal investigation of the errors resulting from a linear

Table 2.1: Parameters for unified AC/DC error analysis

Parameter	Value	Unit
Bus voltage, V_i	1.00	p.u.
Line reactances, x_{ij}	0.084	p.u.
Ratio of reactance-resistance, x_{ij}/r_{ij}	10	-
Voltage phase angle difference, θ_{ij}	$[-1, 1]$	rads
Transformer tap ratio, a_{ij}	$[0.90, 1.10]$	p.u.
Transformer tap phase shift, ψ_{ij}	$[-10, 10]$	degrees

approximations of the unified AC branch model in (2.29). Of interest is the approximation error for specific cases of tap ratio $t_{ij} = a_{ij}\underline{/\psi_{ij}}$. Therefore, two test scenarios are considered, one with $a_{ij} \equiv 1$ to explore approximation over variable ψ_{ij}, and the other scenario considers $\psi_{ij} \equiv 0$ and explores variation in a_{ij}. Approximation errors for both flow directions are similar, so, without loss of generality, only the errors associated with unified power flows $i \to j$ (i.e. f_{ij}) are considered here.

The active power flow characteristics of the unified AC and DC models are compared. It is assumed in this section that sufficient reactive var resources are available to maintain a flat voltage profile. That is, $U_i = U_j = 1$ p.u., which yields the following unified AC and DC models:

$$\text{AC model}: \qquad \frac{g_{ij}}{a_{ij}^2} - \frac{1}{a_{ij}} \left[g_{ij}\cos(\theta_{ij} - \psi_{ij}) + b_{ij}\sin(\theta_{ij} - \psi_{ij}) \right] \qquad (2.33)$$

$$\text{DC model}: \qquad \frac{\theta_{ij} - \psi_{ij}}{a_{ij}x_{ij}} \qquad (2.34)$$

The salient parameter values are displayed in Table 2.1, where the bracket notation $[a, b]$ denotes the parameter interval. The reactance value is based on standard per-unit values as given in the IEEE RTS-96 network [68]. Note that in this network, the ratio of reactance and resistance for the transformer $x_{ij}/r_{ij} \approx 40$, however, in this section, a ratio of 10 is utilized, which yields slightly exaggerated errors.

The unified AC and DC flow models are simulated in Matlab according to Table 2.1 and associated comparison and approximation errors of the unified DC power flow model are illustrated in Figure 2.3. As displayed in Figures 2.3a and 2.3b, for voltage phase angle differences $|\hat{\theta}_{ij}| < 30°$, the AC and DC unified branch models are difficult to separate. The unified DC model captures the presence of PSTs ($|\psi_{ij}| > 0$, $a_{ij} = 1$) as shown in Figure 2.3c with errors that are within standard DC flow approximations ($\sim 10\%$). In fact, if one ignores the presence of ψ_{ij} in the unified branch model and, instead, employs a standard DC power flow model (i.e. θ_{ij}/x_{ij}), then significant approximation errors can be expected for $|\psi_{ij}| > 0$.

For the case of $a_{ij} \neq 1$, the unified DC branch model yields approximation errors that increase as $|1 - a_{ij}|$ increases. Consider $\psi_{ij} \equiv 0$, then the absolute error ϵ_A

between unified AC and DC formulations is given by:

$$\epsilon_A = \left| \frac{g_{ij}}{a_{ij}^2} - \frac{1}{a_{ij}} \left(g_{ij} \cos \theta_{ij} + b_{ij} \sin \theta_{ij} \right) - \frac{\theta_{ij}}{a_{ij} x_{ij}} \right| \tag{2.35}$$

$$= \left| \frac{g_{ij}}{a_{ij}^2} - \frac{g_{ij}}{a_{ij}} \left(\cos \theta_{ij} - \frac{x_{ij}}{r_{ij}} \sin \theta_{ij} + \frac{\theta_{ij}}{g_{ij} x_{ij}} \right) \right| \tag{2.36}$$

$$\approx \left| \frac{g_{ij}}{a_{ij}^2} - \frac{g_{ij}}{a_{ij}} \left(1 - \frac{\theta_{ij}^2}{2} - \frac{x_{ij}}{r_{ij}} \theta_{ij} + \frac{x_{ij}}{r_{ij}} \frac{\theta_{ij}^3}{6} + \frac{\theta_{ij}}{g_{ij} x_{ij}} \right) \right| \tag{2.37}$$

$$= \frac{g_{ij}}{a_{ij}} \left| \frac{1}{a_{ij}} - \left(1 + \frac{r_{ij}}{x_{ij}} \theta_{ij} - \frac{\theta_{ij}^2}{2} + \frac{x_{ij}}{r_{ij}} \frac{\theta_{ij}^3}{6} \right) \right| \tag{2.38}$$

$$= \frac{g_{ij}}{a_{ij}} \left| \left(\frac{1}{a_{ij}} - 1 \right) - \frac{r_{ij}}{x_{ij}} \theta_{ij} + \frac{\theta_{ij}^2}{2} - \frac{x_{ij}}{r_{ij}} \frac{\theta_{ij}^3}{6} \right| \tag{2.39}$$

$$\approx \frac{g_{ij}}{a_{ij}} \left| \left(\frac{1}{a_{ij}} - 1 \right) - \frac{r_{ij}}{x_{ij}} \theta_{ij} \right|, \tag{2.40}$$

where the approximation in (2.37) is achieved by a 2nd-order Taylor expansion of sin and cos while approximation (2.40) utilizes a small-angle approximation. The derivation highlights that for sufficiently small angles, the error is a function of fixed physical ratio x_{ij}/r_{ij} and tap variable a_{ij}. This is displayed in Figure 2.3d, where absolute approximation errors for $a_{ij} = 0.9, 1.10$ and $\theta_{ij} \approx 0$ yield $\epsilon_A \approx 0.1$ p.u., which presents a tube-like error bias for tap-changing transformer, which can be relatively significant for $|\theta_{ij}| > 0$. Unlike the DC model, with the conductance term and even function $\cos(\theta_{ij})$, the unified AC power flow model is not symmetric with respect to $\theta_{ij} = 0$. This means that errors are asymmetric, which is evident by the "twist" in the error-tube at $\theta_{ij} \approx 1$, which is shown in Figure 2.3d. However, for standard transformer x_{ij}/r_{ij} ratios and a_{ij}-values, it generally holds that $a_{ij} \in [0.95, 1.05]$ and $|\theta_{ij}| < 30°$, which implies that the DC unified branch flow provides a good approximation of actual (AC) line flows.

To summarize error analysis, **if $|\theta_{ij} - \psi_{ij}| << 1$ and $a_{ij} \approx 1$, then the unified DC model provides a valuable representation of transformers and transmission lines**.

2.3.4   Unified Branch Losses

The unified DC formulation presented in (2.32) ignores active line losses. Defining $\hat{\theta}_{ij} := \theta_{ij} - \psi_{ij}$, losses on branch (i, j) can be modeled via the unified AC power flow
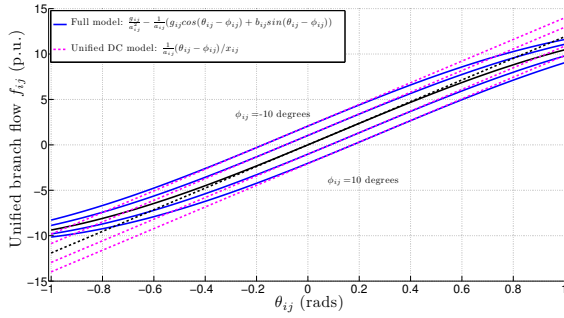
(a) Varying phase-shift with $a_{ij} \equiv 1$.
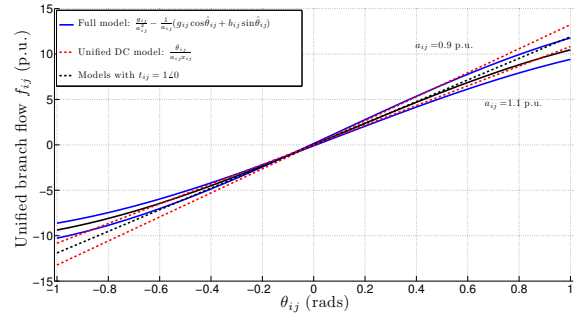
(b) Varying tap-turns ratio with $\psi_{ij} \equiv 0$.
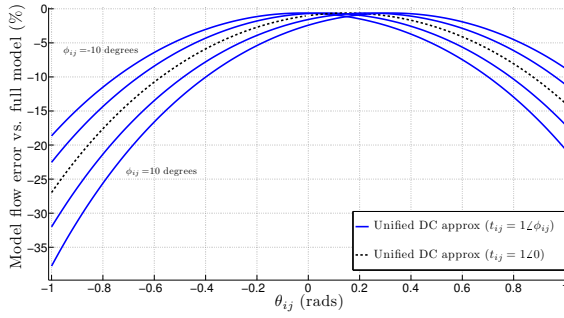
(c) Relative phase-shift error with $a_{ij} \equiv 1$.
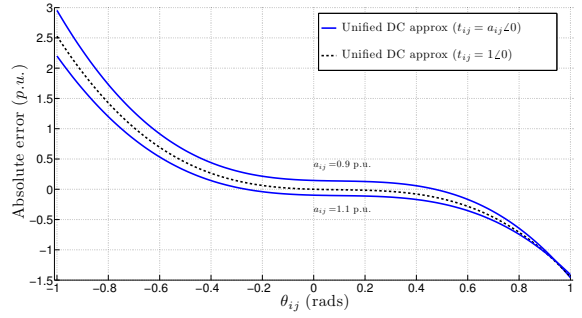
(d) Absolute tap-turns ratio error with $\psi_{ij} \equiv 0$.

Figure 2.3: Comparing unified AC and DC active power models for different ψ_{ij} and a_{ij} values. The black lines represent cases with $t_{ij} = 1\underline{/0}$, which is equivalent to standard power flow across a transmission line with $g_{ij}^{\mathrm{sh}} = g_{ji}^{\mathrm{sh}} = 0$.

equations, as follows:

$$f_{ij}^{loss} = f_{ij} + f_{ji} \tag{2.41}$$

$$= g_{ij} \left(\frac{U_i^2}{a_{ij}^2} + U_j^2 - 2 \frac{U_i}{a_{ij}} U_j \cos \left(\hat{\theta}_{ij} \right) \right) \tag{2.42}$$

$$\approx g_{ij} \left(\frac{1}{a_{ij}^2} + 1 - \frac{2}{a_{ij}} \cos(\hat{\theta}_{ij}) \right) \tag{2.43}$$

$$\approx g_{ij} \left(\left(\frac{1}{a_{ij}} - 1 \right)^2 + \frac{\hat{\theta}_{ij}^2}{a_{ij}} \right) \tag{2.44}$$

$$f_{ij}^{loss} \approx g_{ij} \frac{\hat{\theta}_{ij}^2}{a_{ij}} = \frac{r_{ij}}{r_{ij}^2 + x_{ij}^2} \frac{\hat{\theta}_{ij}^2}{a_{ij}}. \tag{2.45}$$

The approximation in (2.43) comes from the 1 p.u. voltage magnitude assumption, while the approximation in (2.44) is due to a 2nd-order Taylor expansion of $\cos(\hat{\theta}_{ij}) = 1 - \frac{\hat{\theta}_{ij}^2}{2!} + \mathcal{O}(\hat{\theta}_{ij}^4) \approx 1 - \frac{\hat{\theta}_{ij}^2}{2!}$, which is reasonable for $\hat{\theta}_{ij} << \pi/2$. Equation (2.45) stems from application of the simplifying assumption that the nominal tap-ratio is close to one (i.e. $(1 - a_{ij})^2 \approx 0$) and the definition of conductance:

$$g_{ij} = \frac{r_{ij}}{r_{ij}^2 + x_{ij}^2} \approx \frac{r_{ij}}{x_{ij}^2}, \tag{2.46}$$

which is valid since $x_{ij} > 4r_{ij}$ is a characteristic of most transmission systems and allows for reasonable approximation of g_{ij}. Thus, the following describes **the unified "DC" line losses**:

$$f_{ij}^{loss} \approx \frac{r_{ij} \hat{\theta}_{ij}^2}{a_{ij} x_{ij}^2} = a_{ij} r_{ij} f_{ij}^2, \tag{2.47}$$

with unified DC flow f_{ij} defined as in (2.32). Note that the loss term, f_{ij}^{loss}, is quadratic in $\hat{\theta}_{ij}$ and is not suitable for the strictly linear formulation. To include a meaningful model of losses into an linear formulation, one can apply a standard (piece-wise) linear relaxation of losses that circumvents the need for integer optimization, see [69, 70]. To simplify notation in the development of the piecewise linear (PWL) approximation, let $a_{ij} = 1$ and $\psi_{ij} = 0$. Derivation *with* a_{ij} and ψ_{ij} is straightforward but excluded here.

2.3.4.1 PWL Approximation of Line Losses

The approximate line losses in (2.47) can be replaced by a PWL formulation consisting of S linear segments of width $\Delta\theta_{ij}(s)$, $s \in \{1, \ldots, S\}$. Denote the slopes of

22
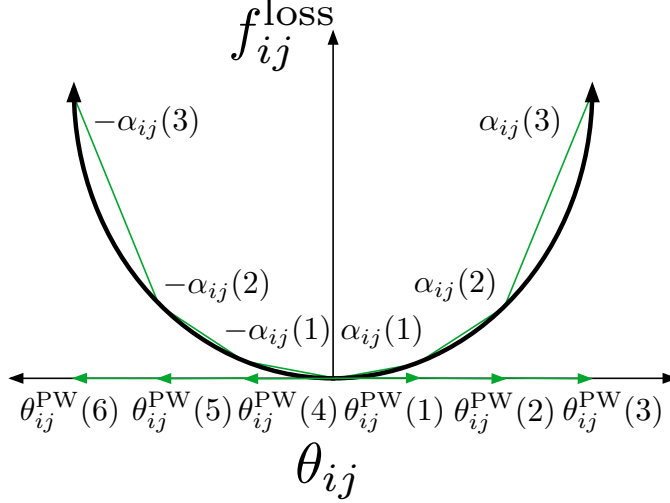
Figure 2.4: Piece-wise linear line losses for $S = 3$ linear identical segments.

each segment $\alpha_{ij}(s)$ and define variables $\theta_{ij}^{\mathrm{PW}}(s)$, $\forall s \in \{1, \ldots, S\}$, such that:

$$f_{ij}^{\mathrm{loss}}(\theta_{ij}) \approx \mathrm{PWL}\left[\frac{r_{ij}}{x_{ij}^2}\theta_{ij}^2\right] \tag{2.48}$$

$$= \mathrm{PWL}\left[\frac{r_{ij}}{x_{ij}^2}|\theta_{ij}|^2\right] = \sum_{s=1}^{S}\alpha_{ij}(s)\theta_{ij}^{\mathrm{PW}}(s), \tag{2.49}$$

where PWL[.] is a piece-wise linear approximation. Figure 2.4 illustrates PWL$[f_{ij}^{\mathrm{loss}}]$ for $S = 3$. Since the line loss function is symmetric with respect to θ_{ij}, replacing θ_{ij} with $|\theta_{ij}|$ means that one only has to consider S different $\theta_{ij}^{\mathrm{PW}}(s)$ variables for each line (i, j) and not all $2S$ variables.

Implementation of PWL[.] within an optimization framework generally requires binary integers to enforce adjacency conditions for PWL segments [71, page 7]. Adjacency conditions ensure that $\theta_{ij}^{\mathrm{PW}}(s) > 0 \Rightarrow \theta_{ij}^{\mathrm{PW}}(p) = \Delta\theta_{ij}(p)\ \forall p < s$.

Remark II.4. While the PWL formulation presented herein does not depend on segment width, there exists multiple techniques for choosing non-identical segment widths $\Delta\theta_{ij}(s)$, e.g. [72]. However, in this dissertation, for the sake of simplicity, identical widths are assumed for all segments and for all lines. That is,

$$\Delta\theta_{ij}(s) := \Delta\theta = \theta^{\max}/S \tag{2.50}$$

is the segment width $\forall s = \{1, \ldots, S\}, \forall(i, j) \in \mathcal{A}$.

If one omits integers and relaxes adjacency conditions, it implies a strictly continuous linear approximation of line losses that is equivalent to a bounded convex relaxation of PWL[.]. The linear relaxation is convex since f_{ij}^{loss} is strictly locally convex for $\theta_{ij} \in (-\pi/2, \pi/2)$ and $g_{ij} > 0$, which is proven by the following.

Lemma II.5. *The PWL relaxation is convex since $f_{ij}^{loss}(\theta_{ij})$ is locally strictly convex.*

23

Proof. Recall that f_{ij}^{loss} is strictly convex if the Hessian is positive definite (i.e. $\nabla^2 f_{ij}^{\text{loss}} > 0$). Assuming the system is operating near standard conditions, then voltage magnitudes $U_i, U_j \approx 1$ and $a_{ij} > 0$ and it follows:

$$f_{ij}^{\text{loss}}(\theta_{ij}) \approx g_{ij} \left(\frac{1}{a_{ij}^2} + 1 - \frac{2}{a_{ij}} \cos(\theta_{ij}) \right) \tag{2.51}$$

$$\Longrightarrow \nabla^2 f_{ij}^{\text{loss}} = \frac{d^2}{d\theta_{ij}^2}(f_{ij}^{\text{loss}}) \approx \frac{2g_{ij}}{a_{ij}} \cos(\theta_{ij}) \tag{2.52}$$

which is strictly positive for $\theta_{ij} \in (-\pi/2, \pi/2)$ and $a_{ij}, g_{ij} > 0$. $\qquad\square$

Remark II.6 (Importance of convex optimization). Convex optimization guarantees that any optimal (and feasible) solution is the globally optimal solution (i.e. local optimality implies global optimality). Furthermore, the computational speed of solving a convex optimization problem is significantly reduced compared to non-convex optimization.

Strict convexity ensures that the PWL approximation exhibits monotonically increasing segment slopes as a function of s. The segment slopes are defined as

$$\alpha_{ij}(s) = \frac{f_{ij}^{\text{loss}}(s\Delta\theta) - f_{ij}^{\text{loss}}((s-1)\Delta\theta)}{s\Delta\theta - (s-1)\Delta\theta} \tag{2.53}$$

$$= \frac{r_{ij}}{x_{ij}^2}(2s-1)\Delta\theta, \tag{2.54}$$

which yields strict monotonicity of segment slopes with respect to s:

$$(2s-1)\frac{r_{ij}}{x_{ij}^2}\Delta\theta = \alpha_{ij}(s) < \alpha_{ij}(s+1) = 2s\frac{r_{ij}}{x_{ij}^2}\Delta\theta. \tag{2.55}$$

The PWL approximation is a relaxation when adjacency conditions are not enforced, as illustrated in Figure 2.5a for $S = 3$:

$$f_{ij}^{\text{loss}} \approx \text{PWL}[f_{ij}^{\text{loss}}] \leqslant \sum_{s=1}^{S} \alpha_{ij}(s)\theta_{ij}^{\text{PW}}(s) \tag{2.56}$$

$$= \frac{r_{ij}}{x_{ij}^2}\Delta\theta \sum_{s=1}^{S}(2s-1)\theta_{ij}^{\text{PW}}(s), \tag{2.57}$$

where segment variables $\theta_{ij}^{\text{PW}}(s)$ are defined by

$$|\theta_{ij}| = \sum_{s=1}^{S} \theta_{ij}^{\text{PW}}(s) \tag{2.58}$$

with $\theta_{ij}^{\text{PW}}(s) \in [0, \Delta\theta]$ for $s = 1, ..., S$ representing the segments in the PWL approximation. To model the (non-convex) absolute value relation in equation (2.58) within

a linear formulation, apply the following relaxation:

$$\theta_{ij} = \theta_{ij}^+ - \theta_{ij}^- \tag{2.59}$$

$$\sum_{s=1}^{S} \theta_{ij}^{\text{PW}}(s) := \theta_{ij}^+ + \theta_{ij}^- \tag{2.60}$$

where $\theta_{ij}^+, \theta_{ij}^- \geqslant 0$. This is equivalent to a bounded convex relaxation of (2.58), as demonstrated in Figure 2.5b and with the triangle-inequality:

$$|\theta_{ij}| = |\theta_{ij}^+ - \theta_{ij}^-| \leqslant |\theta_{ij}^+| + |\theta_{ij}^-| = \theta_{ij}^+ + \theta_{ij}^-. \tag{2.61}$$

Notice that in the absence of enforcing the complementarity condition: $\theta_{ij}^+ \theta_{ij}^- = 0$, the convex relaxation may overestimate $|\theta_{ij}|$ and, hence, overestimate losses.

Remark II.7. The complimentarity condition can be explicitly described via use of mixed-integer optimization:

$$\theta_{ij}^+ \leqslant z_{ij}\theta^{\text{max}},$$
$$\theta_{ij}^- \leqslant (1 - z_{ij})\theta^{\text{max}},$$
$$z_{ij} \in \{0, 1\}.$$

However, integer implementation is not pursued in this dissertation as it prevents a strictly linear formulation of line losses.

From henceforth, to simplify notation, denote unified branch losses by f_{ij}^{loss}. To summarize, **the convex relaxation of active line losses is described by the following**:

$$f_{ij}^{\text{loss}} = \frac{r_{ij}}{a_{ij}x_{ij}^2}\Delta\theta \sum_{s=1}^{S}(2s - 1)\theta_{ij}^{\text{PW}}(s) \tag{2.62a}$$

$$\sum_{s=1}^{S} \theta_{ij}^{\text{PW}}(s) = \theta_{ij}^+ + \theta_{ij}^- \tag{2.62b}$$

$$\theta_{ij} - \psi_{ij} = \theta_{ij}^+ - \theta_{ij}^- \tag{2.62c}$$

$$|\theta_{ij} - \psi_{ij}| \in [0, \theta^{\text{max}}] \tag{2.62d}$$

$$\theta_{ij}^+, \theta_{ij}^- \geqslant 0, \tag{2.62e}$$

$$\theta_{ij}^{\text{PW}}(s) \in [0, \Delta\theta]. \tag{2.62f}$$

The linear formulation presented in (2.62) is a convex relaxation of a lossy DC power flow that is greater than or equal to $\text{PWL}[f_{ij}^{\text{loss}}]$. Equality occurs only when both absolute value complementarity (i.e. $\theta_{ij}^+ \theta_{ij}^- = 0$) and PWL adjacency conditions are satisfied. Under such conditions, the relaxation is considered "tight" and the model is exact (with respect to $\text{PWL}[f_{ij}^{\text{loss}}]$) and provides a superior method for

(a) PWL adjacency relaxation   (b) Absolute value relaxation
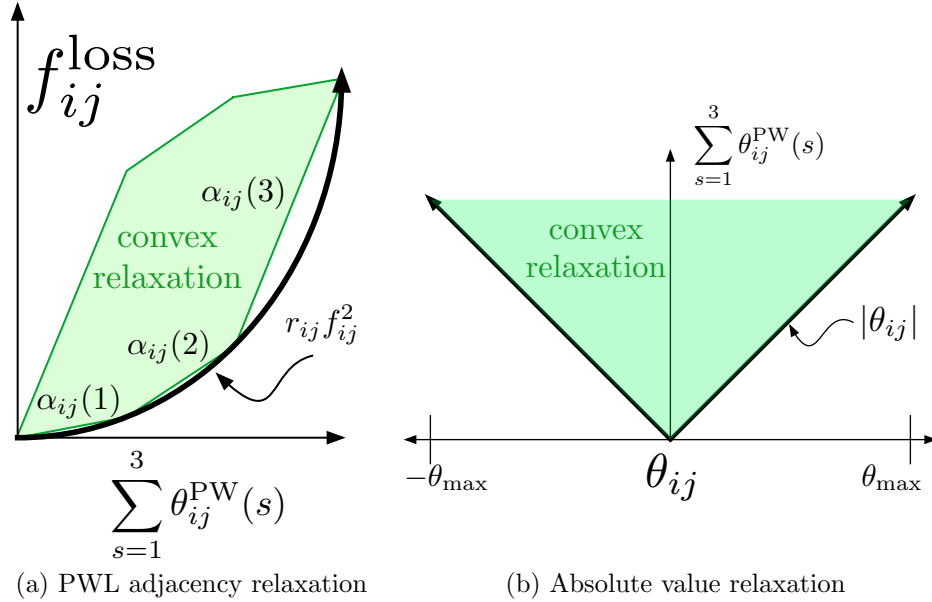
Figure 2.5: Relaxing adjacency conditions and absolute value complementarity condition (i.e. $\theta_{ij}^+\theta_{ij}^- = 0$) for PWL approximation with $S = 3$. Notice how the PWL segment variables $\theta_{ij}^{\mathrm{PW}}(s)$ define the relationship between phase angles and line losses.

estimating line losses than standard linearization about an operating point. Furthermore, when the losses are relaxed (i.e. not tight), overestimated losses are denoted "fictitious losses" as they exist only as a figment of the MPC controller model and not in the actual system. Finally, if a specific line's relaxation is tight, but other lines are not, the term "locally tight" is used.

Remark II.8. To employ the PWL approximation of line losses within an optimization framework, it is often necessary to ensure that, under conditions of interest, the convex relaxation is tight. Otherwise, significant modeling errors result from the relaxation. In [69], the authors prove (under implicit assumptions of non-negative LMPs) that minimizing fuel costs in an economic dispatch setting provides sufficient conditions to ensure a tight relaxation. As is presented in Chapter IV with a model-predictive scheme, minimizing conductor temperature overloads subject to mild simplifications provides another set of sufficient conditions for a locally tight relaxation. The locally tight relaxation is sufficient for the model-predictive scheme to stabilize temperature overloads.

2.3.5 Matrix notation for unified models

For network $\mathcal{G} = (\mathcal{N}, \mathcal{E})$, denote arcs with $e = (i, j) \in \mathcal{E}$ for nodes $i, j \in \mathcal{N}$ and set $m = |\mathcal{E}|$, $n = |\mathcal{N}|$, and define p as the number of PSTs in $\mathcal{G}$. Then, let $A \in \mathbb{R}^{n \times m}$ be the node-arc incidence matrix, let $B \in \mathbb{R}^{p \times m}$ be the PST-to-arc mapping, and let $X = \mathrm{diag}(\hat{x}_1, \ldots, \hat{x}_m) \in \mathbb{R}^{m \times m}$ be the diagonal matrix of unified reactance values $\hat{x}_e := a_{ij}x_{ij}$. For example, given arc e, $A(i, e) = 1$, $A(j, e) = -1$ and, for

- a transmission line, $t_{ij} = 1\underline{/0}$ and $X(e,e) = \hat{x}_e = x_{ij}$.

- an IPT, $t_{ij} = a_{ij}\underline{/0}$ and $X(e,e) = \hat{x}_e = a_{ij}x_{ij}$

- PST k, $X(e,e) = \hat{x}_e = a_{ij}x_{ij}$, and $B(k,e) = 1$.

The unified DC branch model, as stated in equation (2.32), is then defined in matrix form as:

$$X\mathbf{f} = A^\top\theta - B^\top\psi. \tag{2.63}$$

where $[\mathbf{f}]_e = f_{ij}$ is the unified DC power flow of branch e. Similarly, $\theta = \mathrm{col}(\theta_1, \ldots, \theta_n)$ is the vector of nodal voltage phase angles and $[\psi]_k = \psi_{ij}$ is the branch phase-shifts of PST k.

With regards to the PWL approximation of active power losses in equation (2.62), define $\mathbf{c}_e = r_{ij}\Delta\theta\,\mathrm{col}(1, 3, \ldots, 2S-1) \in \mathbb{R}^S$, $C_S = \mathrm{diag}(\mathbf{c}_1^\top, \ldots, \mathbf{c}_m^\top) \in \mathbb{R}^{m \times (mS)}$ is the block-diagonal matrix of PWL slope weights, and let $X_l = \mathrm{diag}(\tilde{x}_1, \ldots, \tilde{x}_m) \in \mathbb{R}^{m \times m}$ be the diagonal matrix of unified loss-reactance values $\tilde{x}_e := a_{ij}x_{ij}^2$. Then, the active losses for all lines can be described as

$$X_l\mathbf{f}^{\mathrm{loss}} = C_l\theta^{\mathrm{PW}} \tag{2.64}$$

where $[\mathbf{f}^{\mathrm{loss}}]_e = f_{ij}^{\mathrm{loss}}$ and $[\theta^{\mathrm{PW}}]_e = \theta_{ij}^{\mathrm{PW}}$ with $\theta_{ij}^{\mathrm{PW}} = \mathrm{col}(\theta_{ij}^{\mathrm{PW}}(1), \ldots, \theta_{ij}^{\mathrm{PW}}(S)) \in \mathbb{R}^S \; \forall e \in \mathcal{E}$ are vectors of unified DC line losses and PWL segment variables, respectively.

The relationship between line e's PWL variables $\theta_{ij}^{\mathrm{PW}}$ and nodal phase angles θ_i, θ_j is defined through the intermediate variables $\theta_{ij}^-, \theta_{ij}^+$ as given by (2.62c) and (2.62b). Let $D_{\mathrm{PW}} = \mathrm{diag}(\mathbf{1}_S^\top, \ldots, \mathbf{1}_S^\top) \in \mathbb{R}^{m \times mS}$ be a block-diagonal matrix of ones where $\mathbf{1}_S = \mathrm{col}(1, \ldots, 1) \in \mathbb{R}^S$, then

$$\theta^+ + \theta^- = D_{\mathrm{PW}}\theta^{\mathrm{PW}} \tag{2.65}$$
$$\theta^+ - \theta^- = A^\top\theta - B^\top\psi, \tag{2.66}$$

with $\theta^+ = \mathrm{col}(\theta_1^+, \ldots, \theta_m^+) \in \mathbb{R}^m$ and θ^- similarly defined.

Note that the scalar bounds defined in (2.62) are defined as $0 < \Delta\theta$, $\theta^{\mathrm{PW}} \in [0, \Delta\theta]^{mL} \subset \mathbb{R}^{mL}$, and $\theta^+, \theta^- \geqslant \mathbf{0}$.

Remark II.9 (PWL optimization and constraints). The (real) active power flow in line $e = (i,j)$ as measured at bus i is given by $f_{ij} + \frac{1}{2}f_{ij}^{\mathrm{loss}}$ while the line flow measured at bus j is given by $-f_{ij} + \frac{1}{2}f_{ij}^{\mathrm{loss}}$. Often, line flows are required to stay within rated limits, which means that flow magnitude is important to model. The line flow magnitude is given by the following:

$$|f_{ij}| + \frac{1}{2}f_{ij}^{\mathrm{loss}} = \left|\frac{\theta_{ij} - \psi_{ij}}{a_{ij}x_{ij}}\right| + \frac{r_{ij}\Delta\theta}{2a_{ij}x_{ij}^2}\sum_{s=1}^S (2s-1)\theta_{ij}^{\mathrm{PW}}(s) \tag{2.67}$$

which, in matrix form, is expressed as:

$$|\mathbf{f}| + \frac{1}{2}\mathbf{f}^{\mathrm{loss}} = \left|X^{-1}(A^{\top}\theta - B^{\top}\psi)\right| + \frac{1}{2}X_l^{-1}C_l\theta^{\mathrm{PW}} \tag{2.68}$$

$$= X^{-1}\left|A^{\top}\theta - B^{\top}\psi\right| + \frac{1}{2}X_l^{-1}C_l\theta^{\mathrm{PW}} \leqslant u_{ij} \tag{2.69}$$

$$= X^{-1}\left|\theta^{+} - \theta^{-}\right| + \frac{1}{2}X_l^{-1}C_l\theta^{\mathrm{PW}}. \tag{2.70}$$

Notice that the convex relaxation of the absolute value complimentarity condition allows for a simple upper bound to be considered. Application of the triangle inequality to $|\theta^{+} - \theta^{-}|$ yields the following:

$$|\mathbf{f}| + \frac{1}{2}\mathbf{f}^{\mathrm{loss}} \leqslant X^{-1}(\theta^{+} + \theta^{-}) + \frac{1}{2}X_l^{-1}C_l\theta^{\mathrm{PW}} \tag{2.71}$$

$$= X^{-1}D_{\mathrm{PW}}\theta^{\mathrm{PW}} + \frac{1}{2}X_l^{-1}C_l\theta^{\mathrm{PW}} \tag{2.72}$$

$$= (X^{-1}D_{\mathrm{PW}} + \frac{1}{2}X_l^{-1}C_l)\theta^{\mathrm{PW}} \tag{2.73}$$

$$\implies \quad |\mathbf{f}| + \frac{1}{2}\mathbf{f}^{\mathrm{loss}} \leqslant K_l\theta^{\mathrm{PW}} \tag{2.74}$$

where $K_l = \mathrm{diag}(\mathbf{k}_1^{\top}, \ldots, \mathbf{k}_m^{\top}) \in \mathbb{R}^{m \times mS}$ is block-diagonal with

$$\mathbf{k}_e = \frac{1}{a_{ij}x_{ij}}\mathbf{1}_S + \frac{r_{ij}\Delta\theta}{2a_{ij}x_{ij}^2}\mathbf{c} \in \mathbb{R}^S. \tag{2.75}$$

If the goal of modeling flow magnitude is to stay below a thermal rating u_{ij} then $2m$ constraints are necessary:

$$|\mathbf{f}| + \frac{1}{2}\mathbf{f}^{\mathrm{loss}} \leqslant \mathbf{u} \implies \left\{ \begin{array}{c} \mathbf{f} + \frac{1}{2}\mathbf{f}^{\mathrm{loss}} \leqslant \mathbf{u} \\ -\mathbf{f} + \frac{1}{2}\mathbf{f}^{\mathrm{loss}} \leqslant \mathbf{u} \end{array} \right. . \tag{2.76}$$

However, as mentioned in [69], formulating the flow magnitude in terms of θ^{PW} yields only m constraints:

$$K_l\theta^{\mathrm{PW}} \leqslant \mathbf{u}. \tag{2.77}$$

Notice that the upper bound is tight (i.e. $|\mathbf{f}| + \frac{1}{2}\mathbf{f}^{\mathrm{loss}} = K_l\theta^{\mathrm{PW}}$) only if the absolute-value complimentarity conditions are satisfied (i.e. $\theta^{+\top}\theta^{-} = 0$). When the conditions are not satisfied, employing $K_l\theta^{\mathrm{PW}}$ will overestimate line flow magnitudes, which can result in fictitious congestion. That is, when the convex relaxation of line losses is not tight, the system is operated conservatively below $\mathbf{u}$ and, as a consequence, more expensively. Finding conditions which ensure a tight formulation is, therefore, important. Discussion of such conditions is included in Chapter IV.

2.4 Power generation and demand

The power injected into a node must equal the net flow leaving the node. In a power system, generators inject power into the network while loads and line losses consume power. Generation can represent conventional (i.e. natural gas and electric power plants) and renewable generation (i.e. wind, hydro, and solar), which have different power generating costs based on energy types. Renewable generation is often subject to high intermittency and is non-dispatchable, whereas, conventional generation is simply controllable. In addition, conventional generators are often subject to well-defined ramp-rate limits, which constrain how quickly generation can be increased and decreased. This section provides an overview of the models used in describing transmission systems with generators and loads and describes the power balance between supply and demand.

2.4.1 Generators

Let $g \in \Omega_i^G \subset \mathcal{C}$ be a generator at node i, where $\mathcal{C}$ is the set of generators in the system. Then, g injects power into the network at rate f_{G_g} to help supply the demand and meet resulting losses. Generator g is described by its state f_{G_g} (i.e. how much it produces) and by a reference f_G^{set}, which is the desired set-point. The dynamics associated with generator g are then given by

$$\dot{f}_{G_g}(t) = \frac{1}{T_g} \left(f_{G_g}^{\text{ref}}(t) - f_{G_g}(t) \right), \tag{2.78}$$

where T_g is a generator time-constant. Discretization with sampling time T_s yields:

$$f_{G_g}[k+1] = f_{G_g}[k] + \frac{T_s}{T_g} \left(f_{G_g}^{\text{ref}}[k] - f_{G_g}[k] \right) \tag{2.79}$$

Defining generator excitation $\Delta f_{G_g}[k]$ as

$$\Delta f_{G_g}[k] := \frac{T_s}{T_g} \left(f_{G_g}^{\text{ref}}[k] - f_{G_g}[k] \right) \tag{2.80}$$

yields the following simple conventional generator model:

$$f_{G_g}[k+1] = f_{G_g}[k] + \Delta f_{G_g}[k]. \tag{2.81}$$

Furthermore, conventional generation is often subject to ramp-rate limits, which constrain the rate at which power production can be increased or decreased. Let g have ramp-up and ramp-down rate limits $\tilde{R}_g^{\text{up}}$ and $\tilde{R}_g^{\text{down}}$ [MW/s], respectively, then

$$-\tilde{R}_g^{\text{down}} \leqslant \dot{f}_{G_g}(t) \leqslant \tilde{R}_g^{\text{up}}, \tag{2.82}$$

which, upon discretization, becomes

$$-T_s \tilde{R}_g^{\text{down}} =: R_g^{\text{down}} \leqslant \Delta f_{G_g}[k] \leqslant R_g^{\text{up}} := T_s \tilde{R}_g^{\text{up}}. \tag{2.83}$$

Finally, each conventional generator has pre-specified generation limits, $f_{G_g}^{\text{min}}, f_{G_g}^{\text{max}}$. Thus, the **full conventional generator model** is given by:

$$f_{G_g}[k+1] = f_{G_g}[k] + \Delta f_{G_g}[k] \tag{2.84}$$
$$f_{G_g}[k] \in [f_{G_g}^{\text{min}}, f_{G_g}^{\text{max}}] \tag{2.85}$$
$$\Delta f_{G_g}[k] \in [R_g^{\text{down}}, R_g^{\text{up}}]. \tag{2.86}$$

Now, consider power injections from non-dispatchable renewable generators $f_{G_g,r}$. Assume renewable generation responds instantaneously and is not subject to ramp-rate conditions. Then, the following embodies a simple **model of renewable generation** (i.e. wind-generating turbines).

$$f_{G_g,r}[k] = f_{G_g,r}^{\text{nom}}[k] - f_{G_g,r}^{\text{spill}}[k] \tag{2.87}$$
$$f_{G_g,r}^{\text{spill}}[k] \in [0, \alpha_{G_g,r}^{\text{spill}}] \subset [0, f_{G_g,r}^{\text{nom}}[k]] \tag{2.88}$$

where $f_{G_g,r}$ is the injected power from renewable generator g given available or predicted nominal wind power $f_{G_g,r}^{\text{nom}}$. Furthermore, the (partial) reduction of nominal power (i.e. spilled power) is denoted by the following relationships: $f_{G_g,r}^{\text{spill}} \leqslant \alpha_{G_g,r}^{\text{spill}} \leqslant f_{G_g,r}^{\text{nom}}$. That is, one cannot spill more renewable generation than what is nominally available.

2.4.2 Loads

Let $d \in \Omega_i^D \subset \mathcal{D}$ be a load at node i, where $\mathcal{D}$ is the set of loads in the system. Then, d consumes power from the network at rate f_{D_d}. Load d is described by a its state f_{D_d} (i.e. how much it consumes). The goal of the operator is (partly) to satisfy loads in the system, however, there are periods during which load cannot be fully supplied and must be (partially) reduced. This can be due to a sudden unexpected shortage of renewable energy coupled or increase in demand, stringent ramp-rate limits on generators or due to multiple lines or generators going out of service. The process of reducing load is termed "load shedding" and, herein, it is assumed that loads can be shed instantaneously by the system operator. Therefore, given predicted or actual nominal load $f_{D_d}^{\text{nom}}$, the **total power consumed by load** d at time k is

$$f_{D_d}[k] = f_{D_d}^{\text{nom}}[k] - f_{D_d}^{\text{shed}}[k]. \tag{2.89}$$
$$f_{D_d}^{\text{shed}}[k] \in [0, \alpha_{D_d}^{\text{shed}}] \subset [0, f_{D_d}^{\text{nom}}[k]] \tag{2.90}$$

where $f_{D_d}^{\text{shed}}[k] \leqslant \alpha_{D_d}^{\text{shed}}$ denotes the (partial) reduction in nominal load.

Remark II.10. Obviously, load-shedding requires a suitable cyber-infrastructure to transmit load-shed commands to customers. More advanced demand response and

load control techniques exist in literature, please see [73] and [74]. Such methods would complement the work in this dissertation and underlie the simple load-shedding commands proposed herein. That is, $f_{D_d}^{\text{shed}}$ could act as a reference signal to a more advanced load control scheme.

2.4.3 Energy Storage

Energy storage is available in many forms (e.g. hydrogen fuel cells, grid-scale battery systems, hydro) and energy storage devices can be located at various nodes throughout the network. Let $q \in \Omega_i^E \subset \mathcal{Q}$ be an energy storage device at node i, where $\mathcal{Q}$ is the set of storage devices in the system. Assume steady-state storage power values, a constant slope for $\dot{E}_p(t) = dE_p(t)/dt$, and treat storage interface as a conversion process with charging and discharging efficiencies $\eta_{c,q}$ and $\eta_{d,q}$, then the relationship between storage state-of-charge (SOC) and power injected/consumed by device q is

$$\dot{E}_q(t) = \frac{dE_q(t)}{dt} \approx e_q(t, Q_q)Q_q(t). \tag{2.91}$$

where the SOC switching mechanism e_q is defined as

$$e_q(t, Q_q) = \begin{cases} \eta_{c,q}, & \text{if } Q_q(t) \geqslant 0 \quad \text{(charge/standby)} \\ \frac{1}{\eta_{d,q}}, & \text{if } Q_q(t) < 0 \quad \text{(discharge)} \end{cases}. \tag{2.92}$$

Since energy storage devices have two distinct states of operation, charging and discharging, that achieve different efficiencies, energy storage devices introduce switches in the SOC formulation. The following reformulation of the SOC makes this non-convex nonlinearity more apparent:

$$\dot{E}_q(t) = \eta_{c,q}Q_{c,q}(t) + \frac{1}{\eta_{d,q}}Q_{d,q}(t) \tag{2.93a}$$

$$Q_q(t) = Q_{c,q}(t) + Q_{c,q}(t), \tag{2.93b}$$

$$0 = Q_{c,q}(t)Q_{c,q}(t) \tag{2.93c}$$

where the rate-limited charging (c) and discharging variables (d), $Q_{c,q} \in [0, \overline{Q}_c]$ and $Q_{d,q} \in [-\overline{Q}_d, 0]$, model the switching mechanism explicitly as a complimentarity condition in (2.93c). The nonlinear complimentarity condition ensures that q can either charge or discharge, but not both simultaneously. To circumvent the nonlinearity, a mixed-integer linear (MIL) formulation can be employed:

$$Q_{c,q}(t)Q_{c,q}(t) = 0 \iff \begin{cases} 0 \leqslant Q_{c,q} \leqslant \overline{Q}_c(1 - z_q) \\ -\overline{Q}_d z_q \leqslant Q_{d,q} \leqslant 0 \\ z_q \in \{0, 1\} \end{cases}. \tag{2.94}$$

where z_q is a binary integer. For example, if $z_q[k] = 1$, then $Q_{c,q}[k] \equiv 0$ and device q is consequently operating in discharging mode at time-step k. While the above

linear formulation is equivalent to the nonlinear complimentarity condition, the use of integers is generally not desired, as it greatly increases computational complexity.

To avoid utilizing integers in the linear model, one can remove the integer-restricted charging/discharging. This implies that simultaneous charging and discharging is now feasible and is equivalent to a convex relaxation of the original SOC model. Replace (2.93) with the strictly linear and continuous formulation:

$$\dot{E}_q(t) = \eta_{c,q} Q_{c,q}(t) + \frac{1}{\eta_{d,q}} Q_{d,q}(t), \tag{2.95a}$$

$$Q_q(t) = Q_{c,q}(t) + Q_{c,q}(t). \tag{2.95b}$$

Employing a Forward Euler Discretization to (2.95) admits linear continuous first-order discrete SOC dynamics that represents **the full linear energy storage model**:

$$E_q[k+1] = E_q[k] + T_s \eta_{ch,q} Q_{c,q}[k] + \frac{T_s}{\eta_{dis,q}} Q_{d,q}[k], \tag{2.96a}$$

$$Q_q[k] = Q_{c,q}[k] + Q_{d,q}[k] \tag{2.96b}$$

$$Q_{c,q}[k] \in [0, \overline{Q}_c], \ Q_{d,q}[k] \in [-\overline{Q}_d, 0]. \tag{2.96c}$$

Remark II.11. The MIL formulation of (2.93) is implemented in Chapter III to model non-simultaneous charging within the context of energy hubs. However, for systems with a large number of storage devices, due to the complexity of integer optimization in the MIL approach, the non-simultaneous charging model is abandoned in Chapter IV and replaced by the strictly continuous linear convex approximation (2.96). The effects of allowing simultaneous charging is discussed then.

2.4.4 Power balance

In addition to the physical properties of the power flow, any network must satisfy Kirchoff's First Law (also called the "power balance"). That is, the net flow into a node must equal the net flow out of the node. Generally, a node may have generators (f_G) and/or loads (f_D) available and, in a system with energy storage devices, the charging (discharging) corresponds to additional demands (injections) (Q_i). Therefore, the power balance equation is formulated as:

$$\sum_{d \in \Omega_i^D} f_{D_d}[k] - \sum_{g \in \Omega_i^G} f_{G_g}[k] + \sum_{j \in \Omega_i^N} f_{ij}^{total}[k] + \sum_{q \in \Omega_i^E} Q_q[k] = 0 \quad \forall i \in \mathcal{N} \tag{2.97}$$

where f_{ij}^{total} is the total flow on line (i, j) and is defined by

$$f_{ij}^{total} = f_{ij} + \frac{1}{2} f_{ij}^{loss}. \tag{2.98}$$

The power balance equation in (2.97) determines the net power generated or consumed at each node. In matrix form, power balance employs the node-arc adjacency

matrix A and corresponding load-, generator-, and storage-to-node mapping matrixes of appropriate dimensions:

$$A_D\mathbf{f}_D[k] - A_G\mathbf{f}_G[k] + A\mathbf{f}[k] + \frac{1}{2}|A|\mathbf{f}^{\text{loss}}k] + A_E\mathbf{Q}[k] = \mathbf{0}. \tag{2.99}$$

Remark II.12 (Power balance and frequency). For a detailed study on frequency control in power systems, please see [75]. Basically, when a generator injects electric power into the network to supply an electric load, it is achieved by a turbine that transfers mechanical power to the generator shaft. An imbalance between the mechanical and electrical power leads to a change in the generator's rotating speed and, therefore, begets deviations from nominal frequency. Due to the inertia of all rotating elements in the system, an abrupt change in power balance, in fact, leads to a smooth change in the system frequency. The role of frequency control is, therefore, to manage the mechanical power of generators to return system frequency to nominal.

The power balance equation, as stated in (2.97), reflects the electrical balance in the system but neglects mismatches between mechanical power and electrical demand. Thus, the frequency of the system is not considered and this dissertation assumes that frequency regulation is the concern of lower-level control, which operates on a scale of seconds.

However, optimization with respect to constrained network flows can produce infeasible scenarios (e.g. flow limited arcs separating demand and generation). To enable persistent feasibility, a slack variable is added for each node to capture any electrical mismatch:

$$A_D\mathbf{f}_D[k] - A_G\mathbf{f}_G[k] + A\mathbf{f}[k] + \frac{1}{2}|A|\mathbf{f}^{\text{loss}}k] + A_E\mathbf{Q}[k] = \Delta\mathbf{m}[k]. \tag{2.100}$$

where mismatch $\Delta\mathbf{m} = \text{col}(\Delta m_1, \ldots, \Delta m_n)$. For example, if a large generator trips or islanding occurs, mismatches are inevitable due to ramp-rate limits. These mismatches are considered in (2.100) and, therefore, the set of W island mismatches $\{\sum_{i\in\mathcal{N}_w}\Delta m_i\}_{w=1}^{W}$ represents a form of frequency perturbation with respect to each island in the system.

2.5   Conductor temperature model

For a 3-phase overhead transmission line (i, j) each conductor can be considered identical. Therefore, consider a conductor as a per-unit length thermal mass with continuous-time temperature dynamics.

$$\dot{T}(t) = \frac{1}{mC_p}\left(q_s(t) + f_{ij}^{\text{loss}}(t) - q_c(t, T(t)) - q_r(t, T(t))\right), \tag{2.101}$$

where T and f_{ij}^{loss} are the conductor temperature [C] and the active power loss per unit length [W/m], respectively, for conductor (i, j). The losses are calculated from Section 2.3.4 and divided by conductor length L_{ij} [m]. Alternatively, f_{ij}^{loss} can be

expressed in terms of conductor current as $f_{ij}^{\text{loss}}(t) = I(t)^2 R(T)$, where the resistance depends linearly on the temperature. However, since the temperature dynamics are much slower than the instantaneous power flows, for all practical purposes, the resistance $R(T)$ is a fixed parameter in power flow calculations and can be updated offline with the most recent temperature measurements. Per unit length values mC_p, q_s, q_c, and q_r represent conductor heat capacity [J/m-C], solar heat gain rate [W/m], conductive heat loss rate [W/m], and radiative heat loss rate [W/m], respectively. The heat loss and gain rates are calculated based on IEEE Standard 738 [76], which provides a method for calculating the current-temperature relationship of bare overhead transmission lines, given weather conditions. The model presented below is described in further detail in [76]. Since the thermal model is with respect to a single line (i, j), for simplifying notation, the index (i, j) and $\cdot_{ij}$ are excluded in this section.

The solar heat gain rate is given by position of sun with relationship to the transmission line and time of day and is independent of temperature:

$$q_s(t) = \alpha \sin(b(t)) L A_l Q_{SE}(t) \tag{2.102}$$

where

$\alpha =$ solar absorptivity $\in [0.23, 0.91]$.

$b =$ angle of incidence of sun's rays $\in [0, 1]$

$L =$ conductor length, m.

$A_l =$ area of conductor per unit length $\in [0.5, 5] \times 10^{-2}$ m^2/m.

$Q_{\text{SE}} =$ total radiated solar flux, W/m^2.

The conductive heat loss rate is strongly coupled to the conductor temperature and depends on parameters associated with air near conductor and wind speed and direction. The below equation describes the heat loss rate for low-wind conditions and provides a conservative calculation of heat loss rate:

$$q_c(t) = \left[1.01 + 0.0372 \left(\frac{D \rho_f V_w}{\mu_f} \right)^{0.52} \right] L k_f K_{\text{angle}}(T(t) - T_{\text{amb}}(t)) \tag{2.103}$$

where

$D =$ conductor diameter $\in [5, 50]$ mm.

$\rho_f =$ air density $\in [0.574, 1.293]$ kg/m^3.

$\mu_f =$ dynamic viscosity of air $\in [1.72, 2.17] \times 10^{-5}$ Pa-s.

$V_w =$ wind speed $\in [0.2, 1.5]$ m/s.

$k_f =$ thermal conductivity of air $\in [2.42, 3.17] \times 10^{-2}$ W/m-C.

K_{angle} = wind direction correction factor $\in [0.4, 1]$.

Temperature is coupled to the radiative heat loss rate:

$$q_r(t) = 1.78 \times 10^{-10} LDe \left((T(t) + 273)^4 - (T_{\text{amb}}(t) + 273)^4 \right) \tag{2.104}$$

where

e = emissivity $\in [0.23, 0.91]$.

Finally, the per-unit length heat capacity is determined by the different materials employed in the construction of the conductor. Traditional conductors are aluminum conductor steel-reinforced (ACSR) cables and are specific types of stranded cables made of aluminum and steel materials.

$$mC_p = \sum_{i=1}^{N_{\text{mat}}} m_{l,i} C_{p,i} \tag{2.105}$$

where

N_{mat} = number of materials used in constructing conductor.

$m_{l,i}$ = mass per unit length of material i, kg/m.

$C_{p,i}$ = specific heat capacity of material i, J/C-kg.

By employing conservative values for the many exogenous and physical parameters above, the thermal model simplifies to a function of conductor temperature (T), ambient temperature (T_{amb}) and sun exposure (q_s), and active power loss (i.e. f_{ij}^{loss}). The simplifying assumptions are:

- Wind-speed is low and fixed to 0.61 m/s perpendicular to line.

- Solar heat gain rate is constant and set to that of a sunny summer day.

- Ambient temperature is set to constant 25°C.

- Lines are aluminum conductor steel-reinforced (ACSR) cables:

  - Standard conductor look-up tables yield m and C_p values for aluminum and steel.

- Line and air constant parameters do not depend on conductor temperature.

  - Exception: conductor resistance $R(T)$ [Ω/m], which can be approximated as a linear function of temperature [48]:

    $$R(T) = R_0[1 + \alpha_R(T - T_0)] \tag{2.106}$$

    where

* $R_0 := R(T_0)$ is the reference resistance value at T_0 [Ω/m]
* T_0 is the reference temperature for R_0 [C]
* $\alpha_R = 0.0039$ is the thermal resistivity coefficient [1/C]

By appropriately applying the above assumptions, the temperature dynamics are described by:

$$\dot{T}(t) := \frac{1}{mC_p} F(q_s, f_{ij}^{\text{loss}}, T, T_{\text{amb}}) \tag{2.107}$$

$$= \frac{1}{mC_p} \left(q_s(t) + f_{ij}^{\text{loss}}(t) - \eta_c(T(t) - T_{\text{amb}}(t)) - \eta_r((T(t) + 273)^4 - (T_{\text{amb}}(t) + 273)^4) \right) \tag{2.108}$$

where mC_p, η_c, and η_r are positive constants and reflect assumed heat capacitive and solar, conductive, and radiative heat rate-related parameter values, respectively.

To allow for tractable implementation of the model-predictive control scheme, we linearize equation (2.108) around equilibrium point $T^* = T_{\text{lim}}$, where T_{lim} is computed from steady-state conditions with line at maximum current rating (i.e. set $f_{ij}^{\text{loss}*} = R(T)I_{\text{lim}}^2$) with T_{amb}^*, q_s^*. For details on how to calculate T_{lim}, please see Section 2.5.2.

Thus, a first-order Taylor approximation yields:

$$\Delta\dot{T} \approx \frac{1}{mC_p} \left(\Delta q_s \left.\frac{\partial F}{\partial q_s}\right|_{q_s^*} + \Delta f_{ij}^{\text{loss}} \left.\frac{\partial F}{\partial f_{ij}^{\text{loss}}}\right|_{f_{ij}^{\text{loss}*}} + \Delta T \left.\frac{\partial F}{\partial T}\right|_{T_{\text{lim}}} + \Delta T_{\text{amb}} \left.\frac{\partial F}{\partial T_{\text{amb}}}\right|_{T_{\text{amb}}^*} \right) \tag{2.109}$$

where linear terms are defined as

$$\Delta q_s(t) = q_s(t) - q_s^* \tag{2.110}$$

$$\Delta f_{ij}^{\text{loss}}(t) = f_{ij}^{\text{loss}}(t) - f_{ij}^{\text{loss}*} \tag{2.111}$$

$$\Delta T(t) = T(t) - T_{\text{lim}} \tag{2.112}$$

$$\Delta T_{\text{amb}}(t) = T_{\text{amb}}(t) - T_{\text{amb}}^*, \tag{2.113}$$

with derivatives given by

$$\left.\frac{\partial F}{\partial q_s}\right|_{q_s^*} = 1 \qquad \left.\frac{\partial F}{\partial T}\right|_{T_{\text{lim}}} = -(\eta_c + 4\eta_r(T_{\text{lim}} + 273)^3)$$
$$\left.\frac{\partial F}{\partial f_{ij}^{\text{loss}}}\right|_{f_{ij}^{\text{loss}*}} = 1 \qquad \left.\frac{\partial F}{\partial T_{\text{amb}}}\right|_{T_{\text{amb}}^*} = \eta_c + 4\eta_r(T_{\text{amb}}^* + 273)^3 \tag{2.114}$$

and the temperature dynamics take the form:

$$\Delta\dot{T}(t) = \frac{1}{mC_p} \left(\Delta q_s(t) + \Delta f_{ij}^{\text{loss}}(t) - (\eta_c + 4\eta_r(T_{\text{lim}} + 273)^3)\Delta T(t) \right. \tag{2.115}$$

$$+(\eta_c + 4\eta_r(T_{\text{amb}}^* + 273)^3)\Delta T_{\text{amb}}(t)\bigg)$$

$$= \frac{1}{mC_p} \left(\Delta q_s(t) + \Delta f_{ij}^{\text{loss}}(t) - \bar{\gamma}_c\Delta T(t) + \bar{\gamma}_a\Delta T_{\text{amb}}(t) \right). \tag{2.116}$$

Coefficients $\bar{\gamma}_c = \eta_c + 4\eta_r(T_{\text{lim}} + 273)^3$ and $\bar{\gamma}_a = \eta_c + 4\eta_r(T_{\text{amb}}^* + 273)^3$. Employing standard Euler forward discretization with sampling-period T_s, the discrete-time temperature dynamics are obtained:

$$\Delta T[k+1] = \Delta T[k] + \frac{T_s}{mC_p} \left(\Delta q_s[k] + \Delta f_{ij}^{\text{loss}}[k] - \bar{\gamma}_c\Delta T[k] + \bar{\gamma}_a\Delta T_{\text{amb}}[k] \right) \tag{2.117}$$

$$= \tau\Delta T[k] + \rho\Delta f_{ij}^{\text{loss}}[k] + \rho\Delta q_s[k] + \gamma\Delta T_{\text{amb}}[k], \tag{2.118}$$

where $\tau = 1 - \frac{T_s\bar{\gamma}_c}{mC_p}$, $\gamma = \frac{T_s\bar{\gamma}_a}{mC_p}$, and $\rho = \frac{T_s}{mC_p}$ [m-C/W]. For stability, it is required that $\tau \in (-1, 1)$, which implies the sampling time must satisfy $T_s < 2\frac{mC_p}{\bar{\gamma}_c}$. Since each line (i, j) is subject to its own temperature dynamics, the notation becomes:

$$\Delta T_{ij}[k+1] = \tau_{ij}\Delta T_{ij}[k] + \rho_{ij}\Delta f_{ij}^{\text{loss}}[k] + \rho_{ij}\Delta q_s[k] + \gamma_{ij}\Delta T_{\text{amb}}[k] \tag{2.119}$$

$$= \tau_{ij}\Delta T_{ij}[k] + \rho_{ij}\Delta f_{ij}^{\text{loss}}[k] + \begin{bmatrix} \rho_{ij} & \gamma_{ij} \end{bmatrix} \begin{bmatrix} \Delta q_s[k] \\ \Delta T_{\text{amb}}[k] \end{bmatrix} \tag{2.120}$$

$$= \tau_{ij}\Delta T_{ij}[k] + \rho_{ij}\Delta f_{ij}^{\text{loss}}[k] + \hat{\rho}_{ij}^\top\Delta d[k] \tag{2.121}$$

where, without loss of generality, the ambient temperature and solar heat-gain rate can be considered identical (exogenous inputs) for all lines in $\mathcal{E}$.

2.5.1 Thermal model in matrix form

Since each transmission line $(i, j) \in \mathcal{E}$ has its own temperature state and losses, and exogenous conditions (ambient temperature and solar radiation) are considered identical for each line (i.e. disturbance inputs), the thermal model is formulated with the following matrix notation:

$$\Delta\mathbf{T}[k+1] = A_\tau\Delta\mathbf{T}[k] + B_\rho\Delta\mathbf{f}^{\text{loss}}[k] + \mathbf{b}_\rho\Delta q_s[k] + \mathbf{b}_\gamma\Delta T_a[k], \tag{2.122}$$

where $\Delta\mathbf{T}[k] \in \mathbb{R}^m, \Delta\mathbf{f}^{\text{loss}}[k] \in \mathbb{R}^m, \Delta q_s[k] \in \mathbb{R}, \Delta\mathbf{T}_a[k] \in \mathbb{R}$, and for all $(i,j) \in \mathcal{E}$ and $m = |\mathcal{E}|$,

$$A_\tau = \underset{(i,j)\in\mathcal{E}}{\text{diag}}(\tau_{ij}) \in \mathbb{R}^{m\times m} \tag{2.123}$$

$$B_\rho = \underset{(i,j)\in\mathcal{E}}{\text{diag}}(\rho_{ij}) \in \mathbb{R}^{m\times m} \tag{2.124}$$

$$\mathbf{b}_\rho = \underset{(i,j)\in\mathcal{E}}{\text{col}}(\rho_{ij}) \in \mathbb{R}^m \tag{2.125}$$

$$\mathbf{b}_\gamma = \underset{(i,j)\in\mathcal{E}}{\text{col}}(\gamma_{ij}) \in \mathbb{R}^m. \tag{2.126}$$

2.5.2 Calculating conductor temperature limit (T_{lim})

Given a three-phase transmission line's steady-state (i.e. continuous) thermal rating, u_{max} [VA], and the base voltage, V_b [V], the ampacity (i.e. current capacity) I_{lim} [A] is calculated as follows:

$$I_{\text{lim}} = \frac{u_{\text{max}}}{\sqrt{3}V_b}. \tag{2.127}$$

Furthermore, given the per-unit-length series resistance $R(T)$ and other physical conductor parameters (e.g. diameter, mass) and conservative estimates of exogenous parameters (e.g. solar and wind), one can describe the per-unit-length heat loss and gain rates at steady state as a function of temperature T. This implies that the heat loss and gain rates per unit length at steady state can be described as a function of T. Since the nonlinear steady-state equation in (2.128) is quartic with respect to T, it has no straight-forward closed-form solution, so numerical methods are utilized to calculate the temperature T that satisfies the steady-state heat balance equation:

$$0 = q_s + R(T)I_{\text{lim}}^2 - \eta_c(T - T_{\text{amb}}) - \eta_r((T + 273)^4 - (T_{\text{amb}} + 273)^4) \tag{2.128}$$

The resulting temperature represents the temperature limit of the conductor and is denoted T_{lim}. With T_{lim} given, it is straightforward to can solve (2.128) for I_{lim} and compute the resulting ampacity of the conductor.

2.5.3 Numerical example

The IEEE Standard transmission-line temperature model described above is simulated for an ACSR 26/7 Drake conductor. In particular, the simulation investigates the conductor temperature response to step-changes in current I_{ij}. Salient parameters are included in Table 2.2 and Figure 2.6 illustrates the conductor response. While the coupling between temperature and resistance is non-trivial, in this numerical example, the resistance is fixed to a constant. That is, $R(T) \equiv R_0$.

The 3-phase transmission line rating is given as $u_{ij} = 500$ MVA and, from Section 2.5.2, the conductor ampacity is calculated as $I_{\text{lim}} = 1255$ A (i.e. 5 pu at $V_b = 230$ kV) with an associated temperature limit of $T_{\text{lim}} = 99°$C. The nonlinear temperature

Table 2.2: Simulation parameters used in numerical example.

Parameter	Value	Unit
Sampling Time, T_{s}	60	s
Specific heat capacity (steel), $C_{p,st}$	490	J/(kg-C)
Specific heat capacity (aluminum), $C_{p,alu}$	910	J/(kg-C)
Mass per unit length (Drake, steel), $m_{l,st}$	0.512	kg /m
Mass per unit length (Drake, aluminum), $m_{l,alu}$	1.115	kg /m
Diameter (Drake), D	28.12	mm
Resistance (Drake), R_0	6.09×10^{-5}	Ω/m
Base voltage, V_b	230	kV
Air density, ρ_f	1	kg/m^3
Air dynamic viscosity, μ_f	0.03,	Pa-s
Air thermal conductivity, k_f	2×10^{-5}	W/m-C
Wind speed, V_w	0.61	m/s
Wind direction angle w.r.t. line, ϕ_w	90	degrees
Conductor elevation, H_e	61	m
Emissivity, ϵ	0.7	-
Ambient temperature, T_{amb}	35	C
Day of the year (for sun intensity), N_{day}	160 (6/10)	-
Hour of the day (for sun position), h_{day}	12 (Noon)	-
Line latitude, Lat	40	degrees
Line azimuth, Z_l	90	degrees
Solar absorptivity, α	0.9	-

model is then linearized around operating point ($T_{\mathrm{lim}}^* = 99, I_{\mathrm{lim}}^* = 1255, T_{\mathrm{amb}}^* = 35, q_s^* = 26.1$ W/m). The conductor current undergoes step-changes between 0 to $2I_{\mathrm{lim}}$ as shown in Figure 2.6a. Figure 2.6b illustrates that the linear and nonlinear models are interchangeable for temperatures $T[k] \in (80, 120)$. Incorporating variable resistance decreases this margin. Finally, Figure 2.6c displays the ohmic losses in the conductor relative to active power on conductor. The losses are small for currents close to or below I_{lim}.

Overall, this example illustrates that the linear model is a reasonable approximation for temperatures near T_{lim}.

2.6 Summary

This chapter describes the basic models used in power systems. These models describe AC, DC, and lossy DC-based power flows, energy storage devices, loads, and generators, as well as, transmission line conductors. Chapter III proposes an optimization framework for modeling large-scale multi-energy systems and introduces the "energy hub" concept. In Chapter IV, model-predictive control problems are
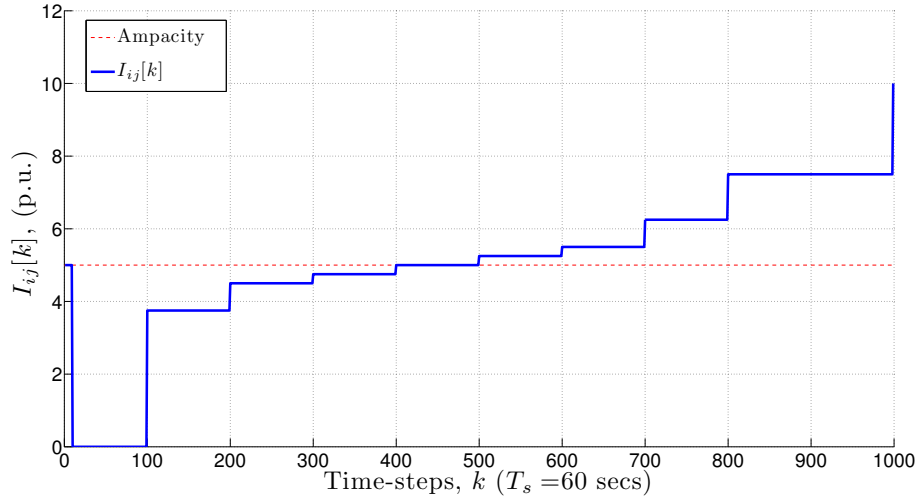
(a) Conductor current step-changes in per unit.
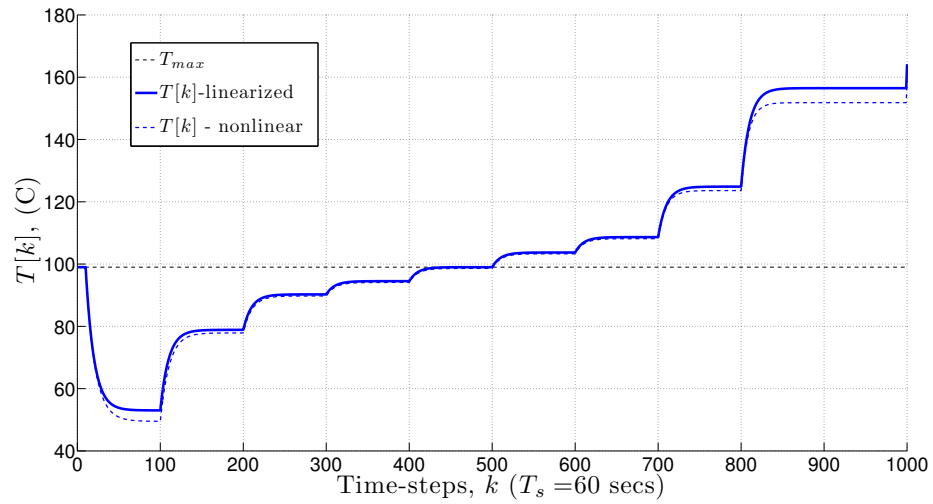
(b) Linear and nonlinear temperature response to current input.
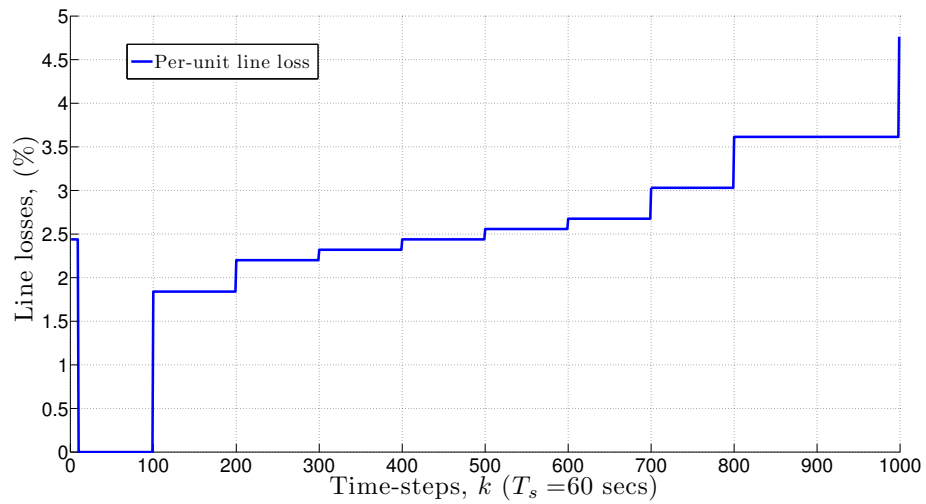
(c) Relative line losses.

Figure 2.6: Thermodynamical conductor response to step-changes in current I_{ij}.

formulated which employ most of the models presented herein to alleviate the effects of cascading outages.

CHAPTER III

Analysis of Energy Hub Networks

3.1 Introduction

Recent events have placed a renewed focus on the reliability and optimality of energy supply systems [28]. Such systems involve interconnections between the electrical network and various energy carriers, such as natural gas, water, and wind energy. For example, electricity produced from thermal generators involve large amounts of water and, as was the case in Australia, a drought negatively affected the electric production capabilities [77]. This interconnectedness of energy systems motivates the concept of the energy hub. Energy hub concepts provide a modeling framework for extending beyond specific energy carrier combinations, such as hydrothermal systems, allowing analysis and optimization of an arbitrary array of energy carriers. Modeling the coupling energy carriers may reveal minimum cost solutions, and also vulnerabilities, that are not apparent when each energy system is treated separately.

While past literature has focused on the energy hub formulation and small coupled energy carrier networks (2-6 hubs), this chapter is directed towards large-scale coupled multi-energy networks (100s of hubs). Through a linear reformulation of the energy hub model, this chapter takes advantage of its mathematical structure to develop a concise format that fully describes general large-scale energy hub systems. The format allows for simple automatic implementation and analysis of multi-energy systems. This methodology is then explored in Chapter IV within a model-predictive control setting to investigate resilience of large multi-energy systems under severe disturbances.

The work presented in this chapter appears in the Proceedings of the 17th Power Systems Computation Conference [78].

3.2 Multi-energy system example

As mentioned in Section 1.2.1, a multitude of approaches exists for formulating multi-carrier energy networks. This chapter focuses discussions on the systems-based "hybrid energy hub" model developed in [15]. Essentially, energy can enter an energy hub from multiple attached networks, undergo various lossy conversion and/or storage processes, and exit the hub to adjacent energy networks or loads. One can consider
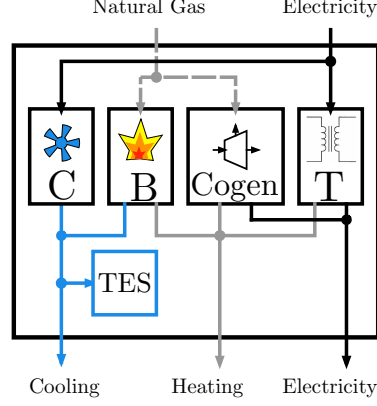
Figure 3.1: An example of a central utility plant with thermal storage modeled as an energy hub.

energy hubs as being representative of cities, universities, hospitals, military bases, or even personal homes where energy demands, generation, and transport are multi-energy in nature. An illustrative example of an energy hub is given in Figure 3.1, where a fictitious central utility plant (CUP) is modeled as an energy hub. The hub is an interface between standard utilities (natural gas and electricity) and local cooling, heating, and electric loads. The CUP utilizes a chiller sub-system (C), a boiler sub-system (B), a cogeneration facility (Cogen), and distribution-level transformer (T). The chiller sub-system converts electricity into cooling through a refrigeration cycle. The boiler sub-system can convert natural gas into district heating (via boilers) and/or cooling (via absorption chillers). The co-generator employs a furnace and steam turbine to generate hot steam (for heating) and electricity, respectively. In this example, a transformer has been retrofitted with a waste heat recovery unit that captures ohmic transformer losses in the form of heat. Finally, the produced cooling can be stored in a thermal energy storage (TES) device, such as ice storage. Losses associated with each conversion and storage process may be variable depending on efficiency parameters and input / output levels. The relationship between energy input P and energy output L in the CUP example is defined by the following:

- **Inputs:**

$$P_{\text{nat gas}} = P_{\text{nat gas},B} + P_{\text{nat gas},Cogen} \tag{3.1}$$

$$P_{\text{el}} = P_{\text{el},C} + P_{\text{el},T} \tag{3.2}$$

- **Outputs:**

$$L_{\text{cool}} = C_{C,\text{el}\rightarrow\text{cool}}P_{\text{el},C} + C_{B,\text{nat gas}\rightarrow\text{cool}}P_{\text{nat gas},B} + Q_{TES,\text{cool}} \tag{3.3}$$

$$L_{\text{heat}} = C_{C,\text{el}\rightarrow\text{heat}}P_{\text{el},T} + C_{B,\text{nat gas}\rightarrow\text{heat}}P_{\text{nat gas},B} \tag{3.4}$$

$$+ C_{Cogen,\text{nat gas}\rightarrow\text{heat}}P_{\text{nat gas},Cogen}$$

$$L_{\text{el}} = C_{Cogen,\text{nat gas}\rightarrow\text{el}}P_{\text{nat gas},Cogen} + C_{T,\text{el}\rightarrow\text{el}}P_{\text{el},T} \tag{3.5}$$

43
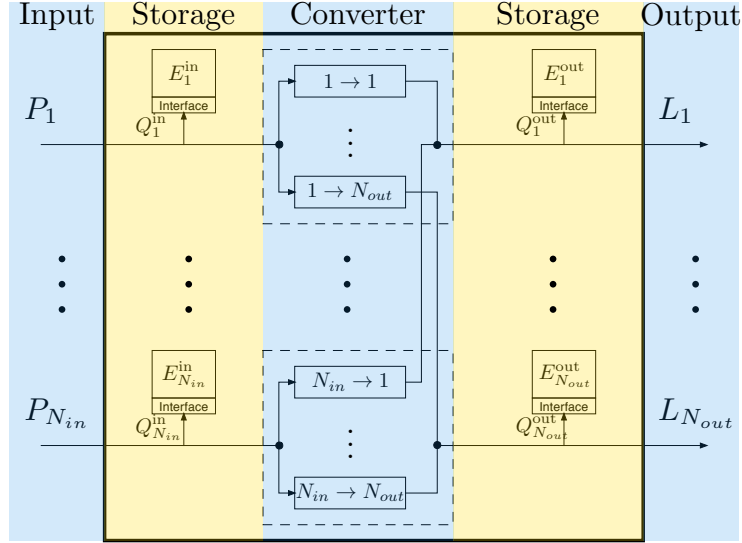
Figure 3.2: A generalized energy hub model illustrating all possible energy-conversion paths and the five major hub building blocks: input sources, input storage, converters, output storage, and output sinks.

where $C_{x,y \to z}$ is the conversion efficiency of converting y to z in converter x and $Q_{TES,\text{cool}}$ is the charging (< 0) or discharging (> 0) of cooling from TES device. Further details on modeling of energy hubs are included below and this example will be revisited then.

3.3 Modeling the Energy Hub

In the example of Figure 3.1, a CUP operator may utilize the TES device for peak-shaving to minimize electricity costs or employ the absorptions chillers in the boiler sub-system to provide cheap cooling. Such scenarios can be tabulated based on the control actions available for a CUP operator. The variables associated with a general energy hub can be classified into independent (control/decision) variables, dependent (state) variables, and constant hub parameters. The decision variables are those quantities that a system or hub controller can directly manipulate.

3.3.1 Nomenclature

Most common energy hubs can be constructed from interconnections of five simple building blocks: input energy sources, input energy storage, energy converters, output energy storage, and output energy sinks. These five building blocks are illustrated in Figure 3.2. In describing the flow of energy from hub input to hub output, there is a need to consider the flow between each of the five blocks of the hub. Let $h \in \mathscr{H}$ be a hub from the set of available hubs, where h has input sources $i \in \{1, 2, \ldots, N_{in}\}$ and output sources $n \in \{1, 2, \ldots, N_{out}\}$.

The main mathematical symbols used in this chapter to describe the energy hub model are classified below for quick reference.

44

Table 3.1: Classification of variables in an energy hub

Variable Type	Variables
Decision	$\widehat{P}_{ij}, Q_i^{\text{in}}, Q_n^{\text{out}}$
Dependent	$P_i, E_i^{\text{in}}, E_n^{\text{out}}, L_n$
Constant Parameter	$C_{ijn}, \eta_{\text{c},i}^{\text{in}}, \eta_{\text{d},i}^{\text{in}}, \eta_{\text{c},n}^{\text{out}}, \eta_{\text{d},n}^{\text{out}}$

P_i - hub energy flow input i.

Q_i^{in} - hub input-side energy storage flow from input i.

E_i^{in} - hub input-side energy storage state-of-charge at input i.

$\eta_{\text{c/d},i}^{\text{in}}$ - hub storage interface charge (c) / discharge (d) efficiencies at input i.

$\widehat{P}_{ij}$ - hub dispatch energy flow from input i directed to converter j.

C_{ijn} - efficiency of converting energy input i into output type n through converter j.

Q_n^{out} - hub output-side energy storage flow to output n.

$\eta_{\text{c/d},n}^{\text{out}}$ - hub storage interface charge (c) / discharge (d) efficiencies at output n.

E_n^{out} - hub output-side energy storage state-of-charge at output n.

L_n - hub energy flow output n.

Table 3.1 categorizes the variables that arise in the energy hub model and are described in detail in the following sections. Within the proposed modeling framework, generation, conversion, and energy storage utilization processes can be controlled. Efficiencies related to conversion and storage charging/discharging processes are, generally, variable based on flow rates. However, for the purposes of the work herein, analysis assumes constant efficiencies. Therefore, the corresponding hub efficiencies are considered as constant parameters. Note that due to the profusion of notation, slight abuses of the notation presented in Chapter II are inevitable.

3.3.2 Formulating a linear model

Let P_i be the input flow from source i at hub h. Referring to Figure 3.3a, to describe the flow from input source i to a converter j, we have to take into account any input storage devices and possible dispatch factors. The dispatch factors $\nu_{ij} \in [0, 1]$ determine the dispatch flows $\widehat{P}_{ij}$, which describe the amount of input flow i that is directed to converter j.

From Figure 3.3a, it is straightforward to see that

$$P_i = Q_i^{in} + \sum_{j=1}^{k_i} \widehat{P}_{ij} \tag{3.6}$$

(a) From input to converters.   (b) From converters to output.
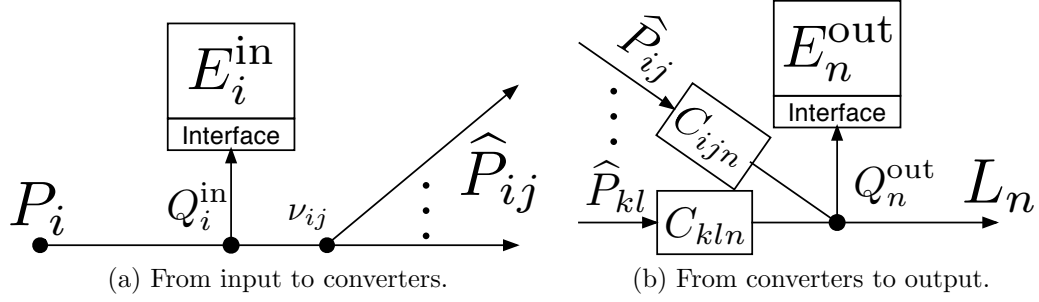
Figure 3.3: Decomposing the energy hub model based on dispatch flows.

where Q_i^{in} is the flow into input storage device i and $\widehat{P}_{ij}$ is one of the k_i flows determined by the dispatch factors, ν_{ij}, such that

$$\widehat{P}_{ij} = \nu_{ij}(P_i - Q_i^{in}) \tag{3.7}$$

and

$$\sum_{j=1}^{k_i} \nu_{ij} = 1, \qquad 0 \leqslant \nu_{ij} \leqslant 1. \tag{3.8}$$

Note that (3.8) ensures conservation of flow between input storage and converter blocks. Employing (3.7) and (3.8), one can eliminate dispatch factors ν_{ij} to obtain

$$0 \leqslant \widehat{P}_{ij} \leqslant P_i - Q_i^{in}. \tag{3.9}$$

Referring to Figure 3.3b, output flows L_n are obtained by converting dispatch flows $\widehat{P}_{ij}$. Converter C_{ijn} converts the j-th dispatch flow of input source i into output source n. The output flows L_n must also take into account any output storage device flow, Q_n^{out}. Thus, modeling hub output flows gives,

$$\sum_{i} \sum_{j \in \mathcal{D}(i,n)} C_{ijn} \widehat{P}_{ij} = Q_n^{out} + L_n. \tag{3.10}$$

where $\mathcal{D}(i, n)$ is the set of dispatch flows from input i that can be converted to output n, and $|\mathcal{D}(i, n)| \leqslant k_i$.

The previous analysis did not consider the effects of storage flows on state-of-charge (SOC). With regard to input and output energy storage devices, one must consider multiple time periods since, for energy source p, the SOC at time $k + 1$, depends on the SOC in the previous time step k. To simplify notation, input and output storage denotations, $(.)^{\text{in/out}}$, are omitted here. For energy storage, assume:

- steady-state storage power values

- a constant slope for $\dot{E}_p(t) = dE_p(t)/dt$, and

- treat storage interface as a converter device with charging and discharging efficiencies $\eta_{c,p}$ and $\eta_{d,p}$,

then employing the mixed-integer linear storage model, based on (2.93) and (2.94), yields the following linear relationship between storage flows Q_p and the state-of-charge E_p:

$$E_p[k+1] = E_p[k] + \eta_{c,p}Q_{c,p}[k] + \frac{1}{\eta_{d,p}}Q_{d,p}[k] \tag{3.11}$$

$$Q_p[k] = Q_{c,p}[k] + Q_{d,p}[k] \tag{3.12}$$

with

$$-(1 - z_p[k])\underline{Q}_p \leqslant Q_{d,p}[k] \leqslant 0 \tag{3.13}$$

$$0 \leqslant Q_{c,p}[k] \leqslant z_p[k]\,\overline{Q}_p \tag{3.14}$$

where $z_p[k] \in \{0, 1\}$, and $\overline{Q}_p$ and $\underline{Q}_p$ are constant limits on the flow into and out of device p. Thus, when $z_p[k] \equiv 0$, storage device p is in discharging mode at time k (as $Q_{c,p}[k] \equiv 0$), while $z_p[k] \equiv 1$ implies p is in charging mode (with $Q_{p,dis}[k] \equiv 0$) at time k.

3.3.3 Matrix notation for energy hub model

Consider discrete time-steps k. From (3.6) and (3.9), the relationship between input sources and input storage can be written in matrix form as,

$$\mathbf{P}_h[k] = \mathbf{S}_h^{in}\mathbf{Q}_h^{in}[k] + \mathbf{F}_h\hat{\mathbf{P}}_h[k] \tag{3.15}$$

with

$$\mathbf{0} \leqslant \hat{\mathbf{P}}_h[k] \leqslant \mathbf{F}_h^\top(\mathbf{P}_h[k] - \mathbf{S}_h^{in}\mathbf{Q}_h^{in}[k]) \tag{3.16}$$

for all $h \in \mathcal{H}$ where $\mathbf{S}_h^{in}$ is the *input storage coupling matrix* and $\mathbf{F}_h$ is the *dispatch flow matrix*.

From (3.10), the output flows for hub h can be written in matrix form as,

$$\mathbf{L}_h[k] = \mathbf{C}_h\hat{\mathbf{P}}_h[k] + \mathbf{S}_h^{out}\mathbf{Q}_h^{out}[k] \tag{3.17}$$

for all $h \in \mathcal{H}$ where $\mathbf{C}_h$ is the *converter coupling matrix* and $\mathbf{S}_h^{out}$ is the *output storage coupling matrix*.

The input-output agnostic energy storage equations as defined in (3.11) and (3.12), yield matrix equations:

$$\mathbf{E}_h[k+1] = \mathbf{E}_h[k] + \mathbf{N}_{c,h}\mathbf{Q}_{c,h}[k] + \mathbf{N}_{d,h}\mathbf{Q}_{d,h}[k] \tag{3.18}$$

$$\mathbf{Q}_h[k] = \mathbf{Q}_{c,h}[k] + \mathbf{Q}_{d,h}[k] \tag{3.19}$$

for all $h \in \mathcal{H}$ where $\mathbf{N}_{c,h} = \text{diag}(\eta_{c,1}, \ldots, \eta_{c,N})$ and $N_{d,h} = \text{diag}(1/\eta_{d,1}, \ldots, 1/\eta_{d,N})$ are diagonal matrices of charging and discharging efficiencies, respectively.

Furthermore, since each hub h is completely described by its local matrices $\mathbf{S}_h^{in}$,

$\mathbf{F}_h$, $\mathbf{C}_h$, and $\mathbf{S}_h^{out}$, each hub is decoupled and one can describe the entire set of hubs $\mathscr{H}$ by constructing block-matrices from the h-specific matrices. For example, the converter coupling matrix for the entire set $\mathscr{H}$ is defined by:

$$\mathbf{C} = \begin{pmatrix} \mathbf{C}_1 & 0 & \cdots & 0 \\ 0 & \mathbf{C}_2 & \ddots & \vdots \\ \vdots & \ddots & \ddots & 0 \\ 0 & \cdots & 0 & \mathbf{C}_{|\mathscr{H}|} \end{pmatrix}.$$

Thus, the following (mixed-integer) linear relations fully describe a general class of energy hubs and hold for all time-steps k:

$$\mathbf{P}[k] = \mathbf{S}_{in}\mathbf{Q}^{in}[k] + \mathbf{F}\hat{\mathbf{P}}[k] \tag{3.20a}$$

$$\mathbf{L}[k] = \mathbf{C}\hat{\mathbf{P}}[k] + \mathbf{S}^{out}\mathbf{Q}^{out}[k] \tag{3.20b}$$

$$\mathbf{E}^{in}[k+1] = \mathbf{E}^{in}[k] + \mathbf{N}_{\mathrm{c}}^{in}\mathbf{Q}_{\mathrm{c}}^{in}[k] + \mathbf{N}_{\mathrm{d}}^{in}\mathbf{Q}_{\mathrm{d}}^{in}[k] \tag{3.20c}$$

$$\mathbf{E}^{out}[k+1] = \mathbf{E}^{out}[k] + \mathbf{N}_{\mathrm{c}}^{out}\mathbf{Q}_{\mathrm{c}}^{out}[k] + \mathbf{N}_{\mathrm{d}}^{out}\mathbf{Q}_{\mathrm{d}}^{out}[k] \tag{3.20d}$$

$$\mathbf{Q}^{in}[k] = \mathbf{Q}_{\mathrm{c}}^{in}[k] + \mathbf{Q}_{\mathrm{d}}^{in}[k] \tag{3.20e}$$

$$\mathbf{Q}^{out}[k] = \mathbf{Q}_{\mathrm{c}}^{out}[k] + \mathbf{Q}_{\mathrm{d}}^{out}[k] \tag{3.20f}$$

with

$$\mathbf{0} \leqslant \hat{\mathbf{P}}[k] \leqslant \mathbf{F}^{\top}\mathbf{P}[k] - \mathbf{F}^{\top}\mathbf{S}_{in}\mathbf{Q}^{in}[k] \tag{3.20g}$$

$$\mathbf{0} \leqslant \mathbf{Q}_{\mathrm{c}}^{in}[k] \leqslant \overline{\mathbf{Q}}^{in}\mathbf{z}^{in}[k] \tag{3.20h}$$

$$-\underline{\mathbf{Q}}^{in}(\mathbf{1} - \mathbf{z}^{in}[k]) \leqslant \mathbf{Q}_{\mathrm{d}}^{in}[k] \leqslant \mathbf{0} \tag{3.20i}$$

$$\mathbf{0} \leqslant \mathbf{Q}_{\mathrm{c}}^{out}[k] \leqslant \overline{\mathbf{Q}}^{out}\mathbf{z}^{out}[k] \tag{3.20j}$$

$$-\underline{\mathbf{Q}}^{out}(\mathbf{1} - \mathbf{z}^{out}[k]) \leqslant \mathbf{Q}_{\mathrm{d}}^{out}[k] \leqslant \mathbf{0} \tag{3.20k}$$

$$z_i^{in}[k], z_n^{out}[k] \in \{0, 1\} \qquad \forall i, n. \tag{3.20l}$$

This formulation is mixed-integer because the elements of $\mathbf{z} = \mathrm{col}(z_1, \ldots, z_N)$ are binary variables that determine charging or discharging behavior of energy storage devices at each time-step k. Note that diagonal matrices $\overline{\mathbf{Q}} = \mathrm{diag}(\overline{Q}_1, \ldots, \overline{Q}_N)$ and $\underline{\mathbf{Q}} = \mathrm{diag}(\underline{Q}_1, \ldots, \underline{Q}_N)$ represent the energy storage charge and discharge power limits, respectively.

Remark III.1 (Value of proposed (MI)LP hub formulation)**.** The significant difference between the linear formulation of the energy hub model presented in equations (3.20a) and (3.20b), and the common input-to-output hub equation developed in [14] and repeated here:

$$\mathbf{L}_h = \mathbf{C}_h\mathbf{P}_h - \mathbf{S}_h\mathbf{Q}_h, \tag{3.21}$$

is that the formulation developed in this chapter explicitly takes into account the dispatch factor flows, and, therefore, the four matrices $\mathbf{S}_h^{in}$, $\mathbf{F}_h$, $\mathbf{C}_h$, and $\mathbf{S}_h^{out}$ are all constant. In the case of (3.21), the matrices $\mathbf{C}_h$ and $\mathbf{S}_h$ depend on the dispatch fac-

tor control variables ν_{ij}, which introduces nonlinearities. Thus, along with a linear reformulation of energy storage via the proposed mixed-integer charge/discharge formulation, a strictly linear, yet, equivalent description for hub h has been constructed in this chapter. The linear model is amenable to straightforward (mixed-integer) linear optimization and guarantees that optimal solutions are globally optimal. In addition, the mixed-integer formulation of the energy storage model can be relaxed depending on the optimization problem and, therefore, the linear hub formulation proposed in this chapter enables a strictly linear and continuous hub model. Having a linear model permits large-scale simulations of multi-energy systems, which is explored in Chapter IV.

3.3.3.1 Multi-energy system example revisited

To illustrate the matrix notation, apply the energy hub matrix formulation to the multi-energy example discussed in Section 3.2. First, denote the input/output energy sources, converters, and storage by the following indices:

Input sources:	$\{\text{natural gas, el}\} := \{1, 2\}$	(3.22)
Converters:	$\{\text{C, B, Cogen, T}\} := \{1, 2, 3, 4\}$	(3.23)
Output sources:	$\{\text{cooling, heating, el}\} := \{1, 2, 3\}$	(3.24)
Storage:	$\{\text{TES}\} := \{1\}.$	(3.25)

Then, the matrices that relate input $\mathbf{P}$ and output $\mathbf{L}$ are given by:

$$\mathbf{P} = \begin{bmatrix} P_1 \\ P_2 \end{bmatrix} = \begin{bmatrix} 1 & 1 & 0 & 0 \\ 0 & 0 & 1 & 1 \end{bmatrix} \begin{bmatrix} \hat{P}_{12} \\ \hat{P}_{13} \\ \hat{P}_{21} \\ \hat{P}_{24} \end{bmatrix} \tag{3.26}$$

$$= \mathbf{F}\hat{\mathbf{P}}$$

$$\mathbf{L} = \begin{bmatrix} L_1 \\ L_2 \\ L_3 \end{bmatrix} = \begin{bmatrix} C_{121} & 0 & C_{211} & 0 \\ C_{122} & C_{132} & 0 & C_{242} \\ 0 & 0 & 0 & C_{243} \end{bmatrix} \begin{bmatrix} \hat{P}_{12} \\ \hat{P}_{13} \\ \hat{P}_{21} \\ \hat{P}_{24} \end{bmatrix} + \begin{bmatrix} -1 \\ 0 \\ 0 \\ 0 \end{bmatrix} \begin{bmatrix} Q_1 \end{bmatrix} \tag{3.27}$$

$$= \mathbf{C}\hat{\mathbf{P}} + \mathbf{S}^{out}\mathbf{Q}^{out}.$$

Remark III.2. Notice how the dispatch flow matrix $\mathbf{F}$ is block-diagonal with each block given by a row-vector of ones. This holds true in general as well, since the sum of dispatch flows must equal the input source flow. That is, $\mathbf{F} = \mathrm{diag}(\mathbf{1}_1^\top, \ldots, \mathbf{1}_{N_{in}}^\top)$ where $\mathbf{1}_i = \mathrm{col}(1, \ldots, 1)$ is a column vector of ones with length equal to the number of dispatch factors for input source $i \in \{1, \ldots, N_{in}\}$. Furthermore, the converter coupling matrix $\mathbf{C}$ exhibits a specific output energy source for each row and a unique converter for each columns. Thus, entry (n, j) in $\mathbf{C}$ describes how much converter j participates production of energy source n. Finally, the $\mathbf{S}^{out}$ matrix utilizes a -1 since discharging

is a negative quantity that increases corresponding hub output.

3.4   Interconnection of Energy Hubs

Energy hubs are interconnected via adjacent energy supply networks. The previous section defined how power flowed *through* an energy hub from input to output. To describe the flow of energy *between* hubs, it is generally necessary to include power networks, which are described in detail in Section 2.4. A power network is a simple graph with additional physical constraints corresponding to the specific nature of the network, e.g. electrical or natural gas. Define the sets of generator and load nodes as $\mathcal{C}, \mathcal{D} \subset \mathcal{N}$ where generator nodes inject power into the network while load nodes consume power from the network. The remaining nodes are called throughput nodes and neither inject nor consume power. Every network must satisfy flow balance. That is, the sum of flows into and out of node i must equal the flow injected G_i, or consumed $-D_i$, at node i. Thus, for each node i in the network the following holds:

$$\sum_{j \in \Omega_i^N} f_{ij} = b_i = \begin{cases} G_i & i \in \mathcal{C} \\ -D_i & i \in \mathcal{D} \\ 0 & \text{otherwise} \end{cases} \tag{3.28}$$

However, with the inclusion of energy hubs, there is a need to consider flows between energy hubs and networks at each node i, and (3.28) becomes,

$$\sum_{j \in \Omega_i^N} f_{ij} + \sum_{l \in \mathcal{H}(i)} P_l - \sum_{m \in \mathcal{H}(i)} L_m = b_i \tag{3.29}$$

where $\mathcal{H}(i)$ is the set of hubs connected to node i, P_l is the energy source (i.e. input) of hub l, and L_m is the energy sink (i.e. output) of hub m. As before, b_i contains generator and demand variables and can be separated into injected generator flows $\mathbf{f}_G$ and consumed load flows $\mathbf{f}_D$. Thus, the flow balance equation in (2.99) can be generalized to that of an interconnected system of energy hubs,

$$A\mathbf{f} + H_I\mathbf{P} + H_O\mathbf{L} + G_A\mathbf{f}_G + D_A\mathbf{f}_D = \mathbf{0} \tag{3.30}$$

where $\mathbf{P}$ is the vector of all hub inputs, $\mathbf{L}$ is the vector of all hub outputs, $\mathbf{f}_G$ is the vector of all generator injections, $\mathbf{f}_D$ is the vector of all consumer energy demands, H_I is the hub input flow matrix, H_O is the hub output flow matrix, G_A is the generator-node matrix, and D_A is the load-node matrix. For example, if hub input P_l is connected to node i then $H_I(i, l) = 1$, and if generator f_{G_k} is at node i then $G_A(i, k) = -1$. Otherwise the entries are all zeros. The other two matrices are defined in a similar manner. Since no control over the network topology is assumed, the matrices are constant parameters. Thus, we can restate (3.30) in terms of function Λ_n for network n,

$$\Lambda_n(\mathbf{f}, \mathbf{f}_G, \mathbf{f}_D, \mathbf{P}, \mathbf{L}) = \mathbf{0}. \tag{3.31}$$

As shown in (3.31), the connection between energy hubs and power networks only exists at hub inputs and outputs. In addition, energy hubs provide the opportunity for coupling multiple energy networks. However, the energy type of each network is subject to specific physical constraints arising from the nature of the power flow. For example, the additional constraints imposed on an electrical power network can be expressed in the form of the linear DC flow model[1]:

$$f_{ij} = \frac{\theta_i - \theta_j}{x_{ij}}, \tag{3.32}$$

where x_{ij} is the reactance of arc (i, j) and θ_i is the voltage phase-angle at node i. As detailed in Section 2.3, the DC model approximates the nonlinear (and more representative) AC power flow. However, such energy flow constraints can also be highly nonlinear. A commonly cited nonlinear power flow constraint is exhibited in natural gas networks, where the power flow through pipelines depends in a nonlinear manner on the pressure p_i applied at the nodes [79],

$$f_{ij} = \begin{cases} k_{ij}\sqrt{p_i - p_j} & \text{if } p_i \geqslant p_j \\ -k_{ij}\sqrt{p_j - p_i} & \text{if } p_i < p_j \end{cases} \tag{3.33}$$

where k_{ij} is a constant pertaining to the specific gas and pipeline properties. In addition, power is necessary to maintain pressure at the nodes, which introduces the nonlinear compressor constraints,

$$f_{com,ij} = k_{com} f_{ij} (p_i - p_j) \tag{3.34}$$

with k_{com} a constant describing the properties of the compressor. In general, however, the physical constraints of any network n can be denoted by an equation of the form,

$$\mathbf{\Gamma}_n(\mathbf{f}, \xi_n, A_n) = 0 \tag{3.35}$$

where ξ_n are the state variables associated with the physical constraints, and A_n is the node-arc incidence matrix for network n. Note that $\mathbf{\Gamma}_n$ is independent of the energy hubs.

3.5   Multi-Period Optimal Dispatch Formulation

Combining the energy hub and network models discussed in the previous sections, one can form an appropriate optimization problem given an objective function. The optimization problem considers a prediction-horizon of N_T time-steps, $k = \{0, 2, \ldots, N_T - 1\}$. The objective function maps systems states and control variables to a scalar cost and the goal of optimization is to reduce the cost of operating the multi-energy system (i.e. provide energy to satisfy demands at lowest cost possi-

---

[1]There exists limitations of the approximate DC flow model, however, since the work herein is primarily within the context of energy exchanges between the multiple networks, this approximate model is sufficient.

ble). This is similar to the economic dispatch problem in electric power systems and, thus, the multi-energy optimization problem is denoted the **Multi-Period Optimal Dispatch Formulation** (MPODF).

Analyzing the optimal dispatch scenarios of power across interconnected energy hub systems allows determination of how to best employ energy hubs, energy hub storage, network generation, and energy resources. From (3.18) and the introduction of binary integer variables, energy storage devices require optimization over multiple periods with binary variables. In addition, the physical constraints in (3.35) are often nonlinear, which means that the MPODF, generally, represents a *multi-period nonlinear mixed-integer programming problem*:

$$\min_{\hat{\mathbf{P}},\mathbf{f}_G,\mathbf{Q}} \quad \sum_{t=1}^{N_T} \mathcal{F}\left(\mathbf{P}[k],\hat{\mathbf{P}}[k],\mathbf{L}[k],\mathbf{f}_G[k],\mathbf{f}_D[k]\right) \tag{3.36a}$$

subject to

$$\mathbf{P}[k] = \mathbf{S}_{in}\mathbf{Q}^{in}[k] + \mathbf{F}\hat{\mathbf{P}}[k] \qquad \forall k \quad (3.36\text{b})$$

$$\mathbf{L}[k] = \mathbf{C}\hat{\mathbf{P}}[k] + \mathbf{S}_{out}\mathbf{Q}^{out}[k] \qquad \forall k \quad (3.36\text{c})$$

$$\mathbf{Q}^{in}[k] = \mathbf{Q}_{\text{c}}^{in}[k] + \mathbf{Q}_{\text{d}}^{in}[k] \qquad \forall k \quad (3.36\text{d})$$

$$\mathbf{Q}^{out}[k] = \mathbf{Q}_{\text{c}}^{out}[k] + \mathbf{Q}_{\text{d}}^{out}[k] \qquad \forall k \quad (3.36\text{e})$$

$$\mathbf{E}^{in}[k+1] = \mathbf{E}^{in}[k] + \mathbf{N}_{\text{c}}^{in}\mathbf{Q}_{\text{c}}^{in}[k] + \mathbf{N}_{\text{d}}^{in}\mathbf{Q}_{\text{d}}^{in}[k] \qquad \forall k \quad (3.36\text{f})$$

$$\mathbf{E}^{out}[k+1] = \mathbf{E}^{out}[k] + \mathbf{N}_{\text{c}}^{out}\mathbf{Q}_{\text{c}}^{out}[k] + \mathbf{N}_{\text{d}}^{out}\mathbf{Q}_{\text{d}}^{out}[k] \qquad \forall k \quad (3.36\text{g})$$

$$\mathbf{\Lambda}_n\left(\mathbf{f}[k],\mathbf{f}_G[k],\mathbf{f}_D[k],\mathbf{P}[k],\mathbf{L}[k]\right) = \mathbf{0} \qquad \forall n, \forall k \quad (3.36\text{h})$$

$$\mathbf{\Gamma}_n\left(\mathbf{f}[k],\xi[k]_n,A_n\right) = \mathbf{0} \qquad \forall n, \forall k \quad (3.36\text{i})$$

$$\mathbf{0} \leqslant \hat{\mathbf{P}}[k] \leqslant \mathbf{F}^{\top}(\mathbf{P}[k] - \mathbf{S}_{in}\mathbf{Q}_{in}[k]) \qquad \forall k \quad (3.36\text{j})$$

$$\mathbf{0} \leqslant \mathbf{Q}_{\text{c}}^{in}[k] \leqslant \overline{\mathbf{Q}}^{in}\mathbf{z}^{in}[k] \qquad \forall k \quad (3.36\text{k})$$

$$-\underline{\mathbf{Q}}^{in}(\mathbf{1}-\mathbf{z}^{in}[k]) \leqslant \mathbf{Q}_{\text{d}}^{in}[k] \leqslant \mathbf{0} \qquad \forall k \quad (3.36\text{l})$$

$$\mathbf{0} \leqslant \mathbf{Q}_{\text{c}}^{out}[k] \leqslant \overline{\mathbf{Q}}^{out}\mathbf{z}^{out}[k] \qquad \forall k \quad (3.36\text{m})$$

$$-\underline{\mathbf{Q}}^{out}(\mathbf{1}-\mathbf{z}^{out}[k]) \leqslant \mathbf{Q}_{\text{d}}^{out}[k] \leqslant \mathbf{0} \qquad \forall k \quad (3.36\text{n})$$

$$\mathbf{0} \leqslant \mathbf{E}_{in}[k] \leqslant \mathbf{E}_{in}^{\max} \qquad \forall k \quad (3.36\text{o})$$

$$\mathbf{0} \leqslant \mathbf{E}_{out}[k] \leqslant \mathbf{E}_{out}^{\max} \qquad \forall k \quad (3.36\text{p})$$

$$\hat{\mathbf{P}}^{min} \leqslant \hat{\mathbf{P}}[k] \leqslant \hat{\mathbf{P}}^{max} \qquad \forall k \quad (3.36\text{q})$$

$$\mathbf{L}^{min} \leqslant \mathbf{L}[k] \leqslant \mathbf{L}^{max} \qquad \forall k \quad (3.36\text{r})$$

$$\mathbf{f}_G^{min} \leqslant \mathbf{f}_G[k] \leqslant \mathbf{f}_G^{max} \qquad \forall k \quad (3.36\text{s})$$

$$\mathbf{0} \leqslant |\mathbf{f}_G[k+1] - \mathbf{f}_G[k]| \leqslant \overline{\mathbf{R}}_G^{ramp} \qquad \forall k \quad (3.36\text{t})$$

$$\mathbf{f}_D^{min} \leqslant \mathbf{f}_D[k] \leqslant \mathbf{f}_D^{max} \qquad \forall k \quad (3.36\text{u})$$

$$\mathbf{f}^{min} \leqslant \mathbf{f}[k] \leqslant \mathbf{f}^{max} \qquad \forall k \quad (3.36\text{v})$$

$$z_i^{in}[k], z_j^{out}[k] \in \{0,1\} \qquad \forall i, \forall j, \forall k \quad (3.36\text{w})$$

where $k \in \{1, 2, \ldots, T\}$ and $n \in \mathcal{N}$ with $\mathcal{N}$ as the set of all energy carrier networks in the system. Of course, the dynamic SOC states $\mathbf{E}[k]$ must be initialized at $k = 0$.

The objective function $\mathcal{F}$ in (3.36a) may take a variety of forms for different studies. It will, therefore, depend on a range of variables, including energy hub inputs, outputs, and converter utilization, as well as network loads and generators. Equality constraints (3.36b)-(3.36g) describe the energy hub flow equations from Section 3.3, while inequality constraints (3.36j)-(3.36r) pertain to limits on dispatch flows, energy storage levels, charge/discharge flows, and hub input and output flows. The flow balance and physical constraints from Section 3.4 are described by equality constraints (3.36h) and (3.36i). Finally, the inequality constraints (3.36s)-(3.36v) arise from limits on network generators and loads, and flow capacities of network arcs. Additional constraints could be added depending on the scenario. For example, energy SOC levels may be required to satisfy a terminal constraints to enable energy conservation: $\mathbf{E}[0] \leqslant \mathbf{E}[N_T]$ over interval $[0, N_T]$.

Remark III.3. As has been discussed, there exists many ways to improve the tractability of mixed-integer non-linear MPODF. For example, the convexification of the SOC difference equations by omitting integers and linearizing power flows about salient operating points would enable a strictly linear MPODF problem since the energy hub model is linear.

3.6 Automated Analysis: Hubert

The energy hub network formulation presented in the previous section is employed to develop a concise ASCII-based format for describing a general energy hub network. Such a format allows one to take advantage of the inherent flexibility of the energy hub model and easily interfaces with Matlab and other optimization solvers to model, simulate, and analyze large multi-energy systems. The ASCII format together with analysis and simulation tools is what is referred to as "Hubert," in honor of the energy hub. Figure 3.4 gives an overview of Hubert: given a physical multi-energy system (modeled as an energy hub network), employ the ASCII format to succinctly describe the system and use Matlab to perform optimization, analysis, and simulation.

3.6.1 Header Information

Before establishing the energy hub and network formats, one must initialize the system with a system header that describes how many hubs and energy carrier networks the system employs. The header also allows users to specify the number of time-intervals they desire for the optimal dispatch problem.

3.6.2 Hub Format

To characterize a general energy hub, one only needs to be able to describe the four matrices: $\mathbf{S}_h^{in}$, $\mathbf{F}_h$, $\mathbf{C}_h$, and $\mathbf{S}_h^{out}$ from (3.15) and (3.17). Construction of these four matrices takes advantage of the simple building blocks nature of any energy hub
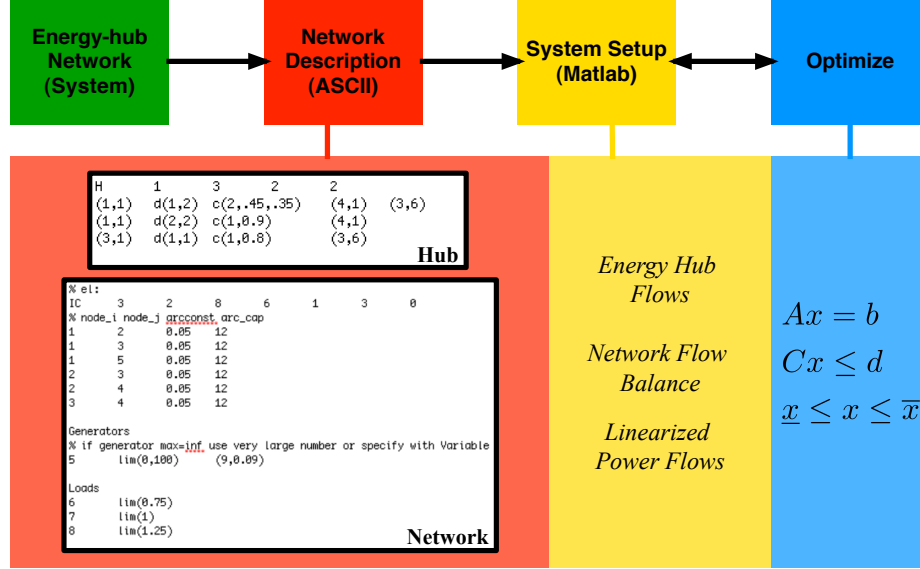
Figure 3.4: Overview of Hubert data flow.

and the knowledge that the flow of any hub input must enter input storage ($\mathbf{S}_h^{in}$), divide into dispatch flows ($\mathbf{F}_h$), enter converters ($\mathbf{C}_h$), and/or enter output storage ($\mathbf{S}_h^{out}$) before reaching a hub output. Therefore, by describing each hub's input flow to a converter, possibly through an input storage device and dispatch factors, and from converter to output, possibly through an output storage device, it is possible to construct the four matrices that characterize that specific energy hub. This hub description can be captured by the proposed ASCII-format description file.

An example energy hub is shown in Figure 3.5 with accompanying ASCII-format description in Listing III.1. The first line of Listing III.1 (starting with "H") identifies the hub ID number (1), the number of total hub dispatch factors (3), the number of hub inputs (2), and the number of hub outputs (2). Next, the format describes how the power flows through the hub. Input 1 (P_1) enters from node 3 in network 1, $(1, 3)$, and has two dispatch factors that each enter a separate converter. The first dispatch factor, df(1,2), enters converter C^F, which has one output with efficiency 0.6, c(1,0.6). The output flow from this converter leaves the hub at L_1 and is injected into node 1 of network 3, $(3, 1)$. Line 2 represents the second dispatch factor df(2,2) and is similar to line 1, except now we have two outputs from converter C^{CHP} into two different networks. The last line in Listing III.1 represents input P_2. This input utilizes input storage E_{in} with charge and discharge efficiencies 0.8 and 0.7, respectively, initial storage level 0 p.u., and maximum energy storage capacity of 6 p.u., s(0.8,0.7,0,6).

```
H 1 3 2 2
(1,3) df(1,2) c(1,0.6)   (3,1)
(1,3) df(2,2) c(2,0.3,0.35) (3,1) (2,1)
(2,5) s(0.8,0.7,0,6)   df(1,1) c(1,0.8)   (2,1)
```

Listing III.1: Description of the energy hub in Figure 3.5.

54
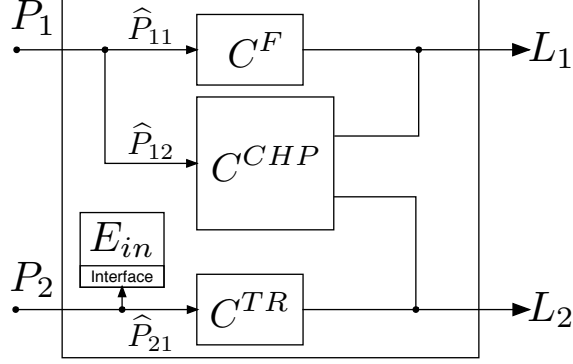
Figure 3.5: Example energy hub used to describe ASCII format.

With only one dispatch flow $\hat{P}_{21}$, described by `df(1,1)`, the flow enters converter C^{TR}, which has one output with efficiency 0.8, `c(1,0.8)`. Finally, the flow is injected into node 1 of network 2, $(2,1)$.

To indicate output storage, the storage string block `s(0.8,0.7,0,6)` is moved between the converter and output source. In the case of multiple output converters, as in Figure 3.1, additional output storage flags can be used to denote which outputs employ output storage devices.

3.6.3 Network Format

Fully describing the energy-carrier networks that interconnect energy hubs requires one to consider power balance and power flow constraints, (3.30) and (3.35), respectively. The matrices H_I and H_O from (3.30) can be constructed from the energy hub description of inputs and outputs in Section 3.6.2. Thus, for any network n, one needs only describe matrices A, G_A, and D_A from (3.30) and $\mathbf{\Gamma}_n$ from (3.35). To describe the first three matrices is relatively straightforward based on the network topology and location of all generators and loads. However, describing $\mathbf{\Gamma}_n$ is more difficult due to the potentially large variety of nonlinear physical networks and network parameters. For example, electricity, natural gas, and district heating are all different networks that require different physical constraints and parameters. Electrical networks (DC model) require reactance values, while natural gas networks require pipeline length and diameter, operating temperatures and pressures, and gas-specific values to describe flows between nodes. Nonetheless, by assigning *network types* to each network and making simplifying assumptions about the physics of each network, it is possible to define concise network-specific formats that allow representation of a simplified model of any network. For example, referring to (3.33), only a single parameter k_{ij} is required to describe the nonlinear flow of natural gas. As of this writing, the format in our libraries supports the following networks: electrical DC flow model, linearized natural gas flow model with linearized compressor stations, simplified district heating, and forecasted renewable (i.e. wind) power.

Figure 3.6 presents a simple (bidirectional) graph with four nodes and four edges, which models a small electrical power network. A DC power flow representation of
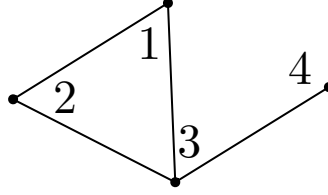
Figure 3.6: Example of a small electrical network (with nodal numbering).

the network is described by the network format in Listing III.2.

```
IC   1 2 4 4 1 1 0
1 2 0.05   10
1 3 0.05   10
2 3 0.05   10
3 4 0.05   10

Generators
1 lim(0,100)    (9,0.09)
Loads
3 lim(1)
```

Listing III.2: Format for describing the network in Figure 3.6.

The first line (starting with `IC`) describes the network ID (1), network type (2), number of nodes (4), number of arcs (4), number of generators (1), number of loads (1), and number of miscellaneous components (0). The network ID is used in the description of energy hubs' input and output sources, as discussed in Section 3.6.2. Network type specifies the expected model (and format) used to represent the physical power flow constraint parameters. The number of miscellaneous components provides a way to describe network-specific components, such as natural gas compressor stations. Since no such components are needed to describe the electrical network, its value is 0 in the example.

The next four lines are necessary to construct the node-arc-incidence matrix, and follow the same format for each arc. For example, Line 2 in Listing III.2 states that node 1 and node 2 in the network are connected with a parameter-value (reactance x_{ij}) of 0.05 p.u. and a flow capacity of 10 p.u.

From the description of each edge (i.e. transmission line) in the network, it is straightforward to determine node-arc incidence matrix A, however, to determine generator and load mapping matrices G_A and D_A it is necessary to explicitly list the generators and loads in the network. Thus, the format lists which nodes are generators (node 1) and loads (node 3). In addition, the format allows the user to specify per-unit limits on generation `lim(0,100)` and loads (fixed at 1 in example), as well as associated linear and quadratic generator costs curves for use in the objective function, `(9,0.09)`. Furthermore, the limits on generators and loads do not have to be numeric. In fact, an expression with variable generator or load limits is permitted by the format. For example, to denote a variable (e.g. forecasted) nominal load, replace `lim(1)` with `lim(0,Pd_el)`, where `Pd_el` $\in \mathbb{R}^{N_T}$ is a vector defined a-priori (e.g. in MATLAB) with an entry for each time-step of the optimization. The format

Network	$\langle k \rangle$	N	E	G	D
Electrical	4.36	100	218	12	22
Gas	4.88	100	244	8	8
Wind	0	20	0	20	0
Heat	0	30	0	0	30

Table 3.2: Topological characteristics of 102-hub energy network.

for other types of networks is similar, but may require different network-specific arc parameters.

3.7 Simulation

The format described in Section 3.6 allows for the construction of arbitrarily large interconnected energy hub networks and, together with MATLAB and a quadratic programming (QP) solver, seamlessly enables a solution to the optimal power dispatch problem formulated in (3.36).

3.7.1 System Construction

To explore the benefit and utility of the linear formulation and the proposed ASCII format, a large example energy hub system is constructed which consists of an electrical network, a natural gas network, district heat loads, and wind farms. Thus, the energy hubs couple the four different energy types. To construct the large energy hub system, the technique proposed in [80] for building random graphs that resemble electric grids is employed. The technique randomly places nodes on a $[0, 1] \times [0, 1]$ grid with uniform distribution. Then, based on a realistic average nodal degree and a maximum normalized arc length, nodes are connected based on an exponential arc-length distribution. Essentially, nodes that are close are more likely to be connected by an arc than nodes that are far away. The parameters used to construct the grids are in per unit (p.u.) and vary with uniform distribution within pre-specified ranges. Due to the size and random construction of the large electrical and natural gas networks and random interconnectivity of energy hubs, a meaningful visualization of the energy hub system is not straightforward and is, therefore, excluded here. However, via application of graph drawing software, such as GraphViz [81], meaningful visualization is a possibility for the future.

The topological characteristics of the large energy hub system are given in Table 3.2. The values N, E, G, and D represent the number of nodes, arcs, generators, and loads, respectively, while $\langle k \rangle$ is the average nodal degree. The wind and heat networks have no arcs and consist of generators and demands, respectively. A total of 102 energy hubs are employed to couple the four energy-carrier networks via randomly selected nodes. The energy hubs are used to connect from the electrical network to gas and heat networks, from the gas network to electrical and heat networks, and from the wind network to the electrical network. All other network couplings, i.e. from

gas to wind, are excluded in this simulation. The energy hubs connecting the wind network to the electrical network have output storage, while hub storage is added randomly to 75% of the remaining hubs. The system is assigned 24 time-intervals, corresponding to one complete day of operation. The consumer demand (load) and generation costs are variable and are set to peak near midday, while wind power is also variable and available mostly in the early and later parts of the day.

3.7.2   Simulation Results

The large hub system of Table 3.2 is represented using the ASCII format of Section 3.6, which allows for automatic construction of all the matrices necessary for solving the optimal dispatch problem in (3.36). The MPODF problem linearizes all power flow constraints and employs quadratic generator costs, resulting in a multi-period mixed-integer quadratic programming (MPMIQP) problem with 1942 (118 integer) variables per one-hour time-step. The MPMIQP problem was solved in 253 seconds within Matlab by interfacing with CPLEX 12.1 on a 2.8 GHz Intel Core 2 Duo MacBook Pro with 4 GB RAM. The results are shown in Figure 3.7.

The cost of wind power generation is assumed negligible (i.e. zero) and capital costs associated with installation and maintenance of storage are also not considered herein. In Figure 3.7a, the costs of electrical and natural gas generator injections are given in normalized monetary units (m.u.) and vary with time, peaking at hour 13. Consumer demand is also variable and peaks at that time, as depicted in Figure 3.7c-(b), raising the cost of supply. The objective function seeks to minimize the overall generator dispatch costs, which, as shown in Figure 3.7c-(a), begets an initial optimal response that causes a large amount of relatively cheap power to be injected into the system by the electrical and wind generators. This surplus injected power is utilized by energy hub storage devices as depicted in Figure 3.7c-(c) to maximize storage SOC levels *before* the generator costs and consumer demand reach their respective peaks near hour 13. After building up the energy storage SOC levels, the available wind power decreases during the middle of the day. Storage is utilized throughout the peak demand period to minimize generation during the most costly intervals. After time interval 18, the wind is strong enough to supply all electrical loads and most of the gas and heating loads.

The impact of storage on the cumulative energy cost over the 24-hour interval is shown Figure 3.7b. Building up the energy storage levels incurs a non-trivial initial cost. However, due to the time-varying price of generation, an overall savings of 5% is achieved when compared to the same system with no storage. In fact, as depicted in Figure 3.7b, the system with no storage becomes more expensive to operate at time-interval 13, which coincides with peak consumer demand. The ability to store low-cost energy and inject it during more expensive periods provides overall savings.

It is worth keeping in mind that these studies were performed on a non-trivial energy hub system that included 250 nodes in four different energy networks and 102 energy hubs.
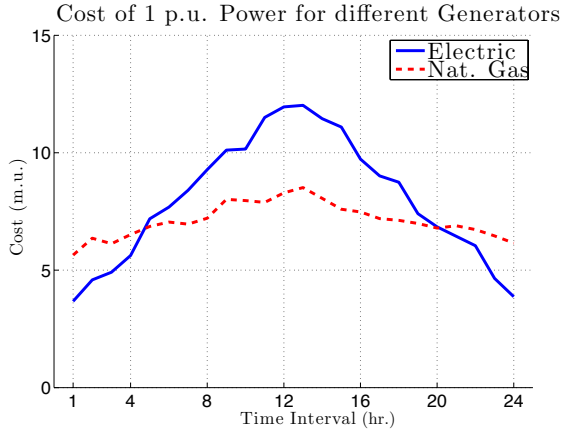
(a) Variable generator fuel costs.
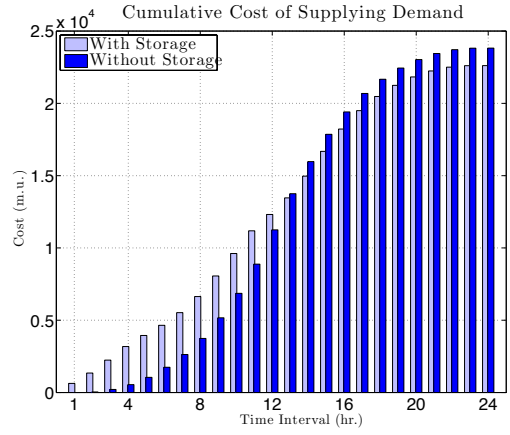
(b) Cost comparison for energy hub system with and without storage.
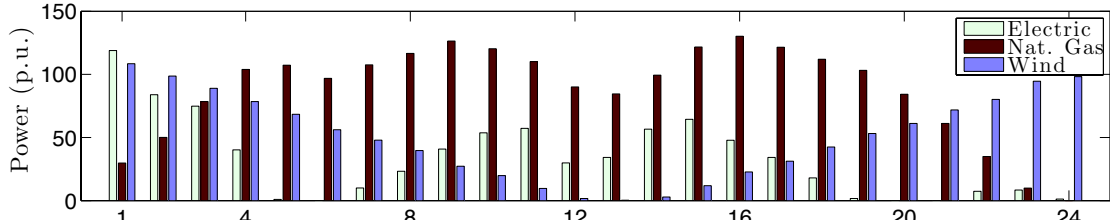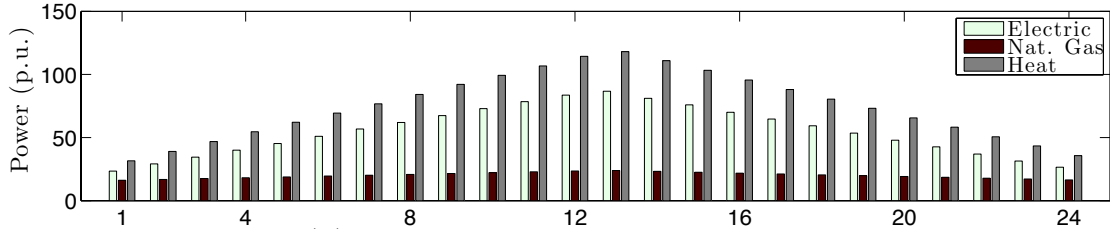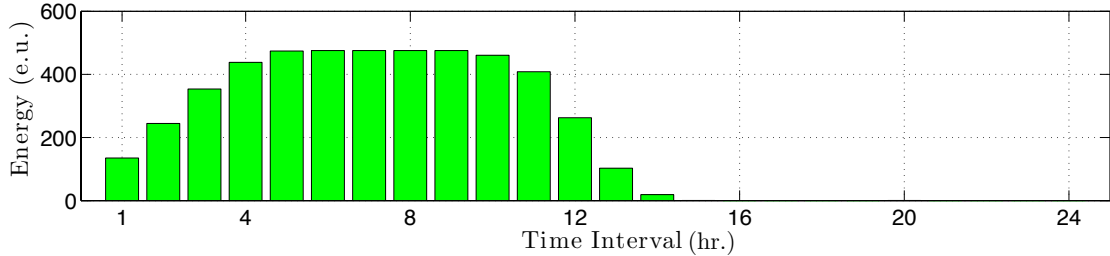
(c) Optimal power dispatch results.

Figure 3.7: Simulation results of 24-hour MPODF for a multi-energy system with 250 nodes and 102 energy-hubs.

3.8 Summary

This chapter motivates multi-energy systems and introduces the concept of the energy hub. A strictly linear model of the energy hub is developed that is amenable to a linear optimization formulation. Then, a concise ASCII-based text format is described to enable a straightforward and flexible framework for solving a general class of optimization problems that involve large-scale energy hub systems. The ideas are brought together with a numerical simulation of an energy hub system of more than 100 energy hubs.

In extending this work, it is of interest to include the study of large-scale cascading failures, which have been studied extensively in decoupled electrical networks. However, research on cascading failures in large multi-energy systems has generally not considered the concept of energy storage or energy hubs. Simulating cascading failures requires large networks and the tools developed in this chapter allows one to establish and manipulate large energy-hub systems in an efficient manner. Extending the results from this chapter, energy hubs within a cascade mitigation setting is explored in Chapter IV.

CHAPTER IV

Model-predictive Cascade Mitigation

4.1   Introduction

A significant extension of the work presented in Chapter III underlies this chapter. Employing the optimization framework and ASCII system format developed in Chapter III, arbitrarily large energy hub systems can be constructed and simulated. This allows for investigations of large-scale energy systems under severe disturbances (i.e. line outages), which comprises the core of this chapter. Specifically, two model-predictive control-based cascade mitigation approaches are analyzed herein. The first approach represents our initial work in the area, which evolves into second practical, yet rigorously justified, cascade mitigation scheme.

The chapter is organized as follows. First, basic relevant concepts are described, including line-tripping models. Then, a bi-level cascade mitigation scheme that considers economic and security objectives is discussed. Two cascade mitigation approaches utilizing model-predictive control (MPC) are detailed: shrinking horizon and receding horizon. The former employs the multi-energy formulation from Chapter III within a simplified shrinking-horizon MPC framework to highlight the role of energy storage and represents a first attempt of large-scale employment of energy hubs within a cascade mitigation framework. The second approach refines and improves upon the shrinking-horizon MPC scheme and focuses on receding-horizon MPC of electric power systems and a thorough analysis of the scheme is provided. The receding horizon MPC scheme is complemented with a case-study of an augmented version of the IEEE RTS-96 test network to highlight the practical, yet rigorously justified, cascade mitigation scheme.

The work presented in this chapter appears or is going to appear in the proceedings of the the 50th and 52nd IEEE Conference on Decision and Control and the 2012 Power & Energy Society General Meeting, and two manuscripts are in preparation to be submitted to the IEEE Transactions of Power Systems (see [82], [83], [84], [85], [86]).

4.2   Basic concepts and definitions

To ameliorate possible confusion with terminology, relevant definitions and concepts are described in this section.
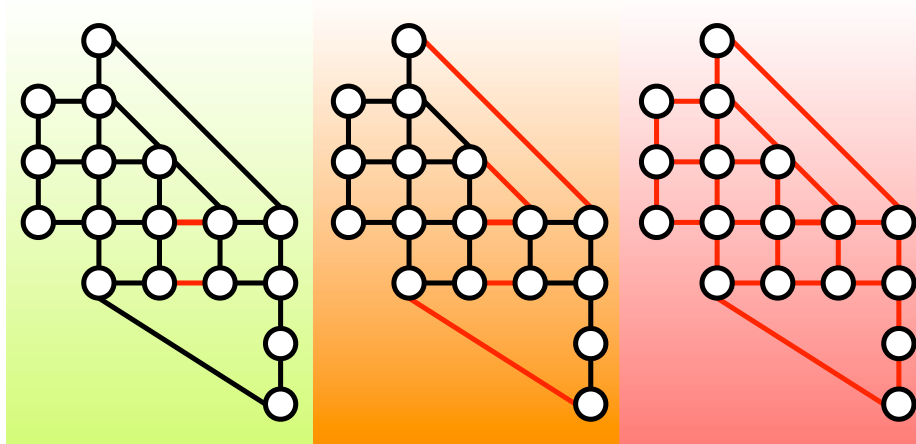
Figure 4.1: From left to right, illustration of the general process of a cascade failure in a network: initial disturbance, overloads and line tripping, and terminal blackout.

4.2.1 Cascade failures

From left to right, Figure 4.1 illustrates the three stages of a cascading failure: initial disturbance (left side of figure), cycles of line outages and flow redistributions (center), and a terminal blackout (right). Cascade failures are initiated when a disturbance occurs that forces a redistribution of flows. A line outage, generally, diminishes the network capacity, which causes additional lines to become overloaded and, if overloads are not alleviated, more lines may go out of service. If left uncontrolled, the cycle of line outages and redistribution of flows is referred to as a cascade failure. A cascade failure generally terminates in a major blackout, with large areas of a network unable to supply demand.

Furthermore, for electric power grids, a cascade is multi-scale in a somewhat unusual way. After the initial fault, the first stages of grid failure can proceed relatively slowly, on a scale of hours or minutes. If a cascade develops, the pace of failures can accelerate, with later waves happening on a scale of even seconds. This has important consequences for any control strategies. Since longer time scales allow for significant computations to be performed, corrective control strategies may extend the time between stages, can become an important method for mitigating a cascade.

Remark IV.1 (Braess Paradox)**.** The Braess Paradox [87] states that adding capacity to networks can, in some instance, actually increase congestion. Thus, an analogue in power systems would be that removing capacity (or lines) may not always lead to increased congestion, overloads, and a cascade failure, see [33] for such examples.

4.2.2 Line tripping

Definition IV.2 (Line Tripping)**.** When lines exceed their limits, it is possible that these lines trip. The term "tripping" refers to the event that causes a line to go from being in-service (i.e. ON) to out-of-service (i.e. OFF). When a line (i, j) is tripped (i.e. out of service) the following must hold:

- no flow (or losses) across (i, j): $f_{ij} = 0$.

- node i and j are decoupled in power flow equations. For example, for DC power flow, the constraint $x_{ij}f_{ij} = \theta_i - \theta_j$ does not have to hold.

In general, one of the main goals of a system operator is to ensure that line flows stay within predefined flow limits, which represents a form of network reliability. Therefore, if $f_{ij}(t)$ and u_{ij} are the (bidirectional) power flow and the power flow rating (i.e. limit) on arc (i, j) at time t, respectively, then, it is desirable to enforce the line flow limit:

$$|f_{ij}(t)| \leqslant u_{ij}, \tag{4.1}$$

where (i, j) represents arc between nodes i and j. Thus, if system operations satisfy (4.1) at all times t, arc (i, j) will not be tripped (under normal operating circumstances).

While it is feasible to take inequality (4.1) into consideration upon determination of an hourly economic energy management schedule, it is unrealistic to expect such a constraint to be valid after the system undergoes a significant disturbance (e.g. multi-line outage). This is due to the fact that flows depend on the physics of the network and cannot be directly guided (e.g. FACTS devices[1] are not considered here), which means that the line flows may exceed their limit after a contingency has occurred.

There exists a myriad of approaches to determine when an overloaded line should be tripped, ranging from deterministic hard constraints, as in [33], to soft-constrained probabilistic setups described in [34]. This section presents two models of line tripping: one is a simplified deterministic model and the other is probabilistic based on temperature overloads.

4.2.2.1 Deterministic outage model

The first model employs a simple deterministic outage criterion, which assumes that lines can withstand any power overload for M_T minutes before being tripped out of service. This model is obviously conservative, as it will trip lines regardless of the degree of the overload. For example, a 1% overload for 5 minutes is very different from 100% overload for 5 minutes, yet under this simple model both lines would trip. A justification for employing such a simple line outage model is that sensors may be installed that sample the line flow every M_T minutes and trips a line if an overload is sensed. Therefore, under proper control actions, lines should be brought within flow limits by time-step M_T (assuming synchronization of sensors and actuators). Such controller response aligns with a shrinking-horizon MPC controller which is described in Section 4.4.1.

---

[1]Flexible AC Transmission System (FACTS) devices employ power electronics to control AC system parameters, such as impedance, which enables some controllability of line flows.

4.2.2.2 Probabilistic Thermal Outage Model

The following probabilistic model is utilized in Section 4.5 to represent the actual line outage process for electrical transmission systems. For electrical systems, components, such as over-current relays, are often in place to protect the system against abnormal conditions by tripping lines (i.e. taking them out of service). However, these components operate for extreme over-current fault scenarios (e.g. $10,000+$ A) and trigger automatically on a timescale of seconds and mili-seconds and are, therefore, not considered in this work. Instead, the line-tripping behavior of interest in this dissertation occurs on a time-scale of minutes, which shifts the focus from fault-conditions to thermal conditions of transmission lines and sagging.

Electrical transmission lines have prescribed power flow limits to prevent dangerous sagging and permanent damage. These limits are related to the thermal capacity of the conductor and the current flowing across the line. Generally, there is an inverse relationship between the overload on a line and the time it takes before the line sags excessively and must be taken out of service; however, there are no clear rules when a sagging line will be taken out of service (by operator or nature). For example, a human system operator may decide that the red flashing warning sign is sufficiently annoying and trip the line manually or an elephant may just walk into a sufficiently sagging line and cause an outage[2]. Excessive line temperature (and resulting sag or possible annealing) may eventuate in line-tripping. In short: *the higher the temperature, the more likely line tripping becomes.* This inverse relationship between temperature and mean time-to-trip (i.e. mean time-to-failure) is captured in the actual system by use of the exponential time-to-failure density parametrized by the temperature overload:

$$P\left(\text{line } (i,j) \text{ trips at time } t\right) = \lambda(\Delta T_{ij})e^{-\lambda(\Delta T_{ij})\,t}, \tag{4.2}$$

where rate parameter $\lambda(\Delta T_{ij}) > 0$ is a non-linear function of the temperature overload, defined such that the mean time-to-failure goes to zeros as temperature increases (i.e. $\frac{1}{\lambda(\Delta T_{ij})} \to 0$ as $\Delta T_{ij} \to \infty$). That is, for each temperature overload, there is different mean time-to-failure. Thus, the probability of line (i,j) tripping during time-interval T_s, given ΔT_{ij}, is defined by the cumulative density function (also called the *unreliability function*):

$$P\left(\text{line } (i,j) \text{ trips during time-step } k \,|\, \Delta T_{ij}[k]\right) = \int_0^{T_s} \lambda(\Delta T_{ij})e^{-\lambda(\Delta T_{ij})\,\tau}d\tau \tag{4.3}$$

$$= 1 - e^{-\lambda(\Delta T_{ij}[k])\,T_s}, \tag{4.4}$$

where rate parameter $\lambda(\Delta T[k]) > 0$ is based on the short-time (15-minute) emergency (STE). That is, given an STE rating (e.g. $1.25 \times$ nominal rating), the method presented in Appendix 2.5.2 is deployed to compute an associated STE temperature, from which an appropriate $\lambda(\Delta T_{ij}[k])$ is chosen. It has been found experimentally that $\lambda(\Delta T_{ij}[k]) = (\Delta T_{ij}[k]/15)^6$ gives reasonable line tripping behavior, as shown in Figure 4.2. Notice how the mean time-to-trip decreases with increasing temperature

---

[2]This has actually happened more than 120 times in India since 2000 [88].
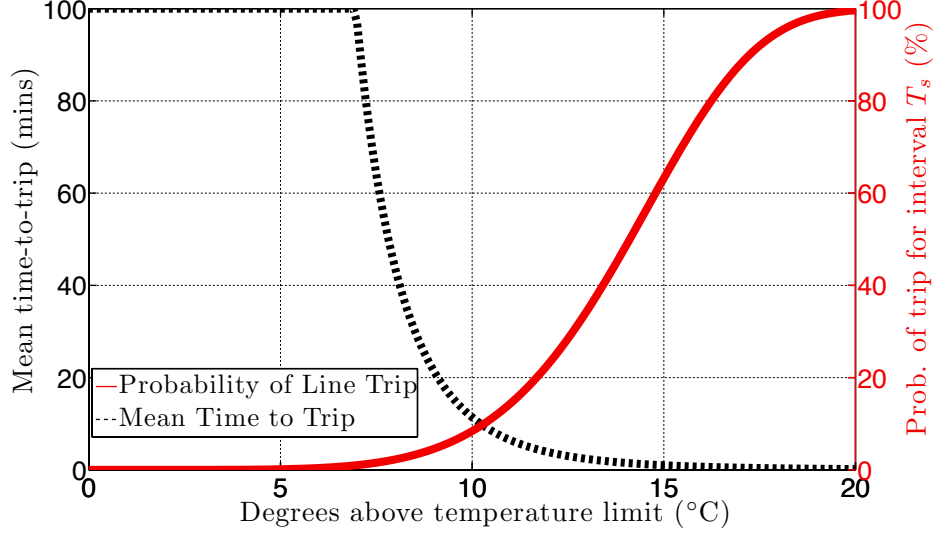
Figure 4.2: Probabilistic line outage model based on exponential time-to-trip distribution with $\lambda(\Delta T_{ij}[k]) = (\Delta T_{ij}[k]/15)^6$ from STE overload temperature rating. Tripping times beyond 100 minutes have been truncated for graphical purposes.

overload.

Furthermore, considering over-current protection on transmission lines (for large overloads), an additional condition can be added to the probabilistic line-tripping model:

$$P\left((i,j) \text{ trips at } k \,\middle|\, \frac{|f_{ij}[k]| + \frac{1}{2}f_{ij}^{\text{loss}}[k]}{u_{ij}} \geqslant \overline{\Omega}\right) = 1, \qquad (4.5)$$

where $\overline{\Omega}$ is an upper bound on allowable relative *instantaneous* overload. For example, if $\overline{\Omega} = 3$, then a line flow of 300% of nominal thermal limit u_{ij} automatically trips line (i,j).

With this formulation for line-tripping, if a line experiences an overload, the expected time to trip decreases as a function of the inverse of temperature-based rate-parameter $\lambda(\Delta T_{ij})$ and sampling time T_s.

4.2.2.3 Implementation of line-tripping

In this work, line tripping is not considered as a controllable decision made by the system operator. Therefore, line outages are implemented throughout this work by dynamically removing power flow constraints and variables associated with tripped lines from the optimization formulation. That is, it is assumed that network topology is observable at all times and that line-tripping events are known to the controller immediately after they occur. Relaxing these conditions represents avenues for future work.

Remark IV.3 (Extension to active line-switching). Note that *disjunctive line outage models*, such as the one proposed by [89], are employed widely in the area of line-

switching, where system operators are allowed to switch lines ON and OFF (e.g. to minimize losses). To consider the line-switching process within a linearly constrained optimization formulation is achieved by defining $s_{ij} \in \{0,1\}$ as the ON/OFF state of line (i,j), such that $s_{ij} \equiv 1$, implies that line (i,j) is ON; else, OFF. Thus, to model the ON/OFF switching of lines, one can modify line flow limit and power flow constraints (see (3.35)) as follows:

$$|f_{ij}[k]| \leqslant u_{ij}s_{ij}[k] \tag{4.6}$$

$$|\Gamma_n(f_{ij}[k], \xi_n[k], A_n)| \leqslant (1 - s_{ij}[k]) M_s. \tag{4.7}$$

where $M_s \gg 1$ is large enough to ensure that the physical parameters (ξ_{ij}) effectively become decoupled. For example, for an electric system modeled by DC power flow, if line (i,j) trips, then $s_{ij} \equiv 0$ and the following conditions are equivalent to a line that is OFF:

$$\left. \begin{array}{c} |f_{ij}[k]| \leqslant 0 \\ |\Gamma_n(f[k], \xi_n[k], A_n)| \leqslant M_s \end{array} \right\} \implies |x_{ij}f_{ij}[k] - \theta_{ij}[k]| = \begin{array}{c} |f_{ij}[k]| \leqslant 0 \\ |\theta_{ij}[k]| \leqslant M_s \end{array}. \tag{4.8}$$

Note that line flow is set to zero and voltage phase angles $\theta_{ij} := \theta_i - \theta_j$ are effectively decoupled by right-hand side inequality for a large M_s. When $s_{ij} \equiv 1$, the original constraints are recovered. Note that the extension of line tripping to line-switching is not pursued in this dissertation, but is straightforward. Of course, it should be cautioned that implementation of the disjunctive line outage model relies on integer variables (i.e. s_{ij}) and the "big-M" formulation, which does not scale well with network size and can encounter numerical difficulties. Finally, to be clear, the disjunctive models are not considered herein and this section only represents a possible extension.

4.2.3   Model-predictive control (MPC)

Literature provides two general approaches to mitigating cascade failures in power networks. The first method predicts disturbances *a priori* and is based on an off-line computation of all possible or likely failures in the network — the so-called $N - k$ problem, which was discussed in Chapter I. In such approach, control policies are devised to deal with each possible disturbance. A major drawback of this approach is that it does not scale well, since the number of salient contingencies to consider increases exponentially with network size. A second method is based on retroactive control, whereby the uncertainty surrounding the disturbance has been revealed and one can utilize the knowledge available about the disturbance to determine control responses in real-time to mitigate the effects of the disturbance. In the latter approach, the multi-timescale nature of cascading failures provides sufficient time for post-contingency computations and since power/energy systems are suffused with constraints on control inputs and states, it is, therefore, natural to consider model predictive control (MPC) schemes to alleviate the effects of cascading failures.

MPC has gained prominence over the last 30 years from its extensive deployment in the chemical industry for process/batch control. For a thorough technical discussion of predictive control in linear systems, please see [2]. Basically, MPC provides a

method for controlling dynamic systems with constraints on inputs and/or states using tools from optimization. MPC implementations solve on-line, at each sampling instant, a finite horizon optimal control problem based on a dynamic model of the plant. Most MPC approaches can be described by the following algorithm:

1. Determine a control profile that optimizes an objective function over a prediction window, where the current state at time-step k is the initial state.

2. Apply the computed control profile until new process measurements become available,

3. When new measurements are available, set $k = k + 1$ and repeat step (1).

MPC is most often formulated in the state space by linear discrete-time difference equations. The mathematical formulation is given below.

MPC Formulation The constraints are assumed linear (i.e. non-linear MPC is not discussed) and an l_2-norm represents the objective function, therefore, MPC can be formulated as a quadratic programming (QP) problem over a finite prediction horizon M:

$$U^*[k] = \min_{u[l|k]} \quad ||x[M|k]||_{S_M} + \sum_{l=0}^{M-1} L\left(x[l|k], u[l|k]\right) \tag{4.9a}$$

$$\text{s.t.} \quad x[l+1|k] = Ax[l|k] + Bu[l|k] \tag{4.9b}$$

$$x[0|k] = x[k] \tag{4.9c}$$

$$Cx[l|k] + Du[l|k] \leqslant d \tag{4.9d}$$

$$x[l|k] \in \mathcal{X}, \; u[l|k] \in \mathcal{U} \tag{4.9e}$$

$$x[M|k] \in \mathcal{T}_x \tag{4.9f}$$

for all $l < M$ where $x[l|k]$ and $u[l|k]$ represent the dynamic state and control input variables, respectively, at predicted time l given initial measured state at time k, $x[k]$ (i.e. $[l|k] \to$ time $k+l$). The objective function in (4.9a) is defined by:

$$L(x[k], u[k]) = ||x[k] - x_{\text{sp}}||_Q + ||u[k] - u_{\text{sp}}||_R \tag{4.10}$$

where $||y||_B = y^\top By$ and $S_M > 0$, $Q = Q^\top > 0$, $R = R^\top > 0$ are spositive-definite weighting matrices. The optimizer $U^*[k] = \{u^*[0|k], u^*[1|k], \ldots, u^*[M-1|k]\}$ represents the open-loop optimal control sequence over the prediction horizon at time k. Expressions (4.9b) and (4.9c) represent the linear discrete dynamics and initial (measured) state at time k, respectively. Expressions (4.9d), (4.9e), and (4.9f) define static inequality constraints, bounds on states and inputs, and a terminal state constraint set, respectively. Consider $\mathcal{X}$ closed, $\mathcal{U}$ compact, and $\mathcal{T}_x$ compact and containing the "origin." As will be discussed below, $\mathcal{T}_x$ represents a crucial "ingredient" which helps ensure stability of the MPC scheme.

4.2.3.1 Some important issues

Feasibility The computation of the optimal control profile $U^*[k]$ requires solving the QP optimization problem in (4.9). Therefore, it is necessary that the QP problem remains feasible under uncertainty and in the presence of noise and numerical errors. When feasibility is guaranteed for all future time, the QP problem is denoted *persistently feasible*. A common method to ensure persistent feasibility is by softening state constraints and keeping input-only constraints hard:

$$\begin{bmatrix} C_1 \\ \mathbf{0} \end{bmatrix} x[l|k] + \begin{bmatrix} D_1 \\ D_2 \end{bmatrix} u[l|k] \leqslant d + \begin{bmatrix} I \\ \mathbf{0} \end{bmatrix} \epsilon[l|k] \tag{4.11}$$

where $\epsilon[l|k] \geqslant 0$ are slack variables that are penalized relatively heavily in the objective function. The idea behind the heavy penalty on $\epsilon[l|k]$ is that the optimal solution should only employ $\epsilon[l|k] > 0$ to ensure feasibility, not to improve control performance. This implies that constraints on actuators, such as ramp/slew-rate and saturation constraints are enforced at all times to reflect hard constraints imposed by the physical system.

Stability The basic idea of stability of MPC relies on Lyapunov arguments, where stability is guaranteed if it can be shown that the total cost in the objective function is a Lyapunov function. That is, define

$$V(U, x[k]) := ||x[M|k]||_{S_M} + \sum_{l=0}^{M-1} L\left(x[l|k], u[l|k]\right) \tag{4.12}$$

with $S_M, Q, R > 0$ to be the objective function value corresponding to a feasible control profile $U[k]$, then the goal is to show that $V(U^*, x[k])$ is a Lyapunov function (i.e. $V(U^*, x[k+1]) \leqslant V(U^*, x[k])$ for all k, $V(\mathbf{0}, \mathbf{0}) = 0$, $V(U, x[k]) > 0$ for all $U \neq \mathbf{0}$).

As hinted to with terminal constraint in (4.9f), there exist basic "ingredients" (i.e. conditions) that enforce stability of MPC. Some popular and relevant techniques are reviewed here.

- *Terminal Equality Constraint.* A common condition for stability enforces that the terminal state of the prediction horizon is at the "origin" (defined by set point):

$$x[M|k] - x_{k+M}^{\text{sp}}[k] = 0. \tag{4.13}$$

  This implies that a feasible control profile at time-step $k + 1$ can be constructed from $U^*[k]$: $U[k+1] = \{u^*[1|k], u^*[2|k], \dots, u^*[M|k], 0\}$. Now, with the terminal constraint applied at $k+1$, it is straightforward to show that $V(U^*, x[k+1]) \leqslant V(U, x[k+1]) \leqslant V(U^*, x[k])$ is a Lyapunov function of the system, which ensures stability [90]. Employing a terminal

constraint reduces the set of admissible control laws, since initial conditions may prevent a large subset of feasible controls from being able to steer the state to the origin. Therefore, terminal constraints generally require longer horizons, which increases computational efforts.

- *Invariant Terminal Constraints.* A relaxation of the terminal equality constraint in (4.13) is the invariant terminal set constraint:

$$x[M|k] \in \mathcal{X}_f \tag{4.14}$$

where $\mathcal{X}_f$ is control invariant, which implies that if $x[k] \in \mathcal{X}_f \Rightarrow \exists u[k] \in \mathcal{U}$, s.t. $Ax[k] + Bu[k] \in \mathcal{X}_f$ for all k. Thus, when the state enters the invariant terminal set, there exists a local controller which can drive the system to the origin and stability follows from Lyapunov arguments. A common choice for the local (terminal) controller is the linear quadratic regulator. While less than in the case of (4.13), the terminal set constraint does shrink the set of admissible control profiles and may require large M-values.

- *Terminal Penalty.* To avoid adding stability-enforcing constraints, one can choose the terminal weighting matrix S_M to be the solution of the Algebraic Ricatti Inequality:

$$A^\top S_M + S_M^\top A + Q - S_M B R^{-1} B^\top S_M \geqslant 0. \tag{4.15}$$

Stability is then guaranteed from [91].

In this work, two specific MPC techniques are employed: shrinking horizon and receding horizon MPC. These two approaches are described in detail within the context of cascade mitigation in Sections 4.4 and 4.5, respectively.

4.3 Overview of Bilevel Cascade Mitigation Scheme

Economic dispatch problems (e.g. MPODF problem from Section 3.5) allow computation of economically optimal trajectories, which the system operator tracks via available generation, forecasted load, and other available control actions. However, if a significant disturbance takes place, the operator must modify his economical trajectory to prevent overloads and subsequent line outages. This requires the formulation of a contingency (safety) controller, which responds quickly to a disturbance and drives the system back to a secure and economical state, from which economic dispatch can be re-initiated and normal (economic) operation can resume. Since economic and security objectives are often competing objectives, it is natural to form two separate controllers for each task. Therefore, a bilevel hierarchical control strategy is employed. Figure 4.3 illustrates the proposed bilevel operation of the system.

The "Level 1" controller is enlisted to compute an economically optimal schedule for each hour of the day. When a disturbance takes place (e.g. line outage), Level 1 provides an economic reference for the "Level 2" contingency controller, which shifts
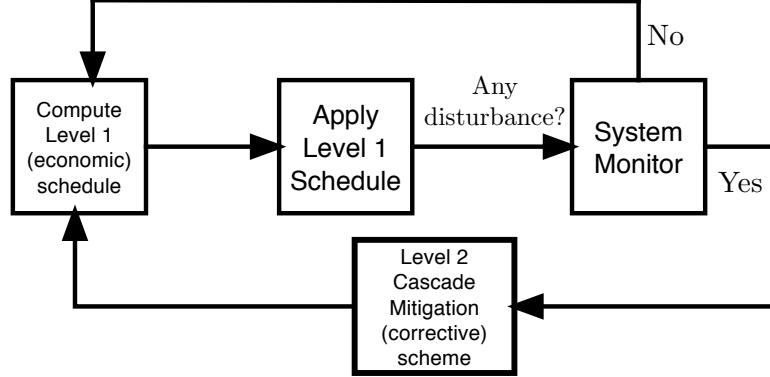
Figure 4.3: Overview of proposed bilevel cascade mitigation scheme.

operation from economically optimal (e.g. hourly) to corrective (e.g. minute-by-minute) in order to alleviate line overloads. When Level 2 signals that the system is secure, economic operation resumes with Level 1. The Level 2 controller is formulated as an MPC problem.

4.3.1 Level 1: economically optimal energy schedule

Over a 24-hour period, Level 1 computes an optimal energy schedule that determines how to best operate energy storage, conventional generation, flexible loads, and available renewable energy based on forecasts. The Level 1 schedule is, therefore, similar to standard economic dispatch [67], except that the temporal coupling introduced by energy storage implies optimization over a horizon rather than a single time-step. In addition, line losses can be included with a standard piece-wise linear (PWL) DC approximation as presented in [69] and described in Section 2.3.4.

The Level 1 model enforces line flow limits to ensure that, under accurate model and forecast scenarios, no lines are overloaded (i.e. the system is "safe" and economical). The dispatch schedule is computed as a multi-period quadratic programming (QP) problem whose objective is to minimize energy (fuel) costs of conventional generators:

$$\text{Cost}\left(\mathbf{f}_G[\,k\,]\right) = \mathbf{f}_G[k]^\top \alpha_G \mathbf{f}_G[k] + \beta_G^\top \mathbf{f}_G[k]. \tag{4.16}$$

where α_G [\$/h/pu^2] and β_G [\$/h/pu] are diagonal matrices of the generator-specific cost parameters and $\mathbf{f}_G$ [pu] is the power output levels provided by the generators. The only dynamics considered for Level 1 are energy storage dynamics and ramp-rate limits on generators. Thus, the Level 1 schedule represents a multi-hour reference signal with economically optimal system set points, x^{sp}, and required operator control actions to achieve optimal set points, u^{sp}. The schedule is submitted to the operator and recomputed every hour.

Remark IV.4 (Extension to Unit Commitment (UC)). UC algorithms, which generally involve integer programming over a 24-hour or 36-hour horizon to compute which generators to schedule for specific periods, could be included as a "Level 0" economic

computation and act as reference for Level 1. This would be a natural extension in line with current operating practice. The main challenges would be how to include energy storage devices and variable renewables within a meaningful and tractable unit commitment algorithm.

4.3.2 Level 2: corrective controller

The Level 2 controller operates in the background to track the reference trajectories computed from Level 1 (i.e. the economic set-point values). The corrective controller employs a linear model of the actual system and operates on a minute-by-minute timescale[3]. If a disturbance takes place (e.g. a line outage), Level 2 computes corrective control actions $u(t)$ in a MPC fashion that steers the system towards a safe and economically optimal state as provided by a Level 1 reference.

Level 2 considers ramp-rate limits on conventional generators, dynamics and power ratings of grid storage devices, and can incorporate the thermal response of overloaded lines. Note that, in Level 2, lines are no longer subject to a hard flow limit constraint and, instead, the controller seeks to drive lines below respective limits. The Level 2 MPC-based cascade mitigation scheme is formulated as a quadratic programming problem (QP) over a finite prediction horizon M.

Our initial work employed a shrinking-horizon (i.e. $M \to 0$) MPC-based scheme within a simplified framework of energy hubs and is detailed in Section 4.4. However, a more advanced MPC-based scheme is achieved with receding-horizon MPC (i.e. M fixed), which is applied within an electric power system setting and described in detail in Section 4.5.

4.4 Multi-energy cascade mitigation

This section investigates whether the presence of conversion and storage processes and technologies in a multi-energy system setting helps mitigate the effects of large network disturbances (i.e. line outages) and halts cascade failures.

Our initial work in the area of cascade mitigation proposes a low-level MPC-based controller that only is allowed to shed load in the final control instance. Once a disturbance is detected by the system monitor, operation of the system is switched from an hourly MPODF (economic) schedule defined by (3.36) to a fast timescale MPC scheme (one-minute time-steps). During the fast timescale, nominal load and intermittent power injections are fixed at their most recent slow timescale values, and generation and storage energy delivery rates are taken into account.

4.4.1 Shrinking horizon MPC (SHMPC)

In this MPC-based cascade mitigation scheme, if lines are overloaded after T_F minutes, they automatically trip (i.e. a sensor may measure overloads every T_F minutes and trip lines based on simple overload criteria). That is, a deterministic line-tripping

---

[3]The Level 2 time-step T_s is much shorter than the time-step used for the Level 1 reference signals. This is resolved by linearly interpolating between reference values.
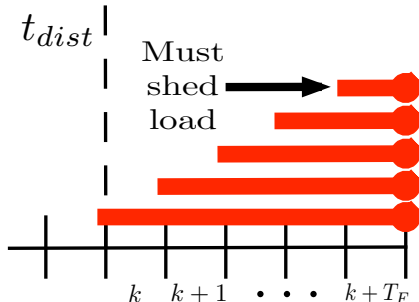
Figure 4.4: Overview of shrinking horizon MPC on fast timescale. The red bars represent the shrinking prediction horizons of each successive time-step.

model is employed in the multi-energy setting. Therefore, it is sensible to utilize a prediction horizon of T_F minutes and assume new measurements are available every minute (and that computation of open-loop control sequences is instantaneous). Furthermore, in attempting to halt the cascade, load-shedding is only allowed in the final time-step T_F, as a last resort to bring line flows within their limits. Accordingly, there is no reason for our prediction window to extend beyond minute T_F and, therefore, the prediction window shrinks by one minute after every measurement update. This method of MPC is often referred to as "fixed-point" or "shrinking-horizon" MPC (SHMPC) [92]. Stability arguments of SHMPC are straightforward as long as persistent feasibility is ensured. SHMPC considers a prediction horizon that is fixed in time as illustrated in Figure 4.4. Consider an energy system at time k over T_F minutes (i.e. initial prediction horizon) with sample time $T_s = 1$ minute. Then, SHMPC algorithm is given by:

Shrinking Horizon MPC Algorithm:

1. Given initial state $x[k]$, solving an optimal control problem over horizon $[k, k + T_F]$ yields the open-loop control sequence $\{u[l|k]\}_{l=0}^{T_F-1}$.

2. For time $[k, k + 1)$, apply first instance of control sequence $u[0|k]$ to the system with a zero-order hold.

3. Measure new system states $x[k + 1]$, set $k := k + 1$,

4. Set $T_F := T_F - 1$ and, if $T_F > 0$, repeat step (1). Else, STOP.

As can be realized from the above SHMPC process, with each successive control action, the horizon shrinks by one minute until horizon has length 0. At the end of the horizon some physical process may have reached a critical juncture, such as presented with the simple deterministic line tripping model: lines may trip.

If the MPC model has no errors and matches the real system, no overloads will remain, and the cascade will be halted. On the other hand, if the MPC model is imperfect, some overloads may remain. If more lines do trip, one would re-run SHMPC with redrawn horizon T_F and this shrinking-redrawing horizon cycle continues until SHMPC relieves all line overloads. At that point, the slow-timescale MPODF

72
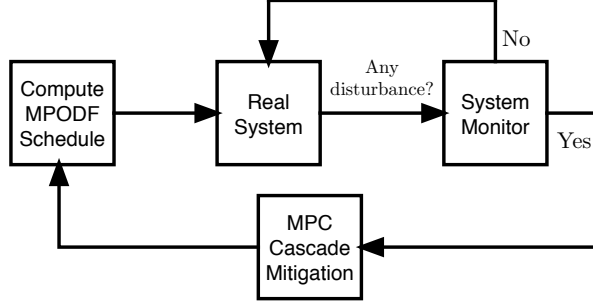
Figure 4.5: Operation overview of energy hub system under both normal MPODF operating conditions and contingency SHMPC operation.

is updated with a new post-disturbance network topology, and the latest values for generation, storage and load and the optimal schedule over the remainder of the 24-hour period are determined. An overview of the energy hub system operation under closed-loop control is illustrated in Figure 4.5. The MPODF schedule is equivalent to a Level 1, while the MPC Cascade Mitigation block represents Level 2. The cascade mitigation scheme interfaces with the "Real System" as well but on a faster time-scale. Note that without the look-ahead feature of MPC, a closed-loop controller acting only at minute T_F would shed more load, as it would not be able to properly allocate storage utilization to overcome possible future generator power limits.

To contrast the performance of the shrinking-horizon MPC scheme, we consider the base case of a "dumb" controller. The "dumb" controller seeks only to satisfy demand (i.e. avoid load-shedding) and line flows are given by the power flow solution with no regard for line flow limits. Therefore, the "dumb" controller will likely undergo cascading failures.

4.4.2 SHMPC model outline

The model presented in Chapter III is employed in the SHMPC scheme and, for convenience, is briefly outlined below. However, the constraints follow directly the MPODF problem posed in (3.36).

4.4.2.1 Constraints

- DC power flow model for each electric transmission line,

- linearized natural gas flow model for each pipeline (see Section 3.4),

- energy hub flow equations for each hub,

- energy storage SOC integrator dynamics,

- limits on network elements (e.g. storage, renewable and conventional generation, loads),

- ramp-rate limits on generators, and

- load shedding is only allowed at the end of the horizon (i.e. last control instance) which is the instance when line flow limits are enforced.

4.4.2.2 Objective function

The objective of the SHMPC is to alleviate line overloads by minute T_F and shed minimal load in the process. To minimize load shedding, rescheduling of energy storage utilization and generation is possible. Energy conversion and storage represents cheap control while generators are rescheduled based on their cost-curves (i.e. expensive generation is only used sparingly). A small penalty is placed on wind-spill while a large penalty is placed on load-shedding.

Remark IV.5. Since line flow limits are not enforced until the final time-instance, effectively, the load-shedding ability of the controller in the final control instance and the large penalty placed on load-shedding represents the means for enabling feasibility at all times. However, since load-shedding is a finite resource, official slack variables are included in the power balance equations. Thus, the SHMPC problem is persistently feasible.

4.4.2.3 Base case

For the base case, the arc flows are given by the power flow solution with no regard for flow limits. Thus, the base-case problem may undergo significant cascading failures and represents a controller with no information about the disturbance or line overloads. The goal of this "dumb" controller is, therefore, to just satisfy the load.

4.4.3 Simulations of SHMPC-based cascade mitigation

The formulation of energy hubs described in Chapter III permits the construction of arbitrarily large interconnected energy hub networks. In this section, the effects of disturbances (i.e. line outages) on small and large energy hub systems are investigated with simulations. Because current power grid operating and planning standards ensure power systems are in a reliable condition even if one contingency occurs [28], the initial disturbances will consist of multiple simultaneous outages. Each system consists of an electrical network, a natural gas network, district heat loads, wind turbines, and multiple energy hubs that couple the four different energy types. The smaller system is useful in describing how the SHMPC approach mitigates a cascade failure, while the large system allows us to better showcase the effects of cascade mitigation.

Remark IV.6. Note that these coupled hub systems are meant to represent future energy systems and, therefore, a lot of economical assumptions about the availability of storage and conversion processes are neglected in this work.

To construct both energy hub networks, the technique proposed in [80] is employed for building random grids. The technique assumes uniform node location, exponential expected link length distribution, and Poisson distribution for arc selection. The
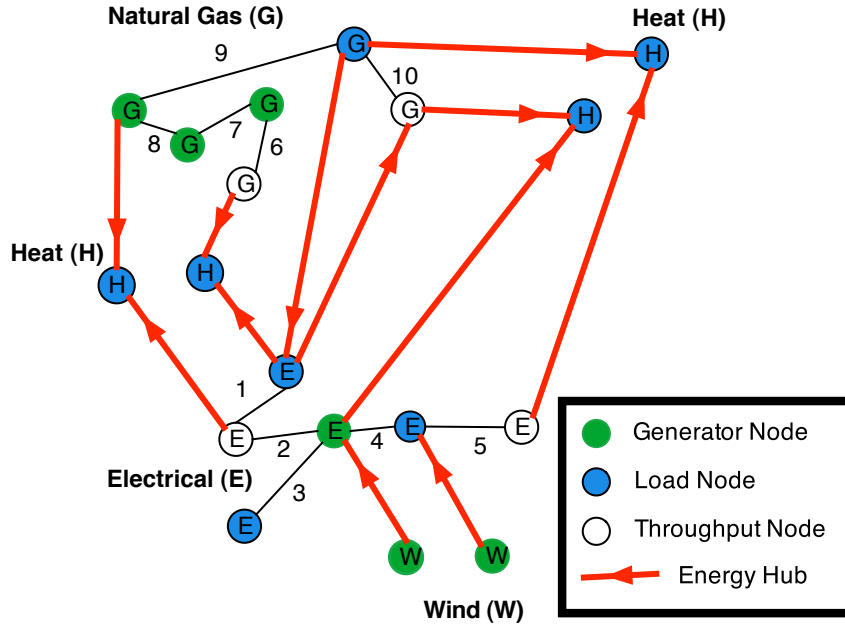
Figure 4.6: Network representation of small 12-hub system

parameters used to construct the power grids are in per unit (pu) and provided in Table 4.1. The small energy hub system is shown in Fig. 4.6. Due to the size of electrical and natural gas networks and the random interconnectivity with energy hubs, a meaningful visualization of the large energy hub system is not straightforward and is excluded. However, via application of graph drawing software, such as GraphViz [81], meaningful visualization is a possibility for the future.

The topological characteristics of our systems are given in Tables 4.2a and 4.2b. The values N, E, G, and D represent the number of nodes, arcs, generators, and loads, respectively, while $\langle k \rangle$ is the average nodal degree. Many well-known power systems exhibit average nodal degrees between 3.0 and 4.5. The wind and heat networks have no arcs and consist exclusively of generators and loads, respectively. A total of 12 energy hubs are utilized in the small system while the larger network has 132 energy hubs to couple the four different energy networks. The energy hubs are used to connect from the electrical network to gas (via electrolysis) and heat networks (via resistor heating), from the gas network to electrical (via gas turbines and fuel cells) and heat networks (via furnaces), and from the wind network to the electrical network (via turbines). All other network couplings, for example from gas to wind and from heat to electric, are excluded in this simulation. Table 4.2c shows the energy conversion efficiencies employed in the simulation. Note that the efficiency between wind energy and electric energy is set to 1.0, because only the injected power from the wind generators are considered and the lossy conversion between wind speed and generator is assumed to have already taken place. All hubs connecting the wind network to the electrical network have limited output storage, while hub (input or output) storage is added randomly to 75% of the remaining hubs.

75

Table 4.1: Parameters for construction of random grids

Parameters	Value/Bounds	Units
Electric Generators	[20,25]	p.u.
Gas Generators	[20,25]	p.u.
Wind Generators	[0, 6]	p.u.
Electric Loads	[0.5, 2]	p.u.
Gas Loads	[0.5, 2]	p.u.
Heating Loads	[1,2]	p.u.
Arc Flow Limits	[2, 4]	p.u.
Generator Ramping Limits	40	p.u./hr
Storage Ramping Limits	40	p.u./hr

Table 4.2: Network characteristics for multi-energy simulated systems

(a) The 12-hub energy network

Network	$\langle k \rangle$	N	E	G	D
Electrical	1.67	6	5	1	3
Gas	1.67	6	5	3	1
Wind	0	2	0	2	0
Heat	0	4	0	0	4

(b) The 132-hub energy network

Network	$\langle k \rangle$	N	E	G	D
Electrical	4.36	100	218	28	37
Gas	4.30	100	214	20	41
Wind	0	30	0	30	0
Heat	0	40	0	0	40

(c) Conversion efficiencies between energy types

From \ To	Electric	Gas	Wind	Heat
Electric	—	0.80	—	0.75
Gas	0.70	—	—	0.90
Wind	1.0	—	—	—
Heat	—	—	—	—

The system is assigned 24 one-hour time-intervals, corresponding to one complete day of operation. For the fast timescale, network arcs are allowed to be overloaded for no more than 5 minutes before being tripped automatically ($T_F = 5$). The consumer demand (load) is set to peak near midday, while wind power is available mostly in the early and later parts of the day. The cost of generation (electric and natural gas) is identical to the one depicted in Figure 3.7a and varies along with forecasted demand, so generation near midday is more expensive than the earlier or later parts of the day. Electric generation is set to be more expensive than natural gas.

The disturbance takes place at a random time between hours 1 and 24, unknown to the system controller, and consists of simultaneous outages of multiple lines. For the small energy hub system, the disturbance takes out 3 lines, while the larger network experiences a simultaneous outage of 5 lines. The 12-hub and 132-hub systems described by Table 4.2 are subjected to a disturbance and the SHMPC cascade mitigation scheme was simulated with Matlab and CPLEX.

- **Simulation results for small 12-hub system:**

  For the small system shown in Fig. 4.6, the disturbance takes place at time $t_{\text{dist}} = 7$ when three lines are taken out of service: lines 2, 5, and 8. Prior to the disturbance, the economically optimal dispatch schedule is computed off-line and is implemented as expected. Due to the cost of generation peaking during midday, cheap generation is employed to maximize storage utilization early in the day, as shown in Fig. 4.7 (b and c). Then after 7th hour, the disturbance causes the simultaneous outage of three lines. Within 5 minutes, the SHMPC approach reconfigures generation and energy storage (taking account of ramping limits) to satisfy nominal demand. However, in the fifth minute, as we seek to enforce the flow limits, the controller must shed around 20% of total load - mainly from the electrical load supplied by line 1 ($\sim 70\%$ shed), but the gas load supplied by line 9 ($\sim 25\%$) and the upper rightmost heating loads ($\sim 30\%$ each) are affected as well. Line 9 is crucial to the system, as it allows the controller to mitigate the effects of the disturbance through adjacent hub connections.

  Since the MPC halts further line outages, control returns to the slow timescale and a new economically optimal schedule is computed to minimize generator costs over the remainder of the 24-hour period with the three lines out of service. When wind power peaks towards the end of the day, despite having three lines out of service, the operator is able to restore loads through hub connections as shown in Fig. 4.7(a) and, therefore, reject the disturbance. Energy hubs play an important role in this problem, because the storage devices and hub-couplings of networks provide flexibility in the optimal scheduling of power flows to limit line overloading.

  For the base case, without the fast timescale MPC, it cannot reconfigure generation to enforce flow limits after the disturbance. Thus, in the fifth minute, the important line 9 is overloaded (as no load has been shed) and it trips from service. With the loss of line 9, the controller cannot supply the electric load supplied by line 1 and the gas load supplied by line 9 (both 100% shed). The
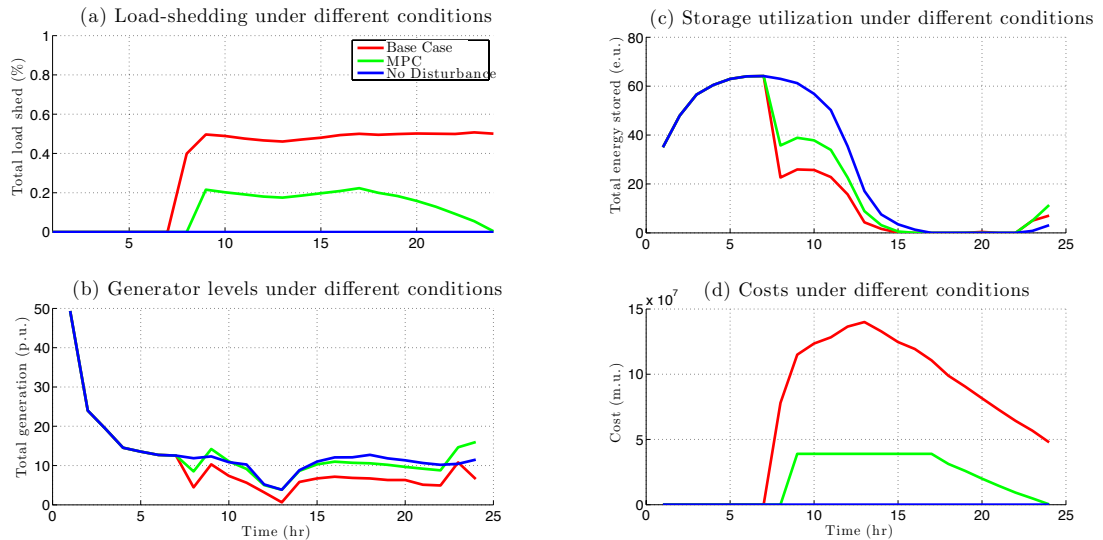
Figure 4.7: Simulation results from small 12-hub system

upper rightmost heating loads utilize stored energy at maximal rates to avoid having to shed loads. At hour 8, around 40% of load is shed in the system and at hour 9, when no stored energy remains to supply the upper-right heating loads, they are shed completely, resulting in $\sim 50\%$ of total load being shed. As seen in Fig. 4.7(a), the load is not restored in the remaining time.

The focus on cascade mitigation in the SHMPC context was to devise control policies that shed minimal load. Therefore, load-shedding was heavily penalized in the objective formulation. As a result, when load-shedding was necessitated during the "MPC" and "base-case" problems, the costs shown in Fig. 4.7(d) became less a measure of minimal generation costs and more a measure of how much load was shed during each case.

- **Simulation results for large 132-hub system:**

For the larger system, described in Table 4.2b, the disturbance also takes place at time $t_{\text{dist}} = 7$, when five lines are removed from service. Prior to the disturbance, the economically optimal schedule is employed to schedule generation and storage. As was the case with the small system, the low cost of generation during the early parts of the day leads to maximal storage utilization. After the 7th hour, the disturbance causes the simultaneous outage of 5 randomly chosen lines. Within $T_F = 5$ minutes, the SHMPC approach reconfigures generation and energy storage (taking into account ramping limits) to satisfy nominal demand across the new network. In the fifth minute, arc flows are returned to within their limits without having to shed any load. This is because a larger system with more nodes, arcs, and generators has greater flexibility in routing power flows to satisfy nominal demand.
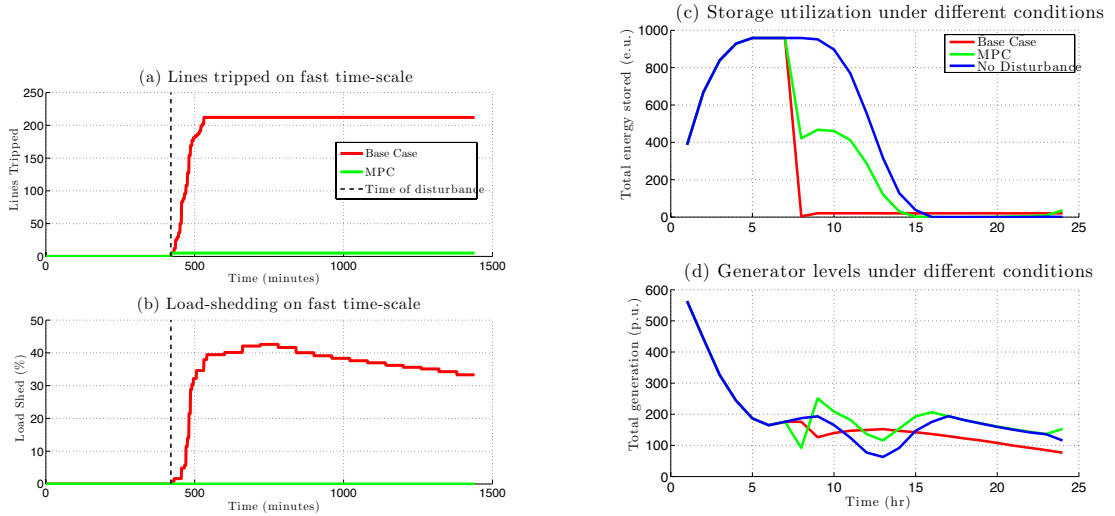
Figure 4.8: Simulation results from large 132-hub system

With a larger network, however, the complexity increases and it becomes more difficult to understand where weaknesses lie and how the system will respond to a disturbance. For the base-case problem, a cascading failure occurs as a consequence of the initial loss of five lines. For the next 115 minutes, the system utilizes all available hub storage to desperately avoid shedding load, as shown in Fig. 4.8(c). But as lines are tripped due to overloads, more and more load is shed. Fig. 4.8(a-b) provides a fast timescale view of the cascading effect of outages and load shedding. The cascade comes to an end when load-shedding has significantly lowered generation output levels, such that arc flows are within limits. In fact, the total load shed immediately after the cascade, when wind is low, is around 40%, Later in the day, when wind power has increased, some of the load is restored ($\sim 30\%$ shed).

Remark IV.7 (SHMPC disturbance rejection). The generator levels in Fig. 4.8(d) highlight that the model predictive controller essentially rejects the disturbance by returning to optimal pre-disturbance levels after time $t = 17$. At $t = 24$, the small difference between generation levels of the "MPC" and "No Disturbance" problems is due to excess available wind energy, which allows flexibility in the optimal solution. That is, in the final time-step, either excess (free) wind energy can be stored or wind generation curbed (i.e. spilled). Both solutions are optimal because stored energy has no future value in the final time-step. Thus, the MPC approach presented in this paper minimizes load shed and mitigates the effects of disturbances in general energy hub systems.

4.4.4 Impact of storage for cascade mitigation

During normal operation of the energy hub system, energy storage plays a significant role in minimizing generation costs from conventional generators, as it allows the system operator to pre-position energy in storage during off-peak hours (and pricing) to satisfy demand in the presence of intermittent generation (e.g. wind power). In the previous section, we employed a method to mitigate cascade failures in multi-energy systems by determining proper utilization of storage and generation. In fact, hub storage also plays a significant role in cascade mitigation since it acts as a "buffer" against disturbances. That is, a system operator can employ stored energy to satisfy temporary energy shortages or overflows, while allowing time for conventional generators to effectively reconfigure their schedules.

Thus, the effectiveness of system operations in minimizing costs and rejecting disturbances depends on the available energy hub storage infrastructure. Indeed, siting, sizing, and operational capability (e.g. power rating and standing losses) are salient parameters. Siting is important for reducing congestion during peak hours; however, the process for determining optimal location of energy hubs is non-trivial and is not considered here. Instead, this paper will fix the location of hubs within the system and study the effects of varying both hub storage capacity and charge/discharge power limits on the cascade mitigation process.

Under the energy hub paradigm, we are able to combine multiple types of energy systems and study their combined performance. Therefore, we need to consider multiple types of energy storage, namely, natural gas storage, electrical storage, and thermal storage. Note that, in this paper, we consider energy storage to have no standing losses, constant charging and discharging efficiencies (see Table 4.3), and we neglect the economics of construction, operation, and maintenance of storage facilities. That is, energy storage represents a cost-free service available to the system operator.

4.4.4.1 Natural Gas Energy Storage

The two main methods used in industry for storing natural gas are: "packed" pipelines and underground storage facilities. The packing of pipelines refers to the accumulation of natural gas in pipelines. Since such practices are commonly employed for pressure-regulation and only make up a small percentage of natural gas storage capacity, packing of pipelines is not considered in this paper. Instead, we consider underground storage in the form of reshaped salt caverns, which have high throughput and can be cycled hourly for both electric and heating loads, and aquifers, which can be regularly withdrawn and have large capacity [93]. The energy hubs that convert natural gas in the proposed multi-energy systems, therefore, contain input-side storage devices that reflect highly efficient underground storage facilities.

4.4.4.2 Electrical Energy Storage

With the intermittency of renewable energy (e.g. solar and wind), effective implementation of storage is highly desirable for improving system reliability. While

Table 4.3: Summary of different types of energy storage

Storage	Location	Charge Eff.	Discharge Eff.
Natural gas	Only input-side	99 %	99 %
Hydrogen	Both sides	80 %	65 %
Thermal	Only output-side	100 %	60 %

pumped hydro storage and compressed air systems provide two large-scale methods for storing electric-ready power, our focus is mainly on distributed storage in the form of hydrogen storage. Therefore, energy hubs that convert from electrical energy contain input-side hydrogen storage, while hubs that convert to electrical energy (e.g. wind) are outfitted with output-side hydrogen storage. Hydrogen storage requires an electrolytic process for charging (i.e. create hydrogen) and employs efficient fuel cells during discharging (i.e. consume hydrogen).

4.4.4.3 Thermal Energy Storage

Under the energy hub paradigm, both natural gas and electrical energy can be converted into thermal energy to satisfy district heating loads. This inherent energy flexibility improves system reliability and by employing thermal energy storage within the hub, we can satisfy distributed thermal loads from stored thermal energy, which reduces network congestion that tends to arise during peak demand. There exists a wide range of thermal energy storage solutions ranging from molten salt to gas-fired and electric storage heaters. However, for this paper, we will just consider a general form of thermal storage that supplies each heating load. The thermal storage device is employed on the output side of hubs which convert electrical and natural gas energy into heating. We assume a loss-less conversion of natural gas and electrical energy into thermal storage and attribute thermal energy losses to the discharging process.

Remark IV.8. Note that the efficiencies in Table 4.3 represent optimistic scenarios to give best-case performance of a multi-energy system with state-of-the-art storage.

4.4.4.4 Simulating energy storage scenarios

Employing the SHMPC cascade mitigation scheme, the following simulations investigate the performance of the scheme under different energy storage scenarios. That is, simulations are used to investigate how the availability (i.e. capacity) and performance (i.e. charge/discharge power limits) of energy storage devices impact the amount of load shed (i.e. performance of scheme).

The random grid-generating techniques proposed in [80] are employed again to construct two multi-energy systems - a small 11-hub system and a larger 69-hub system and subject each to a multi-line outage. The parameters used to construct the energy grids are also given by Table 4.1. The small energy hub system is shown in Figure 4.9 and is identical to the network of Figure 4.6, except that the hub

Table 4.4: Randomly generated network characteristics

(a) The 11-hub energy network

Network	$\langle k \rangle$	N	E	G	D
Electrical	1.67	6	5	1	3
Gas	1.67	6	5	3	1
Wind	0	2	0	2	0
Heat	0	4	0	0	4

(b) The 69-hub energy network

Network	$\langle k \rangle$	N	E	G	D
Electrical	3.07	60	92	20	15
Gas	3.00	60	90	12	21
Wind	0	18	0	18	0
Heat	0	22	0	0	22

(c) Conversion efficiencies between energy types

From \ To	Electric	Gas	Wind	Heat
Electric	—	—	—	0.75
Gas	0.70	—	—	0.90
Wind	1.00	—	—	—

converting electric to natural gas has been omitted as it represented a step too far into the future. Due to the size of electrical and natural gas networks and the random interconnectivity with energy hubs, a meaningful visualization of the larger energy hub system is not meaningful and is again excluded. The smaller, more simple system enables better understanding of how storage is utilized to mitigate cascade failure, whereas the larger system becomes useful in the discussion as it exhibits meaningful cascade behavior.

The topological characteristics of the two systems are given in Tables 4.4a and 4.4b. There are 11 energy hubs in the small system and 69 energy hubs in the large system to couple the four different energy networks. The energy conversion efficiencies are given in Table 4.4c. All hubs connecting the wind network to the electrical network have output storage, while applicable input and output hub storage is added randomly to all of the remaining hubs.

The energy storage scenarios are considered by varying storage capacity and storage power limits from the nominal values by a given factor. For example, for scenario (capacity, power) = $(0.25, 0.10)$, energy storage capacity is at 25% of nominal and power limits are 10% of nominal. The ideas is to compare the effect of different energy storage scenarios on the average load shed over the 24 hour period. In particular, the scenarios include systems with "no" (0), "some" (≈ 0.25), "nominal" (1.0), and "a lot" (10) of storage capacity, while the system storage devices are subject to "small" (0.10), "nominal" (1.0), and "large" ($5 \geqslant$) power limits.

- **Small 11-hub system:**

  In the nominal $(1, 1)$ case, the 11-hub system from Figure 4.9 undergoes a disturbance that results in the outage of lines 2, 5, and 8. The loss of the three lines leaves line 9 (natural gas) with a significant overload, which must be cleared to avoid tripping the line. Under the MPC scheme, generators are
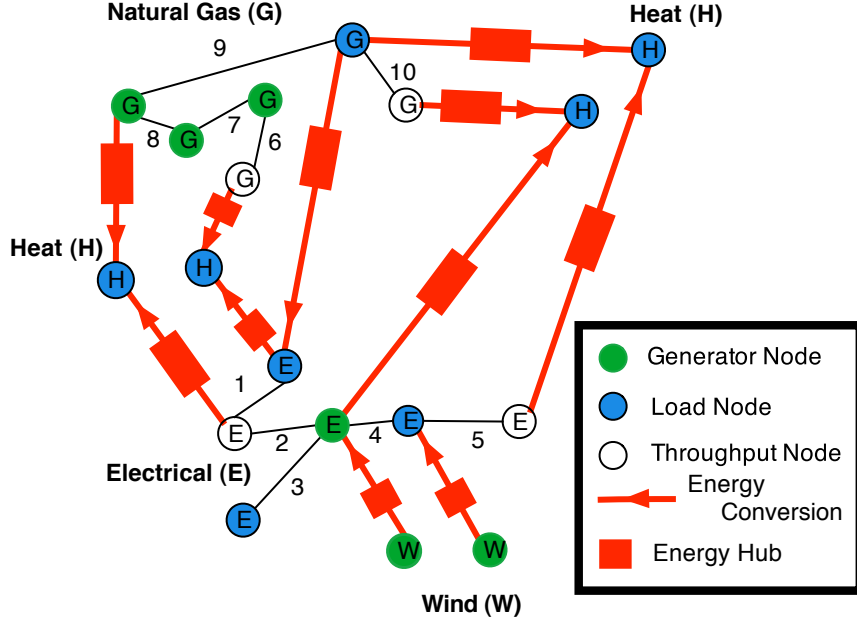
Figure 4.9: Network representation of small 11-hub system

Table 4.5: MPC energy scenario results for 11-hub system

Avg. load shed (%)		Capacity			
		0	**0.25**	**1.0**	**10**
	0.10	12.7	10.6	9.1	8.7
Power	**1.0**	12.7	10.8	9.0	9.2
	5.0	12.7	10.8	10.6	10.6

reconfigured (considering power limits), storage is utilized, and minimal load is shed over the 5-minute interval to avoid tripping line 9. The MPODF schedule is updated to reflect the multi-line outage and some load ($\approx$20%) must be shed until wind-power becomes available towards the end of the day. In the nominal base case, line 9 is not protected and trips after 5 minutes, which leaves the system in a weak state and results in heavy load-shedding ($\approx$50%).

The results of the 11-hub system are shown in Tables 4.5 and 4.6. Increasing storage capacity generally reduces the amount of load shed and improves performance of cascade mitigation, which is expected, since more energy can be stored and is available to inject into the system upon the disturbance. However, the general trend suggests that lowering power limits improves performance. The reason behind this trend is that the MPC scheme does not care about the state of the system beyond the halting of the cascade and will maximally utilize (free) stored energy to satisfy demand and avoid shedding load. However, with

Table 4.6: Base case energy scenario results for 11-hub system

Avg. load shed (%)		Capacity			
		0	**0.25**	**1.0**	**10**
	0.10	32.3	30.6	28.9	28.5
Power	**1.0**	32.3	32.3	30.1	29.8
	5.0	32.3	32.3	31.9	10.4

Table 4.7: MPC energy scenario results for 69-hub system

Avg. load shed (%)		Capacity			
		0	**0.20**	**1.0**	**10**
	0.10	1.1	0.9	0.5	0.4
Power	**1.0**	1.1	1.0	0.7	0.5
	10	1.1	1.0	0.7	0.7

small power limits, the amount of stored energy is effectively rationed during the cascade mitigation process and some conventional generation is needed to satisfy demand and halt the cascade. This balance between generation and energy utilization allows MPC to halt the cascade and best positions the multi-energy system to satisfy load demand over the subsequent period (following the cascade).

In the base case, the amount of load shed under scenario $(10, 5.0)$ is relatively low, because line 9 is "accidentally" not overloaded at minute 5. The term "accidentally" is used here since the base case controller attempts to satisfy all demand at the lowest cost with no regard for flow limits. Furthermore, for the $(10, 5.0)$ scenario, the base case sheds marginally less load than the MPC scheme over the 24-hour period. This is because the optimization does not penalize the spilling of wind power, which means that the MPC scheme can use available energy storage and wind power at the same cost. Thus, stored energy in the future (i.e. beyond the 5-minute prediction window) has no value to the MPC controller. MPC employs available energy storage and spills wind power, while the base case utilizes available wind-power. The MPC response is optimal over the 5-minute period, however with the cascade halted, it leaves the system with less energy stored. This results in a marginal increase in load-shedding over the remaining hours.

- **Large 69-hub system:**

The trends from the 11-hub system apply to the 69-hub system as well, and the results are provided in Tables 4.7 and 4.8. As storage capacity increases and power limits decrease, the performance of MPC increases for the same reasons

Table 4.8: Base case energy scenario results for 69-hub system

Avg. load shed (%)		Capacity			
		0	**0.20**	**1.0**	**10**
Power	**0.10**	23.8	24.7	23.7	19.9
	1.0	23.8	23.1	23.7	14.9
	10	23.8	23.1	24.8	29.4

mentioned above.

In the base case, the trend is not as strong, but nonetheless discernible. While the complexity of the network obfuscates the subtleties of the result, it is worth noting that for the scenario without storage (i.e. zero capacity), the amount of load shed is similar to low- and medium-capacity scenarios $(0.2, *)$ and $(1.0, *)$.

The behavior of both the base case system and the MPC cascade mitigation scheme are depicted in Figures 4.10 and 4.11, for energy scenarios (0, 10), (0.20, 10), (1.0, 10), and (10,10). (Note that thicker lines represent higher capacity scenarios). In fact, for scenarios $(*, 10)$, the base case system generally sheds more and more load as storage capacity increases. This is because the base case is uncontrollable in the sense that it does not regard line-flow limits and, for larger systems, this results in significant line tripping as seen in Figure 4.10a. At high power limits and with increasing storage capacity, the base case controller will inject more stored energy into the system (Figure 4.10c) which, coupled with non-trivial generation levels (Figure 4.11), results in line tripping (Figure 4.10a) and fragmentation of the system. The fragmentation leads renewables to become isolated from loads, which is evident in the base case in Figure 4.10b, since the increase in available wind power (in evening and at night) is unable to recover shed load. The fragmentation is most severe in the highest capacity case, where available wind-power is separated from loads and can only be utilized to aimlessly increase energy storage levels.

Note that "No Disturbance" cases represent economically optimal energy management without any line outages. However, in the absence of a disturbance, there is still a need to shed some nominal load when wind-power reaches its nadir and no more power can be injected by conventional generation without exceeding flow limits. This is a remnant of the fact that the random networks generated do not properly capture the design and planning of real transmission power networks.

Furthermore, it is worth noticing that the zero-capacity MPC scheme $(0, *)$ sheds only 1.1% of total load while the optimal MPC storage configuration $(10, 0.1)$ sheds 0.4% of total load. Therefore, one should ask if the investment made in storage devices is worth the marginally improved cascade mitigation performance (a 0.7% reduction in load shed). Indeed, with the base case minimal load shed of 14.9%, the MPC scheme *without* storage may provide a suffi-
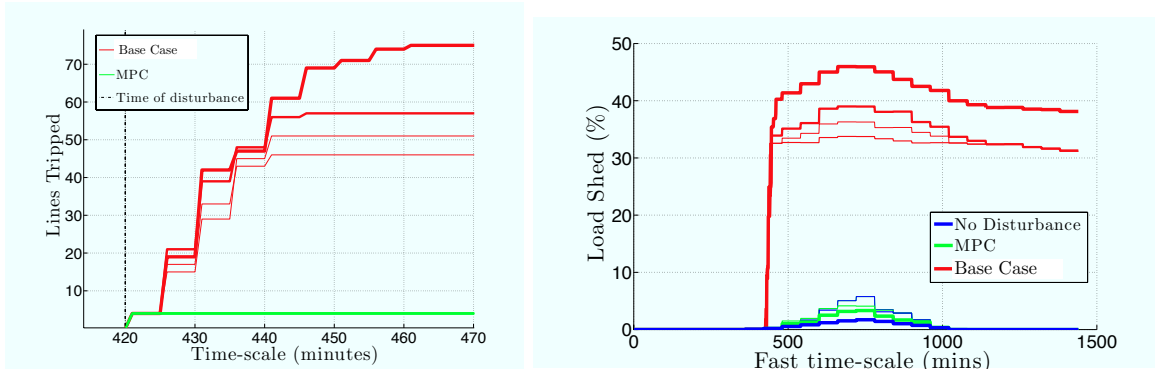
(a) Lines tripped on fast time-scale

(b) Load shedding on fast time-scale
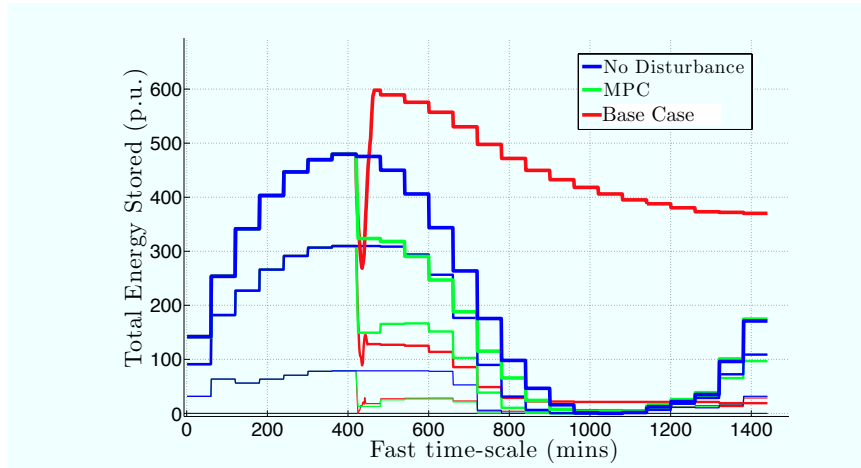
(c) Energy storage management on fast time-scale

Figure 4.10: Cascade simulation results from large 69-hub system with power limits at 10 times nominal. As storage capacity increases, the base case undergoes increasingly significant cascading. (Note: thicker lines $\Rightarrow$ higher capacity).

cient cascade mitigation solution. However, other factors, such as intermittency and congestion reduction, suggests the need for considering distributed storage devices in the investment process.
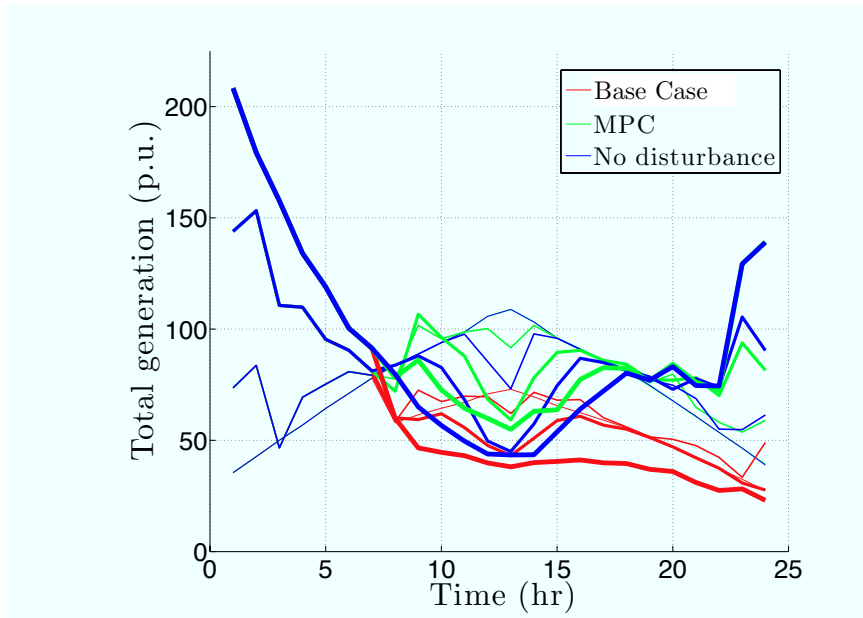
Figure 4.11: Generator levels for energy scenarios with ten times nominal power limits. As storage capacity increases, more off-peak power is utilized for storage, shaving off the midday peaks in generation. (Note: thicker lines $\Rightarrow$ higher capacity).

4.5 Cascade Mitigation in Electric Power Systems

The SHMPC-based first attempt at cascade mitigation was discussed in Section 4.4 and provided valuable insight into the role of energy storage for cascade mitigation purposes and the potential role of model-predictive control. However, the SHMPC formulation and the crude deterministic line overload model requires an improved approach. In addition, while the coupling of energy infrastructures may provide an opportunity to improve upon network resilience against cascade failure, investigations into the natural gas operations show that natural gas systems are significantly different from electric power systems. Namely, there is a time-scale separation between the two power systems, with electricity flowing at nearly the speed of light while natural gas pipelines experience gas flows of up to 60 miles per hour (around 100 km/hr). This relatively slow rate of power flow in natural gas systems gives rise to a different role for the transmission pipeline system. Specifically, natural gas transmission systems operate by filling, *in advance*, large underground natural gas storage facilities near power and heating load distribution centers. Under such circumstances, the idea of a cascade failure in natural gas systems is not as natural (no pun intended) as initially expected. As a result, the focus of this section is on cascade mitigation in electric power networks, which is more applicable.

4.5.1 Receding Horizon MPC (RHMPC)

The SHMPC scheme suffers from two major drawbacks:

- An unpredicted event could take place during the shrinking horizon period, which leaves the system unable to recover in the remaining time.

- As the horizon shrinks and approaches the final time, the control law typically "gives up trying" since there is too little time to go to achieve anything useful in terms of objective function reduction.

The above two shortcomings surrounding SHMPC can be overcome with the notion of *receding horizon* MPC. Receding horizon MPC (RHMPC) considers a prediction horizon that moves with time (i.e. moving or sliding window control) and is immune to the above drawbacks. Consider a system with prediction horizon of M_T minutes and sample time $T_s = 1$ minute and assume initial time-step is k, then RHMPC is summarized by the following algorithm.

Receding horizon MPC algorithm:

1. Given $x[k]$, solving an optimal control problem over horizon $[k, k + M_T]$ yields the open-loop control sequence $\{u[l|k]\}_{l=0}^{M_T-1}$.

2. Apply only the first instance of control sequence to system: $u[k] := u[0|k]$

3. Measure new system state $x[k+1] = f(x[k], u[k])$.

4. Set $k = k + 1$ and repeat step (1).

As the above RHMPC process illustrates, with each successive control action, the horizon no longer shrinks, but, in fact, recedes. A graphical illustration of RHMPC is given by Figure 4.12. Note that in this work, the prediction and control horizons are assumed equal: M_T.

4.5.2 RHMPC system model

The Level 2 RHMPC cascade mitigation scheme considers ramp-rate limits on conventional generators, dynamics and power ratings of grid storage devices, and incorporates the thermal response of overloaded lines. Note that in Level 2, lines are no longer subject to a hard flow-limit constraint. Rather, the controller seeks to drive conductor temperatures below their respective limits. The RHMPC optimization is formulated as a QP over a finite prediction horizon for all $l \in \mathcal{M} := \{0, \ldots, M-1\}$:

$$\min_{u[l|k]} \quad \left\|x[M|k] - x^{\text{sp}}_{k+M}\right\|_{S_M} + \sum_{l=0}^{M-1} L\left(x[l|k], u[l|k]\right) \tag{4.17a}$$

$$\text{s.t.} \quad x[l+1|k] = Ax[l|k] + Bu[l|k] + Fz[l|k] \tag{4.17b}$$

$$0 = \hat{A}x[l|k] + \hat{B}u[l|k] + \hat{F}z[l|k] \tag{4.17c}$$

$$Cx[l|k] + Du[l|k] + Gz[l|k] \leqslant d \tag{4.17d}$$

$$x[l|k] \in \mathcal{X}, \, u[l|k] \in \mathcal{U}, \, z[l|k] \in \mathcal{Z} \tag{4.17e}$$

$$x[M|k] \in \mathcal{T}_x \tag{4.17f}$$

$$x[0|k] = x^{\text{meas}}_k \tag{4.17g}$$
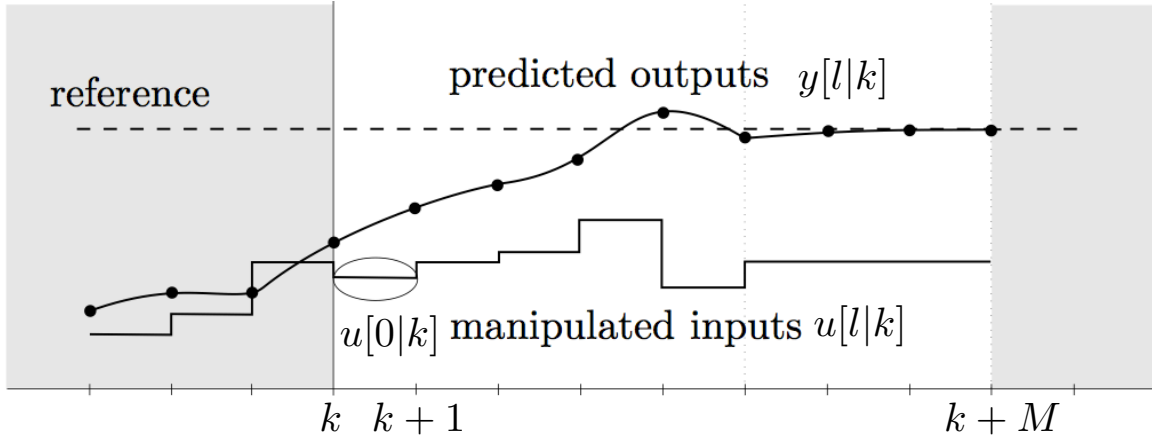
(a) RHMPC at time-step k
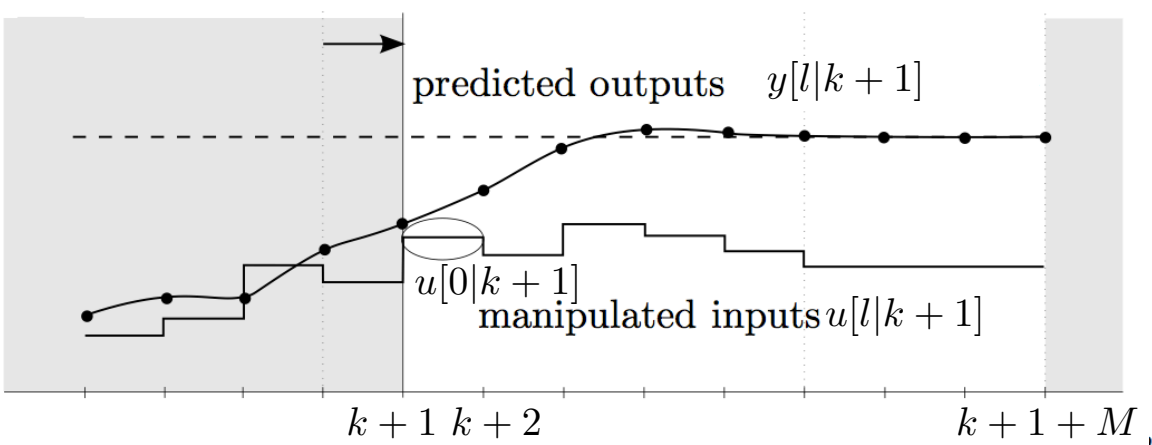
(b) RHMPC at time-step $k + 1$

Figure 4.12: Illustration of receding horizon MPC [2].

where $x[l|k]$, $u[l|k]$, and $z[l|k]$ represent[4] the dynamic state, control input, and algebraic state variables, respectively, at predicted time $0 \leqslant l < M$, given initial measured state x_k^{meas} at time k. The objective function in (4.17a) is defined by:

$$L(x[l|k], u[l|k]) = ||x[l|k] - x_{k+l}^{\text{sp}}||_Q + ||u[l|k] - u_{k+l}^{\text{sp}}||_R \tag{4.18}$$

where x_{k+l}^{sp} and u_{k+l}^{sp} refer to the Level 1 trajectory interpolated at time $k + l$, the norms are defined by $||y||_B \equiv y^\top B y$, and weighting matrices $S_M \geqslant 0$ and $Q \geqslant 0$ are non-negative definite while $R > 0$ is positive definite. Expressions (4.17b) and (4.17c) describe the differential-algebraic (DA) dynamics. Expressions (4.17d), (4.17e), and (4.17f) define static inequality constraints, bounds on states and inputs, and a terminal state constraint set, respectively. Equation (4.17g) establishes the initial state for RHMPC.

Remark IV.9 (Algebraic state constraints)**.** If the reader compares the general MPC description in (4.9) with the RHMPC model in (4.17), the main difference lies with the inclusion of algebraic state variables $z[l|k]$. Generally, algebraic equality constraints enable a formulation that adheres to the dynamic state and control input formulation portrayed in (4.9). This is because algebraic states are, generally, a function of the dynamic states and control inputs. That is, in the linear case, the matrix $\hat{F}$, generally, is invertible or has full rank and the following holds:

$$z[l|k] = -\hat{F}^{-1}(\hat{A}x[l|k] + \hat{B}u[l|k]). \tag{4.19}$$

However, with the convex relaxation of losses, the algebraic states associated with non-tight formulations beget a non-invertible $\hat{F}$ matrix. That is, for a line that is not tight, there is no unique transformation that maps the algebraic states of a line to the dynamics/controls. This affects the descriptions of equilibrium points of the system and turns stability into a quasi-like stability. For example, as the system is driven from an overloaded (non-economical/non-secure) state to an economical and secure state by RHMPC, the "equilibrium point" is actually a subspace of the algebraic state variables defined by the null-space of $\hat{F}$.

The details of the Level 2 RHMPC model, system states, and controls are mostly developed and discussed in Chapter II; however, a summary of the model is provided below. The states and inputs associated with the proposed formulation of a RHMPC cascade mitigation scheme for an electric power system are outlined below.

Dynamic states (x): there are three types of dynamic states:

- $\Delta \hat{T}_{ij}$, line (i, j) conductor temperature overload with respect to limit, T_{ij}^{lim}.

- E_n, state-of-charge (SOC) for ES n

- f_G, generator G's power output level.

Control inputs (u): the formulation employs six types of control inputs:

---

[4]The notation $[l|k]$ implies time $k + l$.

- Δf_G, change to conventional generator G output level

- $f_{G_W}^{\mathrm{spill}}$, wind spilled from nominal wind turbine G_W

- f_D^{shed}, load reduction from nominal demand D

- $Q_{\mathrm{c},n}$, $Q_{\mathrm{d},n}$, charge (c) and discharge (d) rate for ES n

- ψ^{PST}, phase-shifting transformer phase shift (rads)

Uncontrollable inputs: there are three types of forecasted inputs (i.e. exogenous disturbances):

- $f_{G_W}^{\mathrm{nom}}$, nominal available power from wind turbines G_W

- f_D^{nom}, nominal demand D

- d_{ij}, thermal effects for conductor (i,j) (e.g. solar input, ambient temperature).

Algebraic states (z): consider nine types of algebraic states:

- f_{ij}, real power flowing across line (i,j)

- f_{ij}^{loss}, real power loss from line (i,j)

- θ_{ij}, phase angle difference between nodes i and j

- $\theta_{ij}^{+}, \theta_{ij}^{-}$, absolute value approximation of $|\theta_{ij}|$

- $\{\theta_{ij}^{\mathrm{PW}}(s)\}_{s=1}^{S}$, S-segment PWL approximation of $|\theta_{ij}|^2$

- f_{G_W}, real power injected from wind turbine G_W

- f_D, real power consumed by load D

- Q_n^{T}, total power injected or consumed by ES n

References ($x^{\mathbf{sp}}, u^{\mathbf{sp}}$): there are five types of non-zero economical reference states and inputs (i.e. from Level 1):

- E_n^{ref}, state-of-charge (SOC) reference for ES n

- f_G^{ref}, generator G's reference power output level.

- $\Delta f_G^{\mathrm{ref}}$, reference change to conventional generator G output level

- Q_n^{ref}, charge / discharge reference rate for ES n

- $\psi^{\mathrm{PST},\mathrm{ref}}$, phase-shifting transformer phase shift reference (rads)

For each time k, the dynamic states x_k^{meas} are measured and represent the initial state of the system. Since the system is time-invariant, for ease of notation, the term $[l|k]$ is replaced by $[l]$. Then, the full RHMPC formulation is defined as a quadratic programming (QP) problem:

$$\min_{u[l]} \quad \left\| x[M] - x_{k+M}^{\text{sp}} \right\|_{S_M} + \sum_{l=0}^{M-1} L\left(x[l], u[l]\right) \tag{4.20a}$$

$$\text{s.t} \quad \Delta T_{ij}[l+1] = \tau_{ij}\Delta T_{ij}[l] + \rho_{ij}\Delta f_{ij}^{\text{loss}}[l] + \hat{\rho}_{ij}^{\top}\Delta d[l] \tag{4.20b}$$

$$E_n[l+1] = E_n[l] + \eta_{\text{c},n}Q_{\text{c},n}[l] + \frac{Q_{\text{d},n}[l]}{\eta_{\text{d},n}} \tag{4.20c}$$

$$f_{\text{G}}[l+1] = f_{\text{G}}[l] + \Delta f_{\text{G}}[l] \tag{4.20d}$$

$$\Delta \hat{T}_{ij}[l] = \max\{\Delta T_{ij}[l], 0\} \tag{4.20e}$$

$$0 = \Gamma_i\left(f_{ij}[l], f_{ij,k}^{\text{loss,est}}, f_G[l], f_D[l], Q_n^{\text{T}}[l]\right) \tag{4.20f}$$

$$0 = a_{ij}x_{ij}f_{ij}[l] - \left(\theta_{ij}[l] - \psi_{ij}^{\text{PST}}[l]\right) \tag{4.20g}$$

$$0 = a_{ij}x_{ij}^2 f_{ij}^{\text{loss}}[l] - r_{ij}\Delta\theta\sum_{s=1}^{S}(2s-1)\theta_{ij}^{\text{PW}}(s)[l] \tag{4.20h}$$

$$0 = \theta_{ij}^{+}[l] + \theta_{ij}^{-}[l] - \sum_{s=1}^{S}\theta_{ij}^{\text{PW}}(s)[l] \tag{4.20i}$$

$$0 = \theta_{ij}^{+}[l] - \theta_{ij}^{-}[l] - \left(\theta_{ij}[l] - \psi_{ij}^{\text{PST}}[l]\right) \tag{4.20j}$$

$$f_D[l] = f_{D,k+l}^{\text{nom}}[l] - f_D^{\text{shed}}[l] \tag{4.20k}$$

$$f_{GW}[l] = f_{GW,k+l}^{\text{nom}}[l] - f_{GW}^{\text{spill}}[l] \tag{4.20l}$$

$$Q_n^{\text{T}}[l] = Q_{\text{c},n}[l] + Q_{\text{d},n}[l] \tag{4.20m}$$

$$x[l] \in \mathcal{X}, \ u[l] \in \mathcal{U}, z[l] \in \mathcal{Z} \tag{4.20n}$$

$$x[M] \in \mathcal{T}_x \tag{4.20o}$$

$$x[0] = x_k^{\text{meas}} \tag{4.20p}$$

for all $l \in \mathcal{M}$. The objective function in (4.20a) is defined by (4.18) and measures deviation from reference values over the prediction horizon. Expressions (4.20b), (4.20c), and (4.20d) represent the linear (discrete) dynamics associated with conductor temperature for line (i,j), SOC for energy storage device n, and the output level of generator G, respectively. The thermal conductor model is based on IEEE Standard 738 describing the temperature-current relationship in overhead conductors. Temperature dynamics in (4.20b) are linearized with respect to the conductor temperature

(T_{ij}^{lim}) at ampacity (I_{ij}^{lim}), and conservative ambient parameters $(q_s^*, T_{\text{amb}}^*)$. That is,

$$\Delta T_{ij}[l] = T_{ij}[l] - T_{ij}^{\text{lim}} \tag{4.21}$$

$$\Delta f_{ij}^{\text{loss}}[l] = f_{ij}^{\text{loss}}[l] S_b / 3L_{ij} - R_{ij}(I_{ij}^{\text{lim}})^2, \tag{4.22}$$

$$\Delta d[l] = \begin{bmatrix} q_s[l] \\ T_{\text{amb}}[l] \end{bmatrix} - \begin{bmatrix} q_s^* \\ T_{\text{amb}}^* \end{bmatrix} \tag{4.23}$$

where S_b [VA/pu] and L_{ij} [m] are power base and conductor length, respectively, and R_{ij} [Ω/m] is the per-unit length resistance. Recall from Section 2.5 that the resistance of a conductor varies linearly with temperature (up to ±20%) and, thus, given previously measured temperatures, one can obtain a good estimate of R_{ij} over the prediction horizon.

Constraint (4.20e) defines the main objective of alleviating temperature overloads while not incentivizing underloading of lines. That is, the RHMPC should compute control actions that only consider lines with $\Delta T_{ij}[l] > 0$. Keeping in mind the QP linear constraint formulation, the temperature objective is given by $\Delta \hat{T}_{ij} = \max\{0, \Delta T_{ij}\}$. This constraint can be relaxed to the linear formulation,

$$0 \leqslant \Delta \hat{T}_{ij} \tag{4.24a}$$

$$\Delta T_{ij} \leqslant \Delta \hat{T}_{ij}. \tag{4.24b}$$

Because the objective function penalizes $\Delta \hat{T}_{ij}$, this relaxation will always be tight.

Equations (4.20f) and (4.20g) denote nodal power balance constraints ($\forall i \in \mathcal{N}$) and DC power flows, respectively. Power balance implies Kirchhoff's 2nd law: that power flowing into node i must equal the power flowing out of the node i plus/minus what is injected/consumed at node i. Note that DC flow as presented in (4.20g), reflect application of the "Unified Branch Model" [66] that is described in detail in Chapter 2.3. Under the unified model, in-phase (IPT, $\psi_{ij} = 0$) and phase-shifting (PST, $a_{ij} = 1$) transformers and transmission branches ($a_{ij} = 1$, $\psi_{ij} = 0$) can be described with the same system of equations.

The convex PWL approximation of line losses, developed in Section 2.3.4, is described by the algebraic relations (4.20h), (4.20i), and (4.20j). The piecewise linear relaxation utilizes S segments of width $\Delta \theta = \bar{\theta}/S$ and is modeled with the algebraic states $\theta_{ij}^+, \theta_{ij}^-, \{\theta_{ij}^{\text{PW}}(s)\}_{s=1}^{S}$. Note that the unified flow model is also applicable for line losses.

Algebraic equations (4.20k), (4.20m), (4.20l) define the relationship between control inputs and power balance from (4.20f). Specifically, how load shedding, injections/consumption by storage, and wind curtailment are coupled with generation and line flows within the electric network.

The sets defined in (4.20n) and (4.20o) are convex polytypes. In particular, $\mathcal{X}$ is closed and $\mathcal{U}$ is compact and the sets contain the Level 1 reference trajectories $x_l^{\text{sp}}, u_l^{\text{sp}}$

for all $l \in \mathcal{M}$:

$$x_l^{sp} \in \mathcal{X} = \left\{ x \,\middle|\, E[l] \in [0, \overline{E}]; f_G[l] \in [\underline{f_G}, \overline{f_G}] \right\} \tag{4.25a}$$

$$\mathcal{Z} = \left\{ z \,\middle|\, \theta_{ij}[l] \in [-\overline{\theta}, \overline{\theta}] \subset (-\pi/2, \pi/2); \right. \tag{4.25b}$$

$$\left. \theta_{ij}^+[l], \theta_{ij}^-[l] \geqslant 0; \ \theta_{ij}^{\mathrm{PW}}(s)[l] \in [0, \Delta\theta] \right\}$$

$$u_l^{sp} \in \mathcal{U} = \left\{ u \,\middle|\, f_D^{\mathrm{shed}}[l] \in [0, \alpha_D], f_{\mathrm{Gw}}^{\mathrm{spill}}[l] \in [0, \alpha_G], \right. \tag{4.25c}$$

$$\Delta f_G[l] \in [-R_G^{\mathrm{down}}, R_G^{\mathrm{up}}], \psi_{ij}^{\mathrm{PST}}[l] \in [-\alpha_P, \alpha_P],$$

$$\left. Q_{c,n}[l] \in [0, \overline{Q}_c], Q_{d,n}[l] \in [-\overline{Q}_d, 0] \right\}$$

with bounds defined by appropriate parameters.

Finally, the set $\mathcal{T}_x$ represents the convex polytopic terminal constraint set, meant to ensure stability of the RHMPC scheme by enforcing that all temperatures be at or below their limits by the end of the prediction horizon. The terminal set is defined as follows:

$$\mathcal{T}_x = \left\{ x \,\middle|\, \Delta\hat{T}[M] = 0 \land x[M] \in \mathcal{X} \right\} \subset \mathcal{X}. \tag{4.25d}$$

Remark IV.10 (Terminal constraint & Feasibility). Terminal constraint set $\mathcal{T}_x$ is compact and contains the "origin" (established by line temperature limits and Level 1 reference values), as required by standard stability arguments [36]. This guarantees that line temperature overloads will be alleviated by MPC control actions. However, terminal constraints may, in general, impact feasibility of QP problem if the prediction horizon, M, is chosen sufficiently short. To ameliorate concerns of feasibility in this problem, M is appropriately chosen and slack variables are added to the power balance in (4.20f) to prevent network infeasibilities during line tripping and possible islanding.

Given the complete controller model description provided by (4.20), (4.24), and (4.25) the state and input vectors can be defined by:

$$x := \mathrm{col}\{\Delta\hat{T}, E, f_G\} \tag{4.26a}$$

$$u := \mathrm{col}\{\Delta f_G, f_{G,W}^{\mathrm{spill}}, f_D^{\mathrm{shed}}, Q_c, Q_d, \psi^{\mathrm{PST}}\} \tag{4.26b}$$

$$z := \mathrm{col}\{\theta, \theta^+, \theta^-, \theta^{PW}, f, f_{\mathrm{loss}}, f_D, f_{\mathrm{Gw}}, Q^{\mathrm{T}}\}. \tag{4.26c}$$

4.5.2.1 Stabilizing temperature overloads

To ensure correct temperature dynamics in (4.20b), the convex relaxation of line losses must be tight whenever a line temperature rises above its limit (i.e. $\Delta T_{ij} > 0$). This is guaranteed by the following theorem:

Theorem IV.11 (Temperature and Convex Relaxation). *Assume $g_{ij} > 0$ and losses in (4.20f) are fixed to a predetermined value over the duration of the prediction horizon. If the temperature of line $(i, j) \in \mathcal{A}$ exceeds its limit at time $l + 1$, then the convex relaxation is tight with respect to line (i, j) for all previous time-steps. That is, if $\exists l \in \mathcal{M}$ and $(i, j) \in \mathcal{A}$ such that $\Delta T_{ij}[l + 1] > 0$, then adjacency conditions are*

satisfied and $\theta_{ij}^+[\kappa]\,\theta_{ij}^-[\kappa] = 0,\,\forall\,\kappa \leqslant l.$ *Hence the convex relaxation associated with line* (i,j) *is tight* $\forall\,\kappa \leqslant l.$

Proof. The full proof is given in Appendix B. To sketch the proof, let $\{\Delta T_{ij}[l]\}_{l=1}^M$ be an optimal MPC temperature trajectory for line (i,j) and assume $\exists\,l \in \mathcal{M}$ such that $\Delta T_{ij}[l+1] > 0$ but the solution is **not** tight for some $\kappa \leqslant l$. That is, losses are overestimated via the convex relaxation (i.e. either $\theta_{ij}^+[\kappa]\,\theta_{ij}^-[\kappa] > 0$ and/or adjacency conditions are not satisfied in the PWL relaxation, see Figure 2.5). Then a feasible solution can be derived which is identical to the optimal solution except that it enforces a tight formulation at time κ and reduces line losses accordingly, say from $f_{ij,\text{relax}}^{\text{loss}}[\kappa] > f_{ij,\text{tight}}^{\text{loss}}[\kappa]$. According to (4.20b), decreased losses at time κ result in lower temperature at later times, which implies that the temperature overload at time $l+1$ must be less under the tight feasible solution. Since the objective function penalizes $\Delta \hat{T}_{ij}[\kappa]$ and losses are fixed in power balance equation, the feasible tight trajectory provides a lower cost solution than the relaxed optimal trajectory. This is a contradiction. Thus, if (i,j) has a temperature overload at time $l+1$, the formulation is locally tight $\forall\,\kappa \leqslant l.$ □

Remark IV.12 (Fixing losses over the prediction horizon)**.** Under the standard convex relaxation of a PWL approximation of line-losses [69], it is implicitly assumed, for tightness of the formulation, that nodal prices (i.e. LMPs) are non-negative. Negative nodal prices arise for nodes where increasing power consumption leads to decreased overall system costs. For example, if a line is congested or trips at time k and forces a generator at node i to decrease output (i.e. $f_{G,i}[k] - f_{G,i}[k-1] < 0$), then it can be shown that the nodal price at that node at time k will become negative. This breaks the assumption of non-negative nodal prices and prevents a tight formulation of losses. Fictitious losses can then "consume" power via the power balance equation (for nodes with negative LMPs) and reduce the overall objective function value. Similar but more thorough conclusions have been reached by authors in [70, 94] as it relates to convex relaxations in power systems.

To overcome the challenge of negative LMPs in this work, losses are fixed in (4.20f) to a value $f_{ij,k}^{\text{loss,est}}$ obtained from the most recent measurement of the AC system. The proof in Appendix B does not, therefore, require consideration of nodal prices. Furthermore, by fixing losses in the power balance equation, the network structure does not affect the convex relaxation. The astute reader will note that with losses fixed in (4.20f), the computed control actions will be slightly inconsistent with the actual AC system. However, this loss approximation typically constitutes less than 0.1% of total load, and is corrected by feedback in the MPC formulation.

4.5.3 RHMPC objective function

The objective of the MPC scheme is to determine the optimal control actions that alleviate temperature overloads, $\Delta \hat{T}_{ij}$, while minimizing deviations from the economic set-points established by Level 1. Accordingly, the MPC objective function

is composed of the terms:

$$p_o(\Delta \hat{T}_{ij}[l])^2 \quad \text{- line temperature overload}$$
$$p_g(f_{G_g}[l] - f^{\text{sp}}_{G_g,k+l})^2 \quad \text{- deviation from reference output}$$
$$p_r(\Delta f_{G_g}[l] - \Delta f^{\text{sp}}_{G_g,k+l})^2 \quad \text{- changes in generation ramping}$$
$$p_e(E_n[l] - E^{\text{sp}}_{n,k+l})^2 \quad \text{- deviation from reference SOC}$$
$$p_q(Q_n[l] - Q^{\text{sp}}_{n,k+l})^2 \quad \text{- changes in reference dis/charging}$$
$$p_s(f^{\text{shed}}_{D_d}[l])^2 \quad \text{- load control}$$
$$p_w(f^{\text{spill}}_{G,\text{wind}}[l])^2 \quad \text{- wind spill}$$
$$p_p(\psi^{\text{PST}}_{ij}[l] - \psi^{\text{PST,sp}}_{ij,k+l})^2 \quad \text{- deviation from PST reference shift}$$

where reference values, denoted $(\cdot)^{\text{sp}}$, refer to the economically optimal set-points computed in Level 1.

Based on the MPC objectives and the state and input definitions in (4.26), the weighting matrices in (4.20a), (4.18) are given by:

$$Q = \text{diag}\{p_o I, \frac{p_e}{10M^2}I, \frac{p_g}{10M^2}I\} > 0 \tag{4.27a}$$

$$S_M = \text{diag}\{p_o I, p_e I, p_g I\} > 0 \tag{4.27b}$$

$$R = \text{diag}\{p_r I, p_w I, p_s I, p_q I, p_q I, p_p I\} > 0 \tag{4.27c}$$

where I represents square identity matrices of appropriate dimensions and diag$\{.\}$ is a block-diagonal matrix. Note that the terminal cost matrix S_M penalizes deviations from economical references for storage SOC and conventional generation states more severely than does the weighting matrix Q. This is because the MPC does not care *how* these reference signals are tracked, only that they are being considered by the end of the horizon.

4.5.4   Base-case Controller

To enable a reasonable comparison of the performance of the RHMPC, a base-case controller is necessary. The base-case controller serves as an estimate of human operator behavior during a system emergency (i.e. contingency response). Clearly, modeling a human operator is non-trivial as standard emergency procedure varies broadly across regions, involves power market factors, and the experience of a human operator is not amenable to an implementable mathematical (and repeatable) framework. However, the crude base-case presented here captures the underlying objectives of the operator:

- Alleviate thermal (power) overloads by rescheduling or curtailing generation, while considering ramp-rate limits and incremental generator cost curves.

- Employ linear methods, such as, power transmission distribution factors (PTDFs), generation shift factors (GSFs), and transmission loading relief (TLR) procedures to make quick control decisions to relieve thermal overloads [95].

- Shed load only as an absolute last resort.

- Do not consider energy storage.

Thus, mapping the above operator traits into an MPC-based framework serves as the base-case:

- **Base-case implementation**

  - Replace $\Delta \hat{T}[k]$ with a relative algebraic overload:
    $\hat{o}_{ij}[k] = 10 \max\{0, (|f_{ij}[k]| + 0.5 f_{ij}^{\text{loss,est}}[k])/u_{ij} - 1\}$
    That is, if a line is 10% overloaded, $\hat{o}_{ij} = 1.0$.

  - Consider PTDF, GSF, and TLR implicitly as a 1-step MPC process akin to Level 2 (i.e. set $M = 1$) and include overloads $\hat{o}_{ij}[0|k]$, $\hat{o}_{ij}[1|k]$ in objective and terminal costs.

  - Penalize load shedding and control of energy storage devices heavily.

  - Remove terminal constraints on overloads, $\mathcal{T}_x$.

  - Set $R_{\text{base}} = R$, $Q_{\text{base}} = S_M$, $S_{M,\text{base}} = S_M$.

4.5.5 Actual system model (plant)

The AC power flow is generally accepted as a valid representation of the actual physical power system (i.e. the plant). Therefore, the control actions recommended by the MPC, which utilizes the strictly linear model described in Section 4.5.2, is applied to an AC model of the system at each time-step. In addition, resulting losses from the AC power flow are utilized in the non-linear IEEE Standard 738 conductor temperature model to better capture the effects of MPC recommendations on the actual system. Finally, the actual energy storage model does not allow for simultaneous charging and discharging in the same time-step and instead employs the projected control action $Q_n^{\text{T}}[k]$ such that $Q_{\text{c},n}[k]Q_{\text{d},n}[k] \equiv 0$.

The higher the temperature, the more likely line tripping becomes. To capture the inverse relationship between temperature and expected time to trip in the actual system, the probabilistic thermal line outage model from Section 4.2.2.2 is utilized with rate parameter $\lambda = 70$.

4.5.6 Case-study: IEEE RTS-96

The bilevel cascade mitigation scheme illustrated in Figure 4.13 is implemented for a case study. Notice how the scheme updates the reference immediately following a disturbance to capture the correct topology. The hierarchical control scheme developed above is applied to an augmented version of the IEEE RTS-96 power system test-case, which is described in full details in [68]. For completeness, a brief overview of RTS-96 is included here.

The RTS-96 system consists of 138 kV and 230 kV subsystems. The network is organized into three interconnected physical regions, as illustrated in Figure 4.14, and consists of 73 nodes and 120 branches, of which 15 branches are IPTs, one is a PST, and the remaining are overhead transmission lines (138 & 230 kV). Note that
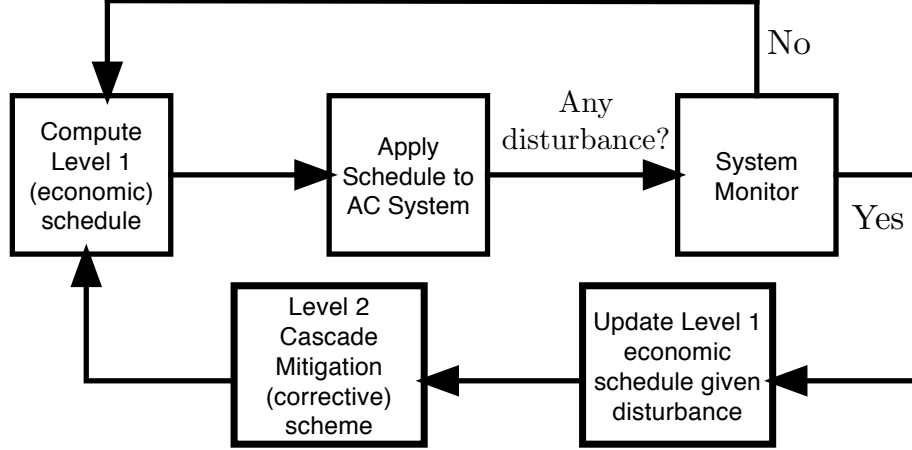
Figure 4.13: Overview of proposed control scheme showing Level 1 (economical) and Level 2 (corrective) interaction.

the three underground cables in the original RTS-96 system have been modified into overhead lines to enable application of a single thermodynamic model. Transformer temperature overloading is not considered in this paper since the thermodynamic responses is applicable on a significantly slower time-scale and are generally equipped with external controls for managing temperatures (i.e. fans).

This case study will highlight the advanced contingency management available from the proposed hierarchical control scheme, however, the RTS-96 system is designed as a highly reliable system with large nominal thermal ratings. To bring the system closer to its limits and engender worthwhile scenarios, thermal ratings u_{ij} have been reduced by 40%, which yields line temperature limits that are reduced to the range of 60-70°C. Furthermore, ramp-rates have been reduced by 82.5% to enhance the role of storage in congestion management and highlight Level 2 performance. For the temperature dynamics, the RTS-96 system data only specifies per-unit resistance and reactance and line length but not the conductor types (i.e. diameter, heat capacity). Therefore, this case-study employs ACSR conductors 18/1 Waxwing (138 kV) and 26/7 Dove (230 kV), which represent reasonable choices given the reduced line ratings. The values for Dove and Waxwing conductors along with system parameters are shown in Table 4.9. Values in brackets represent ranges.

The objective weighting factors utilized in RHMPC Level 2 and base-case are presented in Table 4.10. Note that overload coefficient, p_o, for the base-case, reflects thermal power overload ($\hat{o}_{ij}$) and not temperature. Also, the storage control coefficient for the base-case, $p_q = 1000$, is to reflect that this resource is not available in decision-making. Regarding storage, an interesting phenomena was observed for high-wind scenarios: when the penalty on wind spill greatly exceeded the storage control penalty, the RHMPC scheme would burn excess wind energy through the lossy energy charge/discharge cycles to reduce wind spill. Therefore, penalties on wind-spill are set below those of storage. Control changes to generator inputs, Δf_G, are penalized with factors $p_r = \max\{0.05, \alpha_G / \max_G \{\alpha_G\}\}$ in Level 2 while for the base-case: $p_r = 0.1 \max\{0.1, \alpha_G / \max_G \{\alpha_G\}\}$. Recall, α_G is given by Level 1 objec-
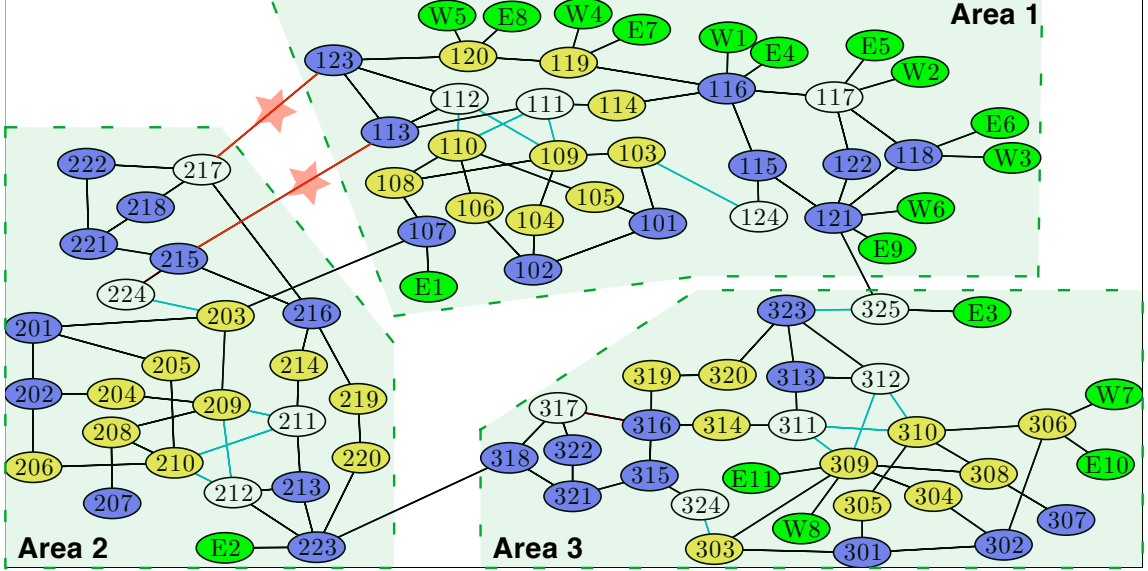
Figure 4.14: Augmented IEEE RTS-96 network with storage (E), wind (W) available at different buses. Specific buses are denoted with three digits. The first digit indicates area and the latter two are intra-area designators. Bus types are indicated by color: generator (blue), load (yellow), and through-put (white). Edges represent transmission lines (black) and transformers (aqua/gray). The disturbance (i.e. tripped lines) is displayed with stars: edges 113-215 and 123-217. Note that storage and wind nodes are attached to buses as indicated in figure, but the associated edges do not represent transmission lines.

tive: $\alpha_G f_G^2 + \beta_G f_G$. The cost-curve parameters (α_G, β_G) utilized in this case-study are from [96, Table 1] and repeated here in Table 4.11 for completeness. Note that generators with ID Ug have upper output limit $f_G[k] \leqslant \overline{f_G} = g$ MW.

Remark IV.13 (Role of Unit Commitment). Since no minimum generator outputs are specified in [68], $\underline{f_G} = 0$ is assumed as minimum outputs available for dispatch.

An overview of Level 2/base-case is displayed in Figure 4.13. Since longer timescales are associated with the early stages of a cascade failure, it allows for significant computing to be performed immediately following a disturbance. Therefore, the updated economically optimal set points are computed by Level 1 immediately following disturbance. Furthermore, the Level 2 cascade mitigation scheme does interact with the AC system (i.e. the plant) and is subject to the probabilistic line outage model between each time-step, which is illustrated in Figure 4.15.

Remark IV.14 (Sampling time and outage probability). The probabilistic outage model was tuned with respect to $T_s = 1$ minute. Development of the probabilistic line outage model parameter λ required consideration of sampling time T_s, since each time-step represents a random event (i.e. rolling a dice). The probability of a line tripping for time-step k considers the probability of the line tripping during the interval $[kT_s, (k + 1)T_s)$. That is, if the probabilistic line outage parameter for sampling time

Table 4.9: Network model parameters used in case-study.

Model Parameter	Value		Unit
3-phase power base, S_b	100		MVA/pu
Energy storage base, E_b	100		MWh/eu
Monetary unit base, M_b	10,000		\$/mu
Sampling Time, T_s	60		s
Storage SOC limits, $\overline{E}_i$	2		eu
Storage power limits, $\overline{Q}_c, -\overline{Q}_d$	0.25		pu
Nominal wind power, $f_{G,\text{wind}}^{\text{nom}}$	Fig. 4.16a		pu
Nominal loads, f_D^{nom}	Fig. 4.16b		pu
Overcurrent protection limits, $\overline{\Omega}$	3		-
Ambient Temperature, T_{amb}	35		C
Wind speed, angle, $v_w \angle \theta_w$	0.61, $\pi/2$		m/s, rads
Solar heat flux rate, Q_s	1.03		kW/m^2
Solar absorptivity, α	0.9		-
Coefficient of emissivity, ϵ	0.7		-
Line-to-line base voltage, V_b	138	230	kV
Thermal rating, u_{ij}	1.05	3.00	pu
Diameter, D_{ij}	15.5	23.5	mm
Heat capacity, $mC_{p,ij}$	383	916	J/C-m
Ampacity, $I_{\text{lim},ij}$	439	753	A
Resistance per unit length, R_{ij}	[103,118]	[55,66]	$\mu\Omega$/m
Temperature limit, $T_{\text{lim},ij}$	[62,64]	[67,71]	C
Temperature coefficient, τ_{ij}	0.796	0.888	-
Ambient coefficient, γ_{ij}	0.193	0.104	-
Loss coefficient, ρ_{ij}	0.157	0.066	C-m/W

$T_s = 1$ minute was used for a sampling time $T_s = 1/100$ minute, then the probability of tripping would incorrectly increase by a factor of 100, because for 1 minute, the random event would have taken place 100 times. A simple solution to this issue is to consider the ratio of the sampling time for which the outage model was tuned T_s^{tune} and the actual sampling time T_s. Then, multiply the resulting temperature-based probability by the factor T_s/T_s^{tune}.

4.5.7 Simulation Results

The case-study detailed in Section 4.5.6 is simulated in Matlab according to Level 1, Level 2, and base-case implementations. Initially, the system is operated economically according to Level 1. However, at hour 18 (low wind, high demand), a two-line outage (i.e. the disturbance) trips lines 113-215 and 123-217. Performance and behavior of Level 2 MPC (with $M = 5, 10, 20, 30,$ and 45) and Base-case are

Table 4.10: Objection function coefficients for Q, R, S_M matrices for RHMPC and base-case systems.

Model	p_o	p_e	p_g	p_r	p_w	p_s	p_q	p_a
Lvl 2	1	200	200	[0.05,1]	0.15	250	0.2	0.01
Base	1	0.01	0.01	[0.01,0.1]	0.5	500	1000	0.1
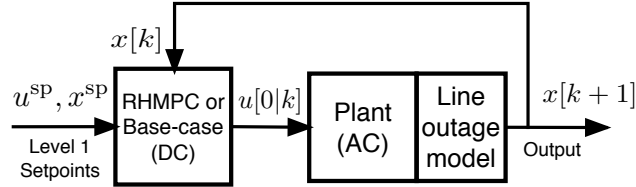
Figure 4.15: Overview of Level 2 RHMPC and base-case implementation.

discussed below.

The two-line outage, at hour 18, causes the remaining inter-area transmission line 107-203 to become severely overloaded ($> 1.25u_{ij}$). The Level 2 MPC scheme alleviates the temperature overloads and brings the system safely to the updated economic set points provided by Level 1. However, the base-case undergoes a cascade failure with line-tripping bringing the system to a voltage collapse after 29 minutes (as exemplified by non-convergent AC power flow). The base-case cascade failure evolves as follows:

- $k = 3$: line 107-203 trips at $\Delta T_{ij}[3] = 13.5\,^\circ$C.

- $k = 16$: line 114-116 trips at $8.14\,^\circ$C.

- $k = 26$: line 113-123 trips at $11.4\,^\circ$C.

- $k = 28$: lines 103-109 & 112-123 trip at 16.8 & $20.7\,^\circ$C

- $k = 29$: Voltage collapses! **"Blackout."**

For the base case, Area 1 undergoes a voltage collapse $k = 29$, as illustrated in Figure 4.17 when the minimal voltage magnitude drops below 0.87 pu.

The maximum line temperatures for each time-step of the base-case and MPC runs are illustrated in Figure 4.18a. Note that MPC is able to avoid high temperature overloads and drive the temperatures below their respective limits by minute $k \approx 75$. After this time period, a few lines hover above their temperature limits. However, this is due to model uncertainty regarding non-linear temperature and AC power system models in the plant and the linear temperature and DC models employed in the controller and for the Level 1 set points. In particular, the largest temperature deviations above limits are associated with 138 kV lines that exhibit $x_{ij}/r_{ij} < 4$, which engenders errors in the DC approximation of an AC system. Basically, the DC model incorrectly informs the controller that losses are low enough that the temperature will

Table 4.11: Generator ramp-rate and cost parameters.

Generator ID	# of units	Ramp rate (pu/hr)	Cost-curve parameters	
			β_G ($/pu-h)	α_G ($/pu^2-h)
U12	15	0.105	1.57	2.87
U20	12	0.315	1.66	2.1
U50	18	0.105	0.11	0.01
U76	12	0.210	0.19	0.07
U100	9	0.735	1.36	0.22
U155	12	0.315	0.182	0.01
U197	9	0.315	1.39	0.09
U350	3	0.420	0.179	0.01
U400	6	2.10	0.062	0

(a) Hourly wind-power profiles.

(b) Hourly aggregate demand profile
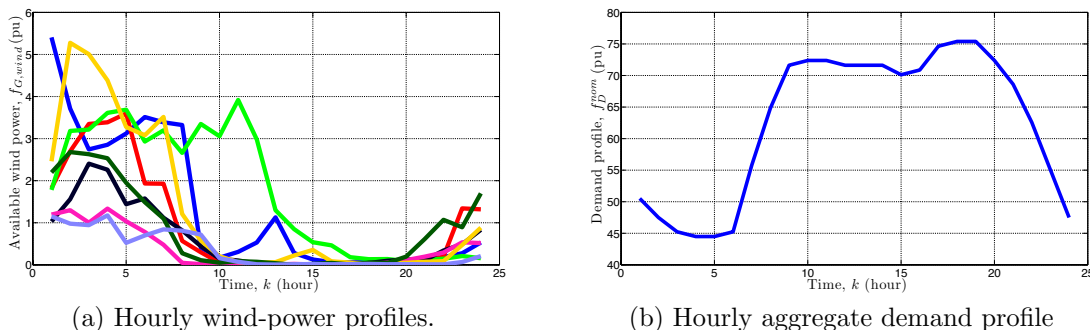
Figure 4.16: Wind power and demand profiles from 8 turbines and 51 loads in the RTS-96 network over 24-hour horizon

drop below its limit in the next time-step under negligible control action. Then, the AC power flow yields higher-than-DC losses and temperature stays above limit. The controller repeats these incorrect estimates of losses until control action is required or load-patterns autonomously reduce line loadings below limits. However, the errors associated with the model uncertainty are highlighted in Figure 4.18b where line flows are less than 6% above their thermal rating for $k > 50$, which is within expected standard DC approximation error levels [97].

The control of line temperatures is achieved from Level 2 MPC schedules via available control actions: load-shedding, wind curtailment, and energy storage injections. Figures 4.18c, 4.18d, 4.18e illustrates the aggregated control signals required to alleviate temperatures (with Level 2). Contrasting MPC runs with the base-case, it is clear that load-shedding and and storage control plays a major factor in Level 2 MPC performance. Namely, by initially shedding less than 3% of the aggregate load (Fig. 4.18c) and curtailing storage injections (Fig. 4.18e), the temperature is brought to within its limit. For $k \in [75, 240]$, storage injections exceed reference levels to bring SOC back to economical reference levels while wind curtailment (Fig. 4.18d)
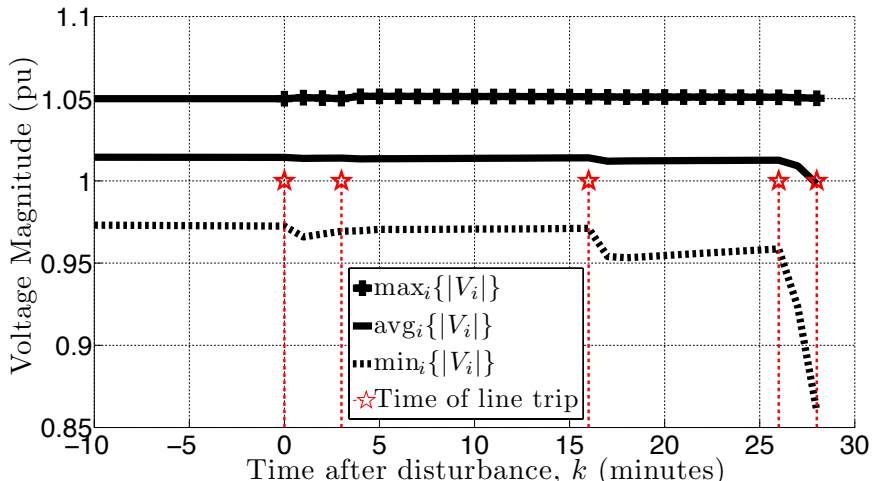
Figure 4.17: Voltage levels under cascade failure event from base-case operation high-lighting voltage collapse.

is employed as cheap control to bring/keep temperatures below limits under model uncertainty.

The Level 2 MPC performs a balancing act between economically optimal references and ensuring safety criteria. This balance is highlighted in Figure 4.18f, where the cost of generation is illustrated for MPC runs and the base-case. To ensure safety, the different MPC cases initially sacrifice economical optimality by deviating from the Level 1 set points. For $k > 120$, the system returns to economically optimal levels with model uncertainty causing some minor discrepancies. Recall that Level 1 (economic) and Level 2 (safety) are computed based on the DC power flow model, but the actual implementation utilizes the AC power flow.

It is worthwhile to point out the effect on performance from varying the prediction horizon. Assuming the QP problem remains feasible, by employing the terminal constraint $\mathcal{T}_x$, the MPC is required to bring line temperatures within their limits by the end of the horizon. Therefore, as the prediction horizon decreases, the MPC scheme utilizes more aggressive (and expensive) control actions to alleviate overloads as evidenced by load-shedding trajectories. In addition, with decreasing M, the terminal constraint on temperature, generally, causes less severe overloads and brings smaller departures from economic references as established with generation costs.

As alluded to Section 4.2.3, the approach employed to show stability of the RHMPC scheme relies on Lyapunov-type arguments. Specifically, it is sufficient to show that the objective function that defines that RHMPC scheme is a Lyapunov function. From the Lyapunov ideas, suitable "ingredients" can be derived, which allow for straightforward stability results for linear systems. For the RHMPC scheme simulated in this case-study, stability was ensured with positive-definite objective weighting matrixes and the terminal constraint $\mathcal{T}_x$. To illustrate that this precipitates a Lyapunov function (and guarantees stability), Figure 4.19 plots the total cost over time of each RHMPC prediction-horizon example and the base-case controller. It can be seen that the cost function does behave as a Lyapunov function for all

Table 4.12: Average QP solver times for different M.

MPC M-value	5	10	20	30	45
Average Time (sec)	0.8	2	5	9	16

RHMPC instances, while the base case exhibits unstable behavior (mainly due to lines tripping). The astute reader may also notice that as the prediction horizon decreases from 45 to 5 minutes, the total cost increases, which is in line with standard MPC results. This increase in total cost due to the terminal constraint and that as MPC predicts further into the future, the MPC is able to respond earlier to predicted events and apply correspondingly cheaper control. Of course, the quality of predictions is coupled with the quality of forecasts, which are assumed perfect in this case study. Generally, with temporally deteriorating forecasts, the reduction in total cost as a function of prediction horizon reaches a limit when the forecasts provide no new information.

In addition, it could be argued that for $M > 20$ the improved performance from increasing M is negligible compared with increased computational complexity of solving the open-loop (QP) problem. Table 4.12 describes the approximate solution times for the average instances of MPC for different M-values. The simulations were performed on a personal computer with Matlab and GUROBI and it would be reasonable to assume that, given the solver times, dedicated hardware may allow for real-time implementation of RHMPC scheme. Of course, any implementation would require considerations for the cyber-couplings that arises between sensors, measurements, state estimators, computation, and control. Implementation, except for maintaining computational tractability of the RHMPC scheme, is outside the scope of this work.

Furthermore, the utilization of estimated AC line losses in the power balance equation effectively decouples the transmission lines (losses and temperatures) in the system and enables the RHMPC scheme to stabilize line temperature via a convex relaxation. However, using fixed estimates of line losses over the prediction horizon in the power balance equation in the RHMPC model manifests itself as a power mismatch in the actual "real" system. The total power mismatch due to the fixed estimate is smaller than 0.05 pu ($< 0.1\%$ of total load) and is, essentially, rejected as a model inaccuracy by the RHMPC scheme as displayed in Figure 4.20. The thick blue line represents the closed-loop response to mismatches (i.e. updates AC estimates) while the thin red lines are open-loop mismatch trajectories from each time-step. The large closed-loop spikes occur due to the hourly Level 1 step-changes in the economically optimal input reference u^{sp} for storage and generators. For example, see the hourly reference signal for Q_n in Figure 4.18e). The RHMPC scheme ability to reject model uncertainty is well-illustrated with these power mismatches.

Finally, to illustrate the locally tight nature of the convex relaxation, Figure 4.21 presents the adjacency, absolute-value, and temperature conditions for RHMPC predictions $[l|k = 1], l \in \mathcal{M}$ with prediction horizon $M = 30$. Notice, how any predicted temperature overloads at time $l+1$ yields a tight relaxation for all previous time-steps

$p \leqslant l$. For example, line 52 (207-208) is predicted to have a temperature overload for $l \in [19, 23]$ and adjacency and absolute values relaxations are tight for all $l < 23$.

4.6   Summary

This chapter presents two bilevel hierarchical control approaches to cascade mitigation in power systems. The first approach represents initial efforts aimed at mitigating the effects of cascading failures in multi-energy hub systems and is based on shrinking-horizon MPC (SHMPC) with a deterministic line outage model. The SHMPC scheme illustrates the active role of energy storage and conversion processes and the benefit from balancing both economic and security objectives in the cascade mitigation scheme. It is shown that energy resources must be carefully regulated because MPC has a tendency to over-exploit stored energy to the detriment of long-term energy requirements.

The ideas uncovered by the SHMPC scheme are advanced by the development of a receding horizon MPC (RHMPC) cascade mitigation scheme applied to electric transmission systems with energy storage. The RHMPC scheme balances economic and security objectives through the use of a higher-level optimal scheduling process and a lower-level model predictive control (MPC) strategy. The MPC design rejects disturbances (contingencies) while tracking the optimal set-points established by the higher level. Disturbance rejection exploits the thermal overload capability of transmission lines. This allows time for adjustments to be made to controllable resources that include generation levels, energy storage and demand response. A convex relaxation is applied to the AC power flow to develop a piece-wise linear approximation for line losses. This formulation is proven to be sufficient to enable RHMPC to drive line temperatures below limits. As supported by an augmented IEEE RTS-96 case study, the RHMPC scheme can significantly improve system reliability and economic performance by leveraging the temporal nature of storage and conductor temperatures.

(a) Line temperature responses

(b) Relative line flow response

(c) Aggregate load shedding

(d) Aggregate wind curtailment

(e) Aggregate storage (dis)charging

(f) Cost of generation with reference from Level 1
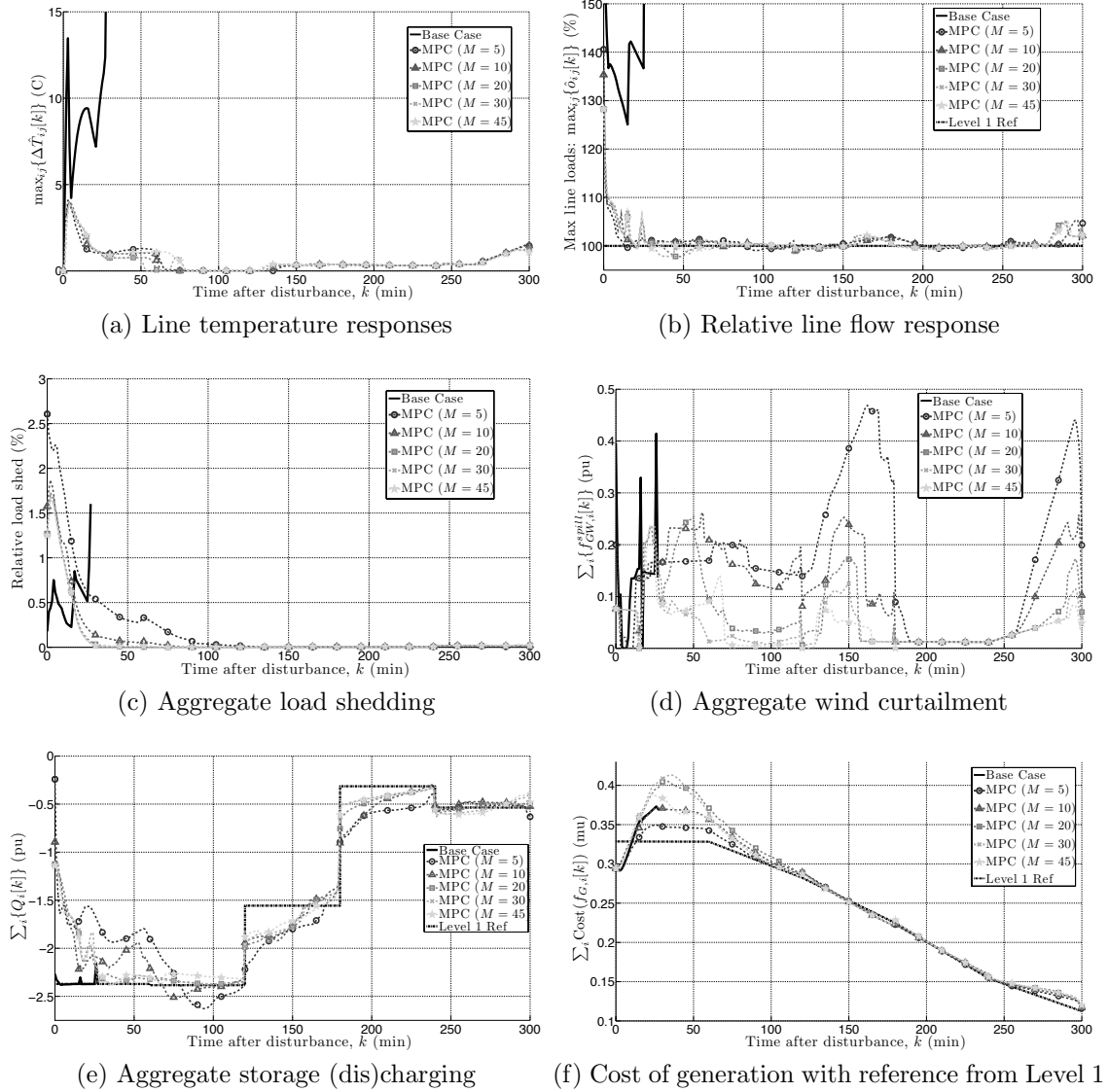
Figure 4.18: Case-study simulation results of RHMPC and Base-case.
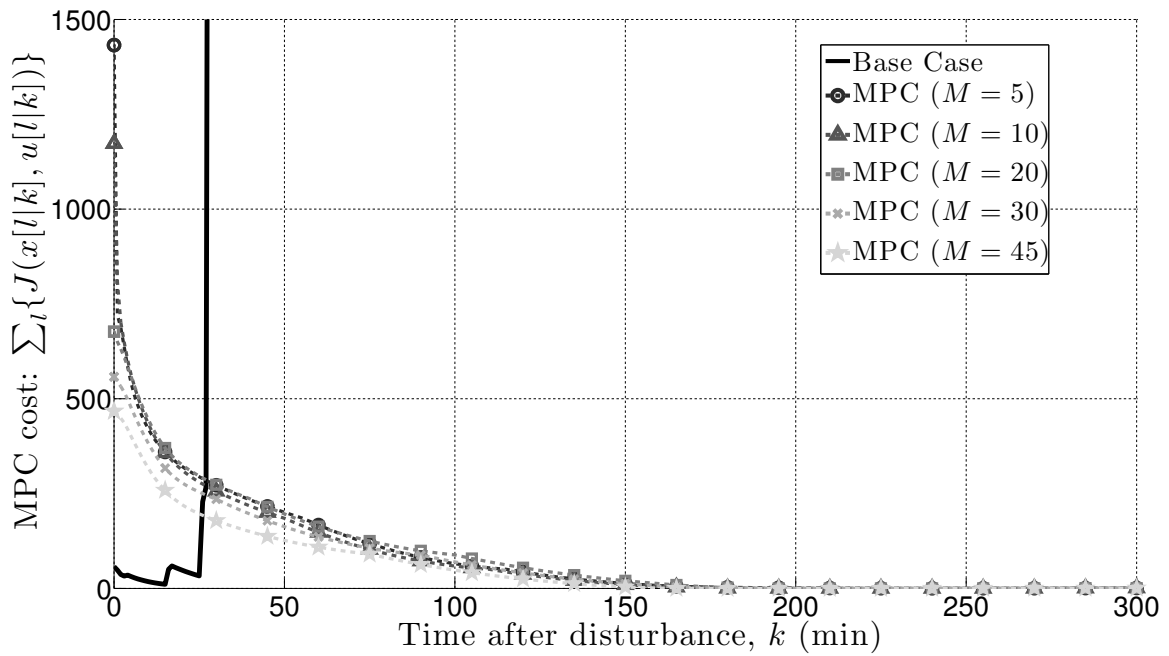
Figure 4.19: Illustration that the RHMPC cost-function behaves as a Lyapunov function and converges to "origin" (as defined by economic references and non-overloaded lines).
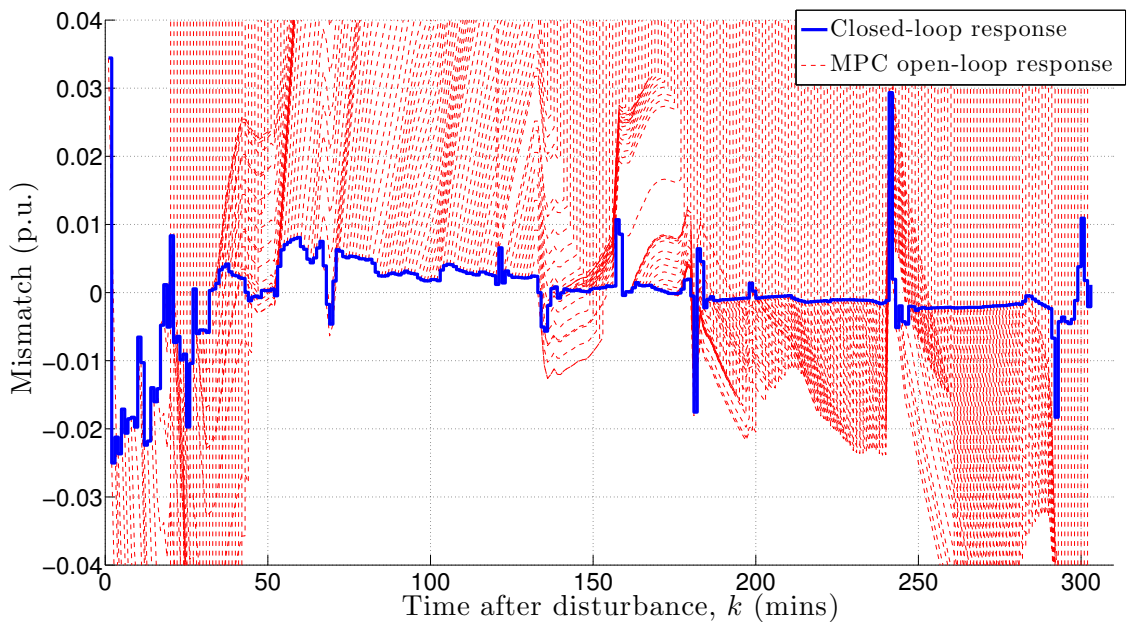
Figure 4.20: Illustration of RHMPC instance $M = 20$ that the scheme can attenuate power mismatches caused by fixed AC loss estimate in power balance.
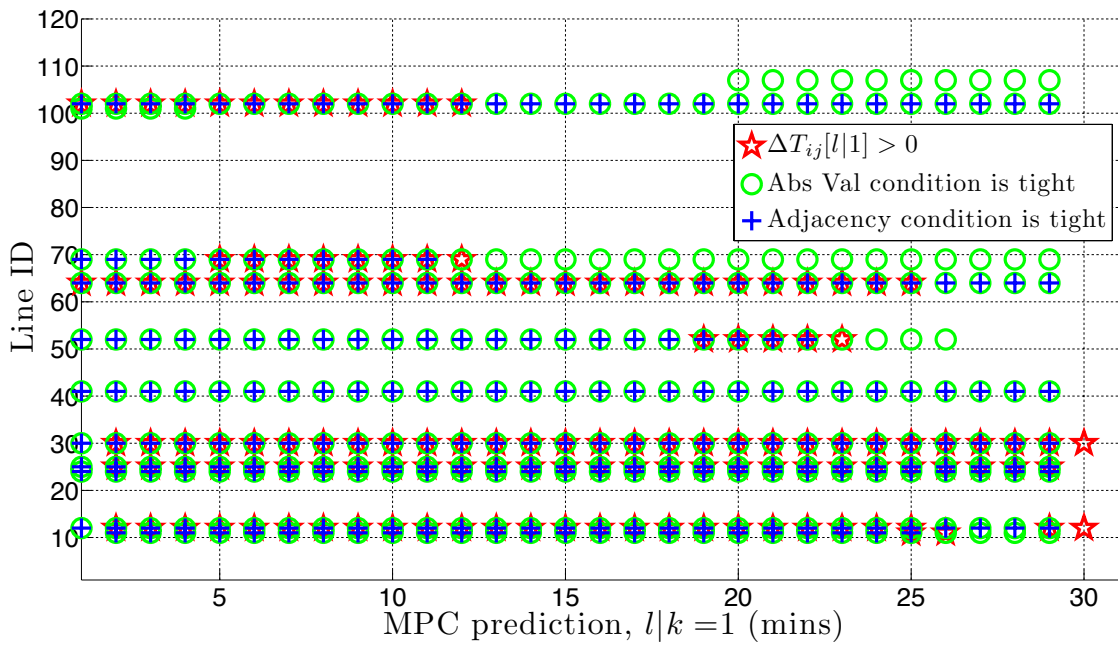
Figure 4.21: Illustration that $\Delta T_{ij}[l|k] > 0$ is a sufficient condition for RHMPC and ensures a locally tight formulation of line losses.

Distributed Model-predictive Overload Prevention via Load Control

5.1 Introduction

Distribution utilities are becoming increasingly aware that their networks may struggle to accommodate large amounts of plug-in electric vehicles (PEVs). In particular, uncoordinated overnight charging is expected to be problematic, as the corresponding power demand exceeds the capacity of most distribution substation transformers. In this chapter, a dynamical model of PEVs served by a single temperature-constrained substation transformer is presented and a centralized scheduling scheme is formulated to coordinate charging of a heterogeneous PEV fleet. Because prediction errors and fluctuations in background demand can be severe due to a low extent of aggregation in the distribution network, feedback to disturbances is introduced by solving the scheduling problem in a receding horizon fashion. This results in a centralized MPC scheme. The centralized scheme is then decomposed into a set of local control laws, which determine the charging strategy of each individual electric vehicle, and which can be coordinated via a common (pseudo-)price for electrical energy. This price is generated by a centralized agent, via application of the dual-ascent method, in such a way that the aggregated power demand is kept within its operational limits and is optimal upon convergence. Then, an implementation is proposed in which this distributed open-loop problem is embedded in an MPC scheme to introduce robustness against exogenous disturbances. Simulations of a realistic charging scenario illustrate the effectiveness of the so-obtained incentive-based coordinated PEV control scheme in terms of performance and enforcing the transformer's thermal constraint.

This work appears in the proceedings of the 2012 American Control Conference [98].

5.2 Basic notation and definitions

Let $\mathbb{R}$, $\mathbb{R}_+$, $\mathbb{Z}$ and $\mathbb{Z}_+$ denote the sets of reals, non-negative reals, integers and non-negative integers, respectively. For each $c \in \mathbb{R}$ and $\Pi \subseteq \mathbb{R}$ let $\Pi_{\geqslant c} := \{k \in \Pi \mid k \geqslant c\}$ and similarly, $\Pi_{\leqslant c}$. Let $\mathbb{Z}_\Pi := \mathbb{Z} \cap \Pi$. For a finite set $\{x_i\}_{i \in \mathbb{Z}_{[1,N]}}$, $x_i \in \mathbb{R}^{n_i}$,
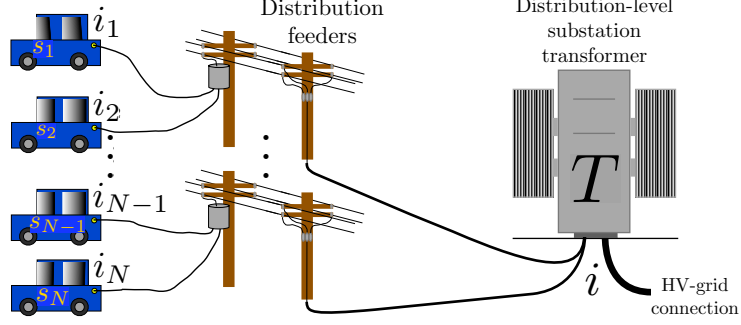
Figure 5.1: PEV charging via a single substation transformer.

$N \in \mathbb{Z}_{\geqslant 1}$, let $\mathrm{col}(\{x_i\}_{i\in\mathbb{Z}_{[1,N]}})$ and $\mathrm{col}(x_1,\ldots,x_N)$ denote the vector $\left(x_1^\top,\ldots,x_N^\top\right)^\top$. Let $\mathbf{1}_n$ be the all-one vector $\begin{bmatrix} 1 & \ldots & 1 \end{bmatrix}^\top$ in $\mathbb{R}^n$, and $\mathbf{I}_n$ the n by n identity matrix. The i-th element of a vector $x \in \mathbb{R}^n$ is denoted by $[x]_i$. Define projection $[x]_+ \in \mathbb{R}_+^n$ by $[[x]_+]_i := \max\{0, [x]_i\}$. Let $\mathbf{z} := \{z(l)\}_{l\in\mathbb{Z}_+}$ with $z(l) \in \mathbb{R}^n$, $l \in \mathbb{Z}_+$, denote an arbitrary sequence. For some scalar $c \in \mathbb{R}$, let $\lceil c \rceil := \min_{k\in\mathbb{Z}_{\geqslant c}} k$ and let $|c|$ be its absolute value. All inequalities are interpreted elementwise.

5.3   Dynamical Model of PEV Charging

We begin by describing a model for the PEV charging problem. Consider a fleet of $N \in \mathbb{Z}_+$ plug-in electric vehicles, all connected to a distribution grid that is fed by a single substation transformer, see Fig. 5.1. Let the continuous-time charging dynamics of vehicle $n \in \mathcal{N} := \{1,\ldots,N\}$ be described by

$$\dot{s}_n(t) = \tilde{\eta}_n p_n(t) = \tilde{\eta} V_{\mathrm{AC}} i_n(t), \qquad t \in \mathbb{R}_+, \tag{5.1}$$

where $s_n(t)$, $p_n(t)\,[\mathrm{W}]$ and $i_n(t)\,[\mathrm{A}]$ denote the vehicle battery's normalized state of charge (SOC), the charging power and the charging current at continuous-time instant $t \in \mathbb{R}_+$, respectively. We assume that the rms grid voltage $V_{\mathrm{AC}}\,[\mathrm{V}]$ is constant. The parameter $\tilde{\eta}_n\,[\mathrm{J}^{-1}]$ is obtained as the ratio of the vehicle's charging efficiency $\alpha_n \in \mathbb{R}_{[0,1]}$ and battery size $\beta_n\,[\mathrm{J}]$. Note that the above dynamics are valid only for s_n in $\mathbb{R}_{[0,1]}$, where $s_n = 1$ and $s_n = 0$ mean that the battery of vehicle $n \in \mathcal{N}$ is fully charged and empty, respectively. Next, suppose that the charging profiles $i_n(t)$ are step-wise with step width $T_{\mathrm{s}}\,[\mathrm{s}]$, such that $i_n(t) := i_n[k]$ for $t \in \mathbb{R}_{[kT_{\mathrm{s}},(k+1)T_{\mathrm{s}})}$ and $k \in \mathbb{Z}_+$. Then, (5.1) yields

$$s_n[k+1] = s_n[k] + \eta_n i_n[k], \qquad k \in \mathbb{Z}_+, \tag{5.2}$$

where $s_n[k] := s_n(kT_{\mathrm{s}})$ and $\eta_n := T_{\mathrm{s}}\tilde{\eta}_n V_{\mathrm{AC}}\,[\mathrm{A}^{-1}]$.

The transformer that connects the distribution grid to the high-voltage transmission network is modeled as a single thermal mass with continuous-time temperature

dynamics

$$\dot{T}(t) = \frac{1}{C}\left\{R_c i^2(t) - \frac{T(t) - T_a(t)}{R}\right\}, \tag{5.3}$$

with aggregated current $i(t) := (\sum_{n \in \mathcal{N}} i_n(t)) + i_d(t)$ [A], transformer heat capacity C [J K^{-1}], heat outflow resistance R [K W^{-1}], coil resistance R_c [Ω], and where $T(t)$ [K] is the transformer core temperature at time instant $t \in \mathbb{R}_+$. The net background/non-PEV current $i_d(t)$ [A] and the ambient temperature $T_a(t)$ [K] act as exogenous disturbances. Using Euler forward discretization and sampling period T_s, the following discrete-time temperature model is obtained:

$$T[k+1] = \tau T[k] + \bar{\gamma}i^2[k] + \rho T_a[k], \tag{5.4}$$

where $\tau := \left(1 - \frac{T_s}{RC}\right) \in \mathbb{R}$, $\bar{\gamma} := \frac{T_s R_c}{C} \in \mathbb{R}_+$ and $\rho := \frac{T_s}{RC} = 1 - \tau \in \mathbb{R}_+$, and where $T[k]$ is the transformer core temperature at discrete-time instant $k \in \mathbb{Z}_+$. For stability, the sampling period is required to satisfy $0 < T_s < 2RC$, such that $\tau \in \mathbb{R}_{(-1,1)}$.

In what follows, we use a linearized version of (5.4) to allow for a tractable implementation of the charging control scheme described in Sect. 5.4. Linearization around the equilibrium point T^*, $i^* := \sqrt{\bar{\gamma}^{-1}\rho(T^* - T_a^*)}$ for $T_a := T_a^*$ and $i_d := 0$ yields the approximate transformer dynamics described by

$$\Delta T[k+1] = \tau \Delta T[k] + \gamma\left(\left(\sum_{n \in \mathcal{N}} \Delta i_n[k]\right) + i_d[k]\right) + \rho \Delta T_a[k], \tag{5.5}$$

with $\Delta T[k] := T[k] - T^*$, $\Delta i_n[k] := i_n[k] - \frac{i^*}{N}$ and $\Delta T_a[k] := T_a[k] - T_a^*$, and where $\gamma := 2\bar{\gamma}i^*$.

Next, let $\{s_n[l \mid k]\}_{l \in \mathbb{Z}_{[0,K]}}$ and $\{\Delta T[l \mid k]\}_{l \in \mathbb{Z}_{[0,K]}}$ be the SOC and temperature sequences generated by (5.2) and (5.5) from initial state $[\,s_1[k] \,\cdots\, s_N[k]\; \Delta T[k]\,]^\top \in \left(\mathbb{R}_{[0,1]}\right)^N \times \mathbb{R}$, charging rate sequences $\{\Delta i_n[l \mid k]\}_{l \in \mathbb{Z}_{[0,K-1]}}$, $n \in \mathcal{N}$, and disturbances $\{i_d[l \mid k]\}_{l \in \mathbb{Z}_{[0,K-1]}}$, $\{\Delta T_a[l \mid k]\}_{l \in \mathbb{Z}_{[0,K-1]}}$ over a finite prediction horizon $K \in \mathbb{Z}_+$. Next, consider the following sequence vector notation, i.e.,

$$\begin{aligned}
\mathbf{T}[k] &= \mathrm{col}\left(\{\Delta T[l \mid k]\}_{l \in \mathbb{Z}_{[0,K]}}\right) \in \mathbb{R}^{K+1} \\
\mathbf{s}_n[k] &= \mathrm{col}\left(\{s_n[l \mid k]\}_{l \in \mathbb{Z}_{[0,K]}}\right) \in \mathbb{R}^{K+1}, \qquad n \in \mathcal{N}, \\
\mathbf{d}[k] &= \mathrm{col}\left(\{d[l \mid k]\}_{l \in \mathbb{Z}_{[0,K-1]}}\right) \\
&:= \mathrm{col}\left(\left\{\left[\begin{smallmatrix} i_d[l|k] \\ \Delta T_a[l|k] \end{smallmatrix}\right]\right\}_{l \in \mathbb{Z}_{[0,K-1]}}\right) \in \mathbb{R}^{2K} \\
\boldsymbol{\pi}_n[k] &= \mathrm{col}\left(\{\pi_n[l \mid k]\}_{l \in \mathbb{Z}_{[0,K-1]}}\right) \\
&:= \mathrm{col}\left(\{\Delta i_n[l \mid k]\}_{l \in \mathbb{Z}_{[0,K-1]}}\right) \in \mathbb{R}^K, \quad n \in \mathcal{N},
\end{aligned}$$

and the sequence vector of aggregated charging current

$$\boldsymbol{\pi}[k] = \text{col}\left(\{\pi[l \mid k]\}_{l \in \mathbb{Z}_{[0,K-1]}}\right) := \sum_{n \in \mathcal{N}} \boldsymbol{\pi}_n[k] \in \mathbb{R}^K,$$

such that (5.2) and (5.5) yield the prediction model

$$\mathbf{T}[k] = \boldsymbol{\Phi}\Delta T[k] + \boldsymbol{\Psi}\boldsymbol{\pi}[k] + \boldsymbol{\Psi}_{\mathrm{d}}\mathbf{d}[k] \tag{5.6}$$

$$\mathbf{s}_n[k] = \boldsymbol{\Phi}_{\mathrm{s}}s_n[k] + \boldsymbol{\Psi}_{S_n}\boldsymbol{\pi}_n[k], \qquad n \in \mathcal{N}, \tag{5.7}$$

with transition matrices $\boldsymbol{\Phi} \in \mathbb{R}^{K+1}$, $\boldsymbol{\Psi} \in \mathbb{R}^{(K+1)\times K}$, $\boldsymbol{\Psi}_{\mathrm{d}} \in \mathbb{R}^{(K+1)\times(2K)}$, $\boldsymbol{\Phi}_{\mathrm{s}} \in \mathbb{R}^{K+1}$, $\boldsymbol{\Psi}_{S_n} \in \mathbb{R}^{(K+1)\times K}$.

5.4 Centralized Scheduling of PEV Demand

Next, we formulate a centralized load scheduling strategy that serves as a starting point for the incentive-based, distributed control scheme derived in Sect. 5.5.

We begin by observing that, for safety or performance reasons, PEV battery charging is subject to strict state and input constraints. Firstly, battery chargers usually come with a limited power capacity, i.e.,

$$\pi_{n,\min} \leqslant \pi_n[k] \leqslant \pi_{n,\max}, \qquad k \in \mathbb{Z}_+, n \in \mathcal{N}, \tag{5.8}$$

with finite $\pi_{n,\min} \in \mathbb{R}$, $\pi_{n,\max} \in \mathbb{R}_+$. Note that vehicle-to-grid technology, which enables power delivery to the network, can be taken into consideration via negative $\pi_{n,\min}$.

Secondly, to prevent transformer overheating, a (relative) temperature constraint is imposed, i.e.,

$$T^* + \Delta T[k] \leqslant T_{\max}, \qquad k \in \mathbb{Z}_+. \tag{5.9}$$

For simplicity, we restrict our attention to a static upper bound on temperature, even though this may be overly strict in practice. Normally, a slight temporary violation of (5.9) is allowed, provided that secure steady-state operating conditions are recovered within a sufficiently short subsequent cooling-down period.

Thirdly, by construction, the SOCs are bounded by

$$0 \leqslant s_n[k] \leqslant 1, \qquad k \in \mathbb{Z}_+. \tag{5.10}$$

Additionally, each PEV owner can set a certain SOC target that needs to be reached by the time they expect to leave their home. Thus, given (5.7) and initial states of charge $s_1[0], \ldots, s_N[0]$, the load scheduling scheme has to select, for all $n \in \mathcal{N}$, an appropriate charging profile $\boldsymbol{\pi}_n[k]$ such that a certain minimum battery state $S_n \in \mathbb{R}_{[0,1]}$ is attained at some discrete-time instant $K_n \in \mathbb{Z}_{\leqslant K}$. That is,

$$S_n \leqslant s_n[k], \qquad k \in \mathbb{Z}_{\geqslant K_n}. \tag{5.11}$$

Next, recall that the individual charging rates $\pi_n[k]$ are coupled to temperature dynamics (5.6) and constraint (5.9) through the relation

$$\pi[k] = \sum_{n\in\mathcal{N}} \pi_n[k], \qquad k \in \mathbb{Z}_+. \tag{5.12}$$

The set of solutions $\{\boldsymbol{\pi}_n\}_{n\in\mathcal{N}}$ to (5.6)–(5.12) given $\Delta T[k]$, $\{s_n[k]\}_{n\in\mathcal{N}}$ and $\mathbf{d}[k]$ is the set of valid charging/feasible control strategies. Note that this set is polytopic (and thus convex), as all constraints (5.6)–(5.12) are affine in $\boldsymbol{\pi}_n$.

The selection of a particular control schedule out of the set of feasible strategies may be based on an optimization criterion. In our work, a PEV-centric objective is employed, namely, the minimization of SOC deviations from 1 and minimization of local battery wear and control effort. Thus, the centralized controller's composite objective is

$$\min_{\boldsymbol{\pi}_n[k],\mathbf{s}_n[k],n\in\mathcal{N}} \sum_{n\in\mathcal{N}} J_n(\boldsymbol{\pi}_n[k], \mathbf{s}_n[k]) \tag{5.13}$$

where $J_n : \mathbb{R}^K \times \mathbb{R}^{K+1} \to \mathbb{R}_+$, $n \in \mathcal{N}$, is defined as

$$J_n(\boldsymbol{\pi}_n, \mathbf{s}_n) := \boldsymbol{\pi}_n^\top \mathcal{R}_n \boldsymbol{\pi}_n + (\mathbf{s}_n - \mathbf{1}_{K+1})^\top \mathcal{Q}_{s,n}(\mathbf{s}_n - \mathbf{1}_{K+1}),$$

with $\mathcal{Q}_{s,n} = Q_{s,n}\mathbf{I}_{K+1}$ and $\mathcal{R}_n = R_n\mathbf{I}_K$, for some $Q_{s,n}, R_n \in \mathbb{R}_{>0}$. Since both $Q_{s,n}$ and R_n are strictly positive and constraints (5.6)–(5.12) are linear, the optimization problem obtained by solving (5.13) over the set of feasible control strategies is strictly convex and any optimal solution is therefore globally optimal.

Now consider the following optimization problem.

Problem V.1 (Open-loop Centralized PEV Charging). Given $s_n[0 \mid k] = s_n[k]$ for $n \in \mathcal{N}$, $\Delta T[0 \mid k] = \Delta T[k]$ and disturbance forecast $\hat{\mathbf{d}}[k] := \mathrm{col}\left(\{\hat{d}[l \mid k]\}_{l\in\mathbb{Z}_{[0,K-1]}}\right)$, solve

$$\min_{\boldsymbol{\pi}_n,\, n\in\mathcal{N}} \sum_{n\in\mathcal{N}} \left(\boldsymbol{\pi}_n^\top (\boldsymbol{\Psi}_{S_n}^\top \mathcal{Q}_{s,n} \boldsymbol{\Psi}_{S_n} + \mathcal{R}_n)\boldsymbol{\pi}_n \right. \tag{5.14a}$$

$$\left. + 2(\boldsymbol{\Phi}_{S_n}\mathbf{s}_n[0 \mid k] - \mathbf{1}_{K+1})^\top \mathcal{Q}_{s,n}\boldsymbol{\Psi}_{S_n}\boldsymbol{\pi}_n \right)$$

$$\text{s.t. } \boldsymbol{\Phi}\Delta T[0 \mid k] + \boldsymbol{\Psi}\left(\sum_{n\in\mathcal{N}} \boldsymbol{\pi}_n\right) + \boldsymbol{\Psi}_{\mathrm{d}}\hat{\mathbf{d}} \leqslant T_{\max}\mathbf{1}_{K+1} \tag{5.14b}$$

$$\pi_{n,\min}\mathbf{1}_K \leqslant \boldsymbol{\pi}_n \leqslant \pi_{n,\max}\mathbf{1}_K \tag{5.14c}$$

$$0 \leqslant \boldsymbol{\Phi}_{S_n}s_n[0 \mid k] + \boldsymbol{\Psi}_{S_n}\boldsymbol{\pi}_n \leqslant \mathbf{1}_{K+1} \tag{5.14d}$$

$$S_n\mathbf{1}_{K-K_n+1} \leqslant \mathbf{M}_{K_n}\left(\boldsymbol{\Phi}_{S_n}s_n[0 \mid k] + \boldsymbol{\Psi}_{S_n}\boldsymbol{\pi}_n\right) \tag{5.14e}$$

for all $n \in \mathcal{N}$, where $\mathbf{M}_{K_n} \in \mathbb{R}^{(K-K_n+1)\times(K+1)}$ is such that $\mathbf{M}_{K_n}\mathbf{s}_n[k] = \mathrm{col}\left(\{s_n[l \mid k]\}_{l\in\mathbb{Z}_{[K_n,K]}}\right)$. ∎

In what follows, we refer to Prob. V.1 as the *primal load scheduling problem*. It is obtained by reformulating constraints (5.9)–(5.11) and objective (5.13) in terms of

control sequences $\boldsymbol{\pi}_n[k]$ only. This is achieved by eliminating state predictions $\mathbf{T}_n[k]$ and $\mathbf{s}_n[k]$ using (5.6)–(5.7) and (5.12).

5.5 Incentive-based Coordinated Charging

In what follows, we derive an iterative, price-coordinated implementation of Problem V.1. Close inspection of (5.14) reveals that except for the complicating temperature constraint, i.e., (5.14b), the centralized charging problem is fully separable in local control sequences $\boldsymbol{\pi}_n$. Thus, if it was not for the temperature constraint that couples the profiles $\boldsymbol{\pi}_n$ for all $n \in \mathcal{N}$, it would be possible to find the optimizer of Prob. V.1 by solving, in parallel, a set of N local PEV-specific optimization problems in $\boldsymbol{\pi}_n$. To derive a non-centralized implementation while still accounting for the coupling temperature constraint, consider the partial dual of Prob. V.1 obtained by relaxing (5.14b), i.e.,

$$\max_{\boldsymbol{\lambda} \in \mathbb{R}_+^{K+1}} \Upsilon(\boldsymbol{\lambda}) \tag{5.15}$$

where

$$\Upsilon(\boldsymbol{\lambda}) := \min_{\boldsymbol{\pi}_n \in \Pi_n\left(s_n[0|k]\right)} \sum_{n \in \mathcal{N}} \left(\hat{J}_n(\boldsymbol{\pi}_n) + \boldsymbol{\lambda}^\top \boldsymbol{\Psi} \boldsymbol{\pi}_n\right) + \boldsymbol{\lambda}^\top \left(\boldsymbol{\Phi} \Delta T[0|k] + \boldsymbol{\Psi}_\mathrm{d} \hat{\mathbf{d}} - T_{\max} \mathbf{1}_{K+1}\right),$$

with $\Pi_n\left(s_n[0|k]\right) := \{\boldsymbol{\pi}_n \in \mathbb{R}^K \mid (5.14c)\text{–}(5.14e) \text{ holds}\}$,

$$\hat{J}_n(\boldsymbol{\pi}_n) := \boldsymbol{\pi}_n^\top (\boldsymbol{\Psi}_{S_n}^\top \mathcal{Q}_{s,n} \boldsymbol{\Psi}_{S_n} + \mathcal{R}_n)\boldsymbol{\pi}_n + 2(\boldsymbol{\Phi}_{S_n} s_n[0|k] - \mathbf{1}_{K+1})^\top \mathcal{Q}_{s,n} \boldsymbol{\Psi}_{S_n} \boldsymbol{\pi}_n,$$

and where $\boldsymbol{\lambda} \in \mathbb{R}_+^{K+1}$ is the Lagrangian multiplier or *pseudo-price vector* associated with constraint (5.14b), see [99].

A well-known decomposition technique from convex optimization, the dual-ascent method, can now be applied to solve Prob. V.1 in a distributed way, see [100, 99]. The underlying observation is that $\Upsilon(\boldsymbol{\lambda})$ allows for separate optimization over $\boldsymbol{\pi}_n, n \in \mathcal{N}$, yielding the following problem.

Problem V.2 (Open-loop Coordinated PEV Charging). At iteration $p \in \mathbb{Z}_+$, given $s_n[0 \mid k] = s_n[k]$, $\Delta T[0 \mid k] = \Delta T[k]$, disturbance forecast $\hat{\mathbf{d}}[k]$ and price vector $\boldsymbol{\lambda}^{(p)}[k] \in \mathbb{R}_+^{K+1}$, solve for each PEV $n \in \mathcal{N}$,

$$\boldsymbol{\pi}_n^{(p)}[k] = \underset{\boldsymbol{\pi}_n \in \Pi_n\left(s_n[0|k]\right)}{\arg\min} \hat{J}_n\left(\boldsymbol{\pi}_n\right) + \left(\boldsymbol{\lambda}^{(p)}[k]\right)^\top \boldsymbol{\Psi} \boldsymbol{\pi}_n. \tag{5.16}$$

Then, given initial price $\boldsymbol{\lambda}^{(0)}[k]$, generate $\boldsymbol{\lambda}^{(p+1)}[k]$ via

$$\boldsymbol{\lambda}^{(p+1)}[k] = \left[\boldsymbol{\lambda}^{(p)}[k] + \alpha^{(p)} \left(\nabla_{\boldsymbol{\lambda}} \Upsilon\right)\right]_+, \tag{5.17}$$

with

$$\nabla_{\boldsymbol{\lambda}} \Upsilon := \boldsymbol{\Phi} \Delta T[0 \mid k] + \boldsymbol{\Psi} \left(\sum_{n \in \mathcal{N}} \boldsymbol{\pi}_n^{(p)}[k] \right) + \boldsymbol{\Psi}_{\mathrm{d}} \hat{\mathbf{d}}[k] - T_{\max} \mathbf{1}_{K+1}$$

and iteration-dependent step-size parameter $\alpha^{(p)} \in \mathbb{R}_+$. ∎

Prob. V.2 can be interpreted as follows, see Fig. 5.2. To decentralize Prob. V.1, we employ a centralized coordinator that is responsible for secure transformer operation, and that supplies the vehicles with a common time-varying pseudo-price for electrical energy, i.e., $\boldsymbol{\lambda}^{(p)}$ [\$/J]. Each PEV owner can respond autonomously to this price. In accordance with (5.16), rational car owners will adjust their scheduled power demand in a way that complies with their local constraints and minimizes the sum of local objectives (i.e., $\hat{J}_n(\boldsymbol{\pi}_n)$) and energy costs (i.e., $\left(\boldsymbol{\lambda}^{(p)}\right)^\top \boldsymbol{\Psi} \boldsymbol{\pi}_n$). The coordinator is informed about the individual optimal power profiles $\boldsymbol{\pi}_n^{(p)}$ and updates the price in a way that supports feasibility of temperature constraint (5.14b) at iteration $p + 1$. More specifically, the corresponding *master problem*, i.e., maximizing over $\boldsymbol{\lambda}$ in (5.15), is solved via the *projected subgradient method* using (5.17). Accordingly, the price is driven towards zero at time instants for which the temperature associated with the profiles $\boldsymbol{\pi}_n^{(p)}$ is predicted to be below $T_{\max}$. However, the price is increased, and thus, charging is discouraged, at instants for which the demand response $\sum_{n \in \mathcal{N}} \boldsymbol{\pi}_n^{(p)}$ would lead to a violation of constraint (5.9).

Now consider the following theorem.

Theorem V.3. *Let $\{\alpha^{(p)}\}_{p \in \mathbb{Z}_+}$ with $\alpha^{(p)} \in \mathbb{R}_+$ for $p \in \mathbb{Z}_+$ be such that $\sum_{p=0}^{\infty} \alpha^{(p)} = \infty$ and $\sum_{p=0}^{\infty} \left(\alpha^{(p)}\right)^2 < \infty$. Then the profiles $\boldsymbol{\pi}_n^{(p)}$, $n \in \mathcal{N}$, generated by Prob. V.2 asymptotically converge to the optimizers $\boldsymbol{\pi}_n^*$ of Prob. V.1, i.e., $\|\boldsymbol{\pi}_n^{(p)} - \boldsymbol{\pi}_n^*\|_2 \to 0$ for $p \to \infty$.*

The above result can be obtained along the following lines. For the above conditions on the step-size sequence $\{\alpha^{(p)}\}_{p \in \mathbb{Z}_+}$, the iterates generated by projected subgradient step (5.17) are guaranteed to converge asymptotically to the optimizer $\boldsymbol{\lambda}^*$ of (5.15), see [100, 99]. Thus, Prob. V.2 asymptotically recovers the optimal Lagrangian multiplier associated with complicating constraint (5.14b) in Prob. V.1. The result now follows from strong duality of Prob. V.1.

In conclusion, we have obtained a distributed implementation of Prob. V.2 that allows for autonomous decision making of individual PEV owners based on a common pseudo-price signal. Next, we describe how this incentive-based scheduling problem can be embedded in a model predictive control scheme as a means to provide feedback to disturbances and changing network conditions.

5.5.1 Implementation: receding horizon control

The previously defined PEV-load scheduling schemes, i.e., Prob. V.1 and Prob. V.2, compute an optimal charging profile given a single state measurement and disturbance forecast. Such approaches are only effective if the future temperature and SOC values can be predicted with high accuracy. Although net inelastic demand can be predicted

relatively well on the transmission-network level (in an empirical fashion), unexpected fluctuations in background demand can be significant in distribution networks due to a low extent of aggregation. Moreover, for a PEV-load control scheme to be useful, it should allow for varying numbers of connected cars during the charging period. Thus, in practice, it is difficult to avoid significant prediction errors over a long horizon K using open-loop scheduling only. However, we can introduce feedback as a solution to unexpected disturbances, modeling errors and changing numbers of PEVs, by running Probs. V.2 and V.1 in a receding horizon fashion. This yields a predictive control law that solves the PEV-load scheduling problem each sampling time, while taking a new state measurement and disturbance forecast into account. At each instant $k \in \mathbb{Z}_+$, the first sample of the last obtained control sequences $\boldsymbol{\pi}_n^{(p)}[k]$ is applied to the system, before running the procedure again at time instant $k+1$. This procedure is summarized below.

Algorithm V.4. *At each time instant $k \in \mathbb{Z}_+$:*
1: *Obtain SOC $s_n[k]$ (PEV controller n), temperature $\Delta T[k]$ and disturbance forecast $\hat{\mathbf{d}}[k]$ (coordinator);*
2: *Initialize $\boldsymbol{\lambda}^{(0)}[k]$ and run Prob. V.2 for $p_{\max}$ iterations;*
3: *Vehicle n charges its battery at a rate of $\pi_n^{(p_{\max})}[0 \mid k]$.* ∎

Fig. 5.2 depicts the control/communication architecture associated with Alg. V.4. Red lines represent exchange of information; measurements and physical inputs are reflected by black lines. The coordinator performs both price update (5.17) and disturbance estimation, whereas PEV behavior is determined by charging laws (5.16) and SOC dynamics (5.2).

In general, there is no guarantee that the iterates $\boldsymbol{\pi}_n^{(p)}$ generated by Prob. V.2 will be feasible for $p < \infty$. However, in practice, it may still be possible to obtain a feasible (yet, not necessarily optimal) set of PEV charging schedules within a finite number of iterations. In what follows, we assume that $p_{\max} < \infty$ iterations are sufficient for this to occur. Then, for Alg. V.4 to be suited for implementation in practice, it is necessary that the time required for evaluating these iterations does not exceed the sampling period T_s.

Simulation results (see Sect. 5.6) indicate that the number of iterations required for obtaining feasible control actions may be reduced by appropriately choosing the sequence $\{\alpha^{(p)}\}_{p \in \mathbb{Z}_+}$. Also, convergence speed may be increased considerably in case of small prediction errors, by initializing $\boldsymbol{\lambda}^{(0)}[k] = \{\lambda^{(0)}[l \mid k]\}_{l \in \mathbb{Z}_{[0,K]}}$ as a time-shifted version of the previous price $\boldsymbol{\lambda}^{(p_{\max})}[k-1]$, i.e., $\lambda^{(0)}[l \mid k] := \lambda^{(p_{\max})}[l+1 \mid k-1]$, $l \in \mathbb{Z}_{[0,K-1]}$, and random $\lambda^{(0)}[K \mid k] \in \mathbb{R}_+$, for $k \in \mathbb{Z}_{\geqslant 1}$. Yet, to the best of our knowledge, general results on the convergence rate of dual-ascent based optimization schemes are lacking still.

Also, note that evaluation of the PEV-specific quadratic programming problems (5.16) can be implemented efficiently, using, e.g., interior-point techniques. A more relevant obstacle for real-time implementation may be posed by the PEV–coordinator communication network, which needs to allow for both secure and reliable bidirectional data transmission.
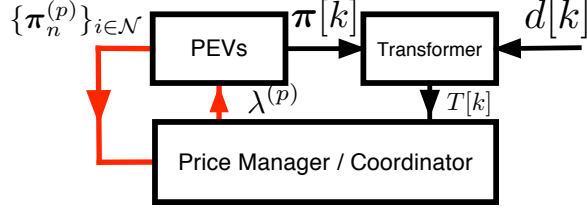
Figure 5.2: Control/communication architecture of coordinated PEV control.

Remark V.5. In Alg. V.4, Prob. V.2 is run for $p_{\max}$ iterations each sampling instant. To avoid superfluous computations and reduce the extent of communication between the vehicles and the coordinator, it may be attractive to stop iterating earlier, based on some convergence test criterion. For example, if the convergence of $\boldsymbol{\lambda}^{(p)}$ is monotonic and super-linear, sufficiently accurate approximation of $\boldsymbol{\lambda}^*$ can be concluded if $\|\boldsymbol{\lambda}^{(p)} - \boldsymbol{\lambda}^{(p-1)}\| < \varepsilon$ for a small $\varepsilon \in \mathbb{R}_+$.

Although the receding-horizon feedback mechanism in Alg. V.4 helps to reduce the effects of prediction inaccuracy, robust feasibility can only be guaranteed if some uncertainty model is explicitly accounted for during open-loop scheduling, i.e., in Prob. V.1 or Prob. V.2. In what follows, we assume that the background demand and ambient temperature can be predicted up to a certain accuracy, that is, $d[l+k] = \hat{d}[l \mid k] + \delta[l+k]$, with arbitrary, unknown $\delta[l+k] \in \Delta \subset \mathbb{R}^2$. One way of establishing robust feasibility of Prob. V.1 with respect to inaccuracies δ in the (compact) set Δ, consists of replacing (5.14b) by the constraint

$$\boldsymbol{\Phi}\Delta T[0 \mid k] + \boldsymbol{\Psi}\left(\sum_{n \in \mathcal{N}} \boldsymbol{\pi}_n\right) + \boldsymbol{\Psi}_{\mathrm{d}}\hat{\mathbf{d}} + \begin{bmatrix} \max_{\boldsymbol{\delta} \in \Delta^K}[\boldsymbol{\Psi}_{\mathrm{d}}\boldsymbol{\delta}]_1 \\ \vdots \\ \max_{\boldsymbol{\delta} \in \Delta^K}[\boldsymbol{\Psi}_{\mathrm{d}}\boldsymbol{\delta}]_{K+1} \end{bmatrix} \leqslant T_{\max}\mathbf{1}_{K+1}, \qquad (5.18)$$

A similar worst-case feasibility approach can be employed in Prob. V.2, by appropriate modification of $\nabla_{\boldsymbol{\lambda}}\Upsilon$ in (5.17).

5.6 Case Study: Overnight PEV Charging

Next, we simulate the charging of $N = 20$ PEVs during an overnight period from 20:00h (i.e., $t = 0\,\mathrm{s}$) to 8:00h given by the centralized and distributed PEV demand control schemes defined by Prob. V.1 and Prob. V.2 to test their effectiveness in terms of satisfying the temperature and SOC constraints, as well as to compare their performance for a realistic charging scenario. Table 5.1 summarizes the simulation scenario, where the bracket notation $[a, b]$, denotes randomly distributed values over the interval $\mathbb{R}_{[a,b]}$. The PEV fleet is heterogeneous in terms of cost parameter values R_n and $Q_{s,n}$, battery parameters η_n and charging rate limits $\pi_{n,\max}$; the latter two were selected to resemble those of today's PEVs. The ambient temperature T_{a} is constant and representative for a hot summer night. The employed SOC and charging penalties are constant, except for a factor 10 increase in R_n after time K_n. This reflects that PEV owners prefer to charge quickly early in the evening. The background load $i_{\mathrm{d}}[k]$,

Table 5.1: Simulation parameters for PEV case study

Parameter	Value	Unit
Sampling Time, T_s	155	s
Temperature limit, $T_{\max} + T^*$	393	K
Ambient temperature, $T_a[k]$	303	K
Initial temperature, $T[0]$	333	K
Transformer parameters, τ, γ, ρ	0.9, 0.1, 0.85	-, -, K/A
Battery parameter, η_n	[0.47, 0.75]	1/kA
Current bounds, $\pi_{n,\min}, \pi_{n,\max}$	0, [10, 20]	A
Initial SOC, $s_n[0]$	[0, 0.2]	-
Required minimum SOC, S_n	[0.8 1.0]	-
Required minimum SOC time, K_n	[4:00, 8:00]	hr:min
Initial control input penalty, R_n	[0.05, 0.10]	-
State penalty, $Q_{s,n}$	[10, 20]	-
Dual-ascent step-size parameter, $\alpha^{(p)}$	$2/\lceil p/3 \rceil$	1 / K
Iterations per time instant, $p_{\max}[k]$	150 to 20	iterations

see Fig. 5.3c, is representative for the nightly power demand of 100 households (i.e. total inflexible load is 45kW to 60kW). Finally, note that the sequence $\alpha^{(p)}$ satisfies the conditions of Thm. V.3.

We evaluated the performance of Prob. V.1 and Prob. V.2 in closed-loop with the *linearized* system characterized by Table 5.1 and (5.2), (5.5). Additionally, we simulated uncoordinated charging by evaluating Prob. V.2 for an all-zero price signal, i.e., $\boldsymbol{\lambda}^{(p)}[k] = \{0, \ldots, 0\}$, for all $k, p \in \mathbb{Z}_+$. All schemes were implemented in a receding horizon fashion, using a 12-hour prediction horizon at time instants between 20:00h and 22:00h, and a shrinking horizon with a fixed end-point at 10:00h at time instants after 22:00h. The coordinator was provided with a perfect forecast of $T_a[t]$ and a $\pm 5\%$ uncertain forecast of demand $i_d[k]$, i.e., $i_d[l + k] = \hat{i}_d[l \mid k] + \delta_i[l + k]$ with $\delta_i[k] \in \Delta_i[k] := \mathbb{R}_{[-0.05\hat{i}_d[k], 0.05\hat{i}_d[k]]}$. Persistent feasibility was ensured via temperature constraint (5.18).

Fig. 5.3 shows the simulation results for the three charging schemes. Clearly, the uncoordinated method performs poorly, since, without the price signal, the PEVs are not affected by the temperature constraint and thus charge rapidly, taking only their own SOC requirements and objectives into account (Fig. 5.3b). Consequently, the temperature exceeds $T_{\max}$ for over 3 hours, which could result in transformer failure.

In contrast to uncoordinated charging, both Prob. V.1 and Prob. V.2 respected temperature constraint (5.9). Note that the uncertainty margin employed in (5.18) caused a performance degradation of less than two degrees Kelvin as compared to the noise-free centralized scheme. Also, observe that the noisy coordinated incentive-based scheme and the noisy centralized scheme induce only slightly different current and temperature trajectories, despite $p_{\max}$ being finite.

118

Because the employed cost functions (5.13) (and, equivalently, (5.16)) heavily penalize non-fully charged batteries early in the evening, PEV owners attempt to charge as quickly as possible. Fig. 5.3a shows that as a result, the temperature reaches $T_{\max}$ as soon as ca. 20:30h. In response to this, the coordinator increases the price to suppress charging (Fig. 5.4), and thus, overloading is prevented. In response to the decrease in price that occurs from 21:00h to 23:30h, the PEV charging current increases again. After 00:00h, the increased penalty on control effort comes with a reduced priority for rapid charging, causing the average charging rate to decrease slightly. Combined with low inelastic demand, this causes the transformer temperature to drop below $T_{\max}$, and thus, the optimal price $\lambda^*[k]$ is driven to zero (in accordance with complementary slackness of the optimal Lagrangian multiplier [99]). For the remainder of the night, the network offers plenty of charging capacity and the PEV owners can charge freely, unhindered by a non-zero price, to reach their SOC target while minimizing their local objectives.

Moreover, even though we employed finite $p_{\max}$ and a $\pm 5\%$ uncertain load forecast, the incentive-based control scheme performed nearly optimal and was feasible with respect to constraints (5.8)-(5.11) at all simulated time instants.

5.7 Summary

Simultaneous overnight charging of plug-in electric vehicles (PEVs) may cause severe overloading of substation transformers in the near future. A distributed incentive-based demand-scheduling problem was derived as a solution to this issue, based on a dynamical model of a small PEV fleet that is served by a single temperature-constrained transformer. Feedback to disturbances was provided by evaluating the open-loop scheduling problem in a receding horizon fashion, yielding an iterative model predictive control (MPC) scheme in which the individual PEVs can autonomously respond to incentives provided by a coordinator that is responsible for secure transformer operation. Simulation results showed that even for a finite number of iterations, the method can be effective in terms of enforcing the temperature constraint.
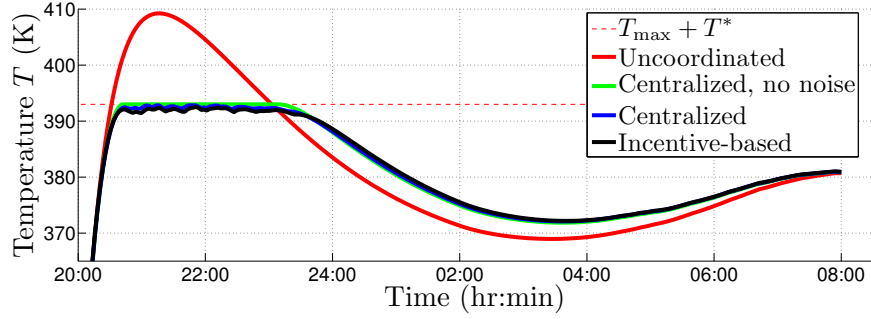
(a) Transformer temperature $T[k]$.
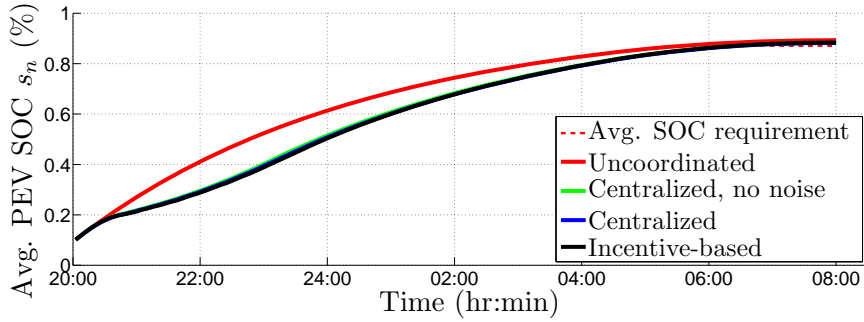
(b) Average SOC target $avg(S_n)$ and profiles $avg(s_n[k])$.
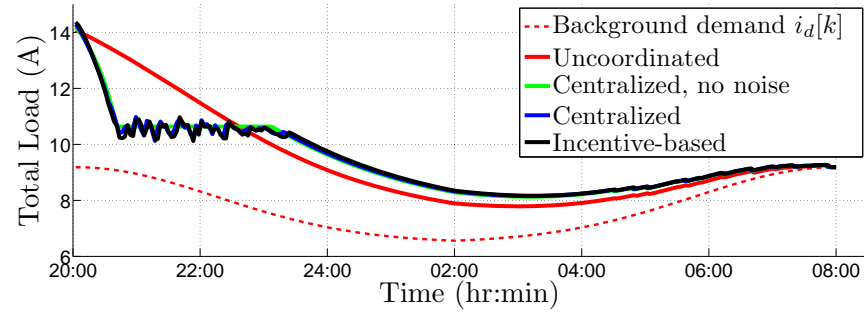
(c) Aggregated transformer current $\pi[k] + i_{\mathrm{d}}[k]$.
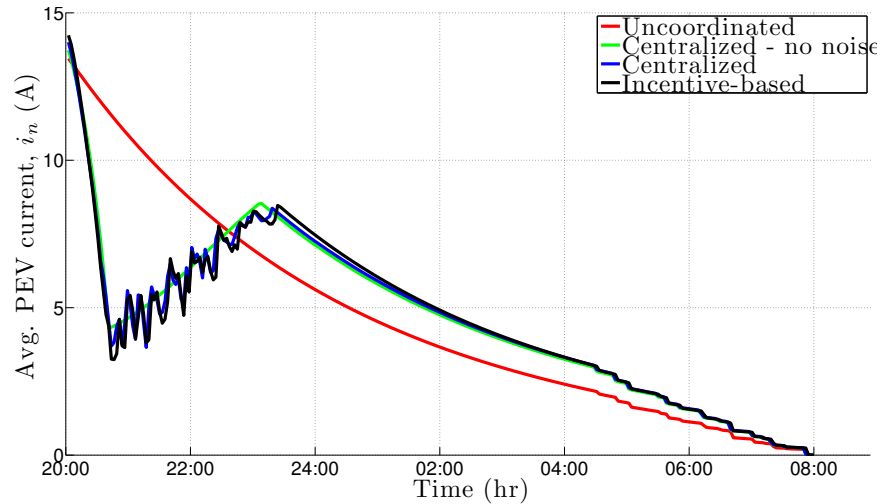
(d) Averaged charging current $\sum_{n \in \mathcal{N}} \pi_n / N$.

Figure 5.3: Performance of Prob. V.1, Prob. V.2, and uncoordinated charging.
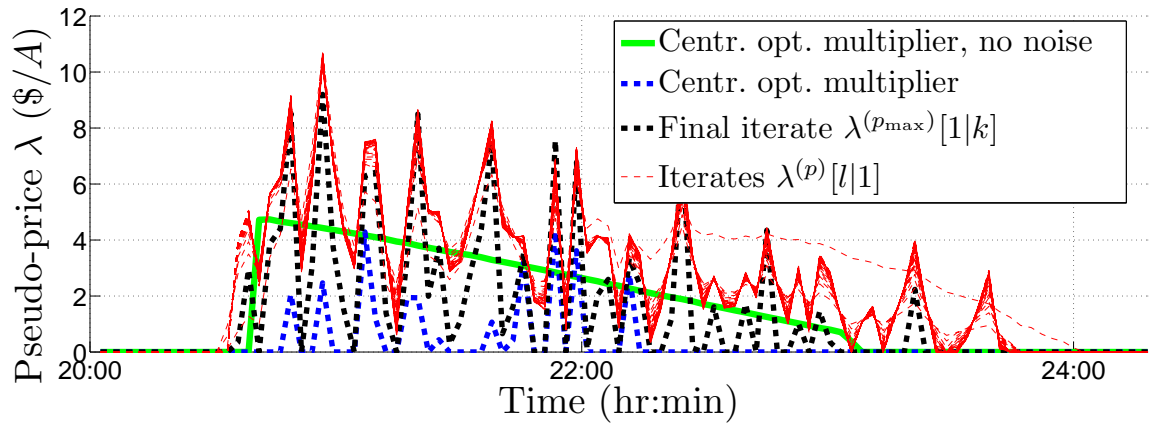
Figure 5.4: Convergence of the incentive-based charging scheme for $k = 0$.

CHAPTER VI

Conclusions and Future Work

6.1   Conclusions

Due to the protracted and cost-intensive nature of upgrading energy infrastructures, power systems are today operating closer and closer to their limits. The research presented herein brings together ideas from power systems, optimization, and control theory to improve the utility of existing and future energy infrastructures. Specifically, this dissertation proposes practical, yet rigorously justified solutions that mitigate the effects of overloads in power systems. Chapter I provides a general introduction to the research area of the dissertation and surveys the relevant literature.

There are signs that co-generation (i.e. the recovery of previously wasted heat) is on the rise in central energy plant settings, such as universities. These venues provide a starting point for the application of energy hub ideas and the tools developed in Chapter III allow for quick analysis of arbitrary energy hub systems under relatively mild assumptions. In addition, the formulation developed for energy hub systems is linear (and convex), which enables computationally tractable and globally optimal solutions to multi-energy system problems.

The electric grid today is operated to ensure safety from common and predicted disturbances, but it is only ad-hoc safety guidelines and human grid operators that stand between cascade failures and consumers. As experienced in 2003, this is not always enough of a safety guarantee and the human and economic costs can be severe. This is why there is a need to consider automated and verifiable methods to minimize the impact of disturbances. Within this context, Chapter IV develops a bilevel model-predictive emergency control scheme to mitigate the effect of cascading failures. The centralized linear receding-horizon MPC (RHMPC) cascade mitigation scheme developed in Section 4.5 incorporates a simple but sufficient model of an electric transmission system into an MPC formulation and considers the system response on a fast minute-by-minute timescale. Importantly, the RHMPC scheme combines and balances economic and security objectives and is shown to significantly improve system reliability by leveraging the temporal nature of storage and conductor temperatures.

Simultaneous overnight charging of plug-in electric vehicles (PEVs) may cause severe overloading of substation transformers in the near future. In Chapter V, a

non-centralized incentive-based demand-scheduling problem is derived as a solution to this issue, based on a dynamical model of a small PEV fleet that is served by a single temperature-constrained transformer. The solution is obtained with an iterative MPC scheme in which the individual PEVs can autonomously respond to incentives provided by a coordinator that is responsible for secure transformer operation.

In this work, the problems addressed and the main results are as follows.

- A strictly linear formulation of the energy hub model is derived that is consistent with the nonlinear models developed in literature. Then, a concise ASCII-based format and a set of Matlab tools are developed, which allow for seamless simulation, optimization, and analysis of multi-systems with more than 100 energy hubs. This allows users to answer questions about the economical role of renewables and energy storage in a multi-energy setting, such as a university campus or military base.

- The SHMPC cascade mitigation scheme is developed for multi-energy systems that highlights the importance of energy storage and balancing of economic and security constraints in power systems. Specifically, it is shown that without coupling economic and security objectives, an automated cascade mitigation scheme may become too greedy and place the system in a worse position long-term.

- The RHMPC cascade mitigation solution is provided for electric power systems, which alleviates temperature overloads on transmission lines and prevents cascade failures. The scheme uses a simple, but sufficient, model of the system and balances economic and security constraints. Using a case-study of a standard IEEE test system, it is shown that the RHMPC scheme can mitigate the effect of severe disturbances and return the system to economically optimal set points under uncertainty and significant model inaccuracies.

- A convex relaxation of AC line losses is derived and proven to be tight for the RHMPC scheme when line temperatures exceed their limit, which enable alleviation of line overloads. The relaxation provides a superior approximation of losses in an AC transmission system compared with standard Taylor approximations and is not subject to any limiting LMP or network topology assumptions as is often the case in literature.

- A non-centralized incentive-based robust MPC scheme is developed for preventing distribution-level transformer overloads. The scheme employs distributed load control of PEVs and a centralized coordinator to balance the objectives of the PEVs subject to network constraints. To achieve this overload prevention scheme, the dual ascent algorithm is applied. Simulations highlight that even with finite iteration limits enforced, the performance of the scheme is near-optimal and overload is prevented robustly.

6.2 Future Work

The following challenging tasks and interesting ideas represent future work emanating from this dissertaton:

- In the area of energy hubs:

  - While Hubert is useful to us, it needs to be groomed a bit to become useful to others. That is, with some time and effort, the energy hub tools we call Hubert could become an open-source toolbox enabling users to quickly model, simulate, optimize, and analyze multi-energy systems.

  - The concise ASCII-based format presented herein somewhat lacks modeling flexibility. That is, there are multi-energy systems which are not readily captured by the proposed format. This presents challenges for applying the tools in specialized industrial settings.

  - Energy hubs are known for their simplicity, but when it comes to modeling conversion processes they might be too simple. Therefore, development of an improved energy hub, which captures nonlinear/non-constant conversion efficiencies would be valuable. One approach would be to consider piece-wise affine efficiency curves, which introduces integer variables.

- In the area of receding-horizon cascade mitigation:

  - The balancing of multiple MPC objectives was performed manually in this work. However, multi-objective MPC, in a general setting, requires a method for automatically tuning the Q and R weighting matrices to achieve desired balance between security and economic performance. In a sense, economical and security objectives are competing objectives but methods, such as economic [101] and utopia-tracking [102] MPC may be particularly useful in describing performance and stability.

  - The PWL relaxation of line losses is only tight for overloaded lines. Therefore, lines that are not overloaded can attain any relaxed value and, thus, there is no unique optimal mapping between the algebraic states and dynamic states and control inputs. This prevents us from writing RHMPC in standard form: $x[k+1] = Ax[k] + Bu[k]$, which complicates technical verification of the scheme. As a result, there is value in developing MPC results for systems such as this, with the "origin" (i.e. equilibrium point) defined by a subspace of the algebraic states.

  - Non-centralized (i.e. distributed) MPC for cascade mitigation in power systems represents a natural and immediate extension of this work. Non-centralized schemes are motivated by the multi-agent nature of power systems, and the computational requirements for solving large-scale power system problems. However, a less obvious but more interesting motivation arises from the physical nature of power systems. Specifically, the immediate effects of a disturbance are generally localized, with more widespread

consequences evolving over a longer time-frame. This implies an opportunity for adapting the (potentially overlapping) control areas based on sensitivities and the nature of contingencies, see [103].

– The DC power flow model used in the MPC development does not consider voltage magnitudes (nor reactive power). There is value in being able to include voltage information in a linear/convex MPC scheme as that would facilitate protection against voltage collapse. To accomplish this, convex relaxations and cutting planes will be explored in the future.

– The proposed control scheme provides a basis for considering enhanced roles for energy storage, and for addressing questions regarding optimal siting and sizing as a function of economic and security objectives.

– The performance of the RHMPC scheme under uncertainty should be analyzed subject to different scenarios. In particular, the cyber-coupling of the RHMPC scheme with state estimators and PMUs would provide insight into future implementation of scheme. In addition, due to the role of information in the scheme, development of control policies that consider resource-constrained adversaries would be very interesting.

• In the area of distributed charging control of PEVs:

– In real-time implementation, it is key that the PEV coordination scheme can generate feasible control actions within each sampling period. Since the incentive-based charging control method relies on an iterative scheme, it is important, for the purpose of implementation, to ensure fast convergence. Therefore, it becomes valuable to improve the notoriously slow convergence rate of dual ascent method, which is used in the iterative scheduling problem, or replace it with other alternative non-centralized implementations that may exhibit faster convergence.

– A linearized current-based thermal model for transformer heating is employed in this problem. Using the quadratic current-based model is preferred but requires reformulation of our MPC and is not immediately well suited for dual decomposition. Employing a convex relaxation similarly to the PWL relaxation of AC line losses seems promising.

– The current setup assumes perfect communication between coordinator and PEVs. However, under imperfect or adversarial communication network assumptions, it would be interesting to investigate how uncertainty and noise (e.g. faulty price signals sent to a few vehicles) affect convergence of the dual ascent method.

– Lastly, a comprehensive experimental validation of the scheme is important.

The solutions to these challenging and interesting problems will provide practical, but rigorously justified solutions to real-world problems and be of interest to both local utilities and ISOs.

APPENDICES

APPENDIX A

Karush-Kuhn-Tucker Necessary Conditions

Given a general (not necessarily convex) mathematical program, $\mathcal{P}$:

$$(\mathcal{P}) \quad \begin{array}{ll} \max_x & f(x) \\ \text{s. t.} & h(x) = b \in \mathbb{R}^l \\ & g(x) \leqslant d \in \mathbb{R}^m \\ & x \in \mathcal{X} \subset \mathbb{R}^n, \end{array} \tag{A.1}$$

where $f(x) : \mathbb{R}^n \to \mathbb{R}$, $h(x) : \mathbb{R}^n \to \mathbb{R}^l$, and $g(x) : \mathbb{R}^n \to \mathbb{R}^m$ are continuously differentiable functions. The Lagrangian $\mathcal{L} : \mathbb{R}^{n+m+l} \to \mathbb{R}$ is defined as follows:

$$\mathcal{L}(x; \lambda, \mu) = f(x) + \lambda^\top (h(x) - b) + \mu^\top (g(x) - d), \tag{A.2}$$

where $\mu \in \mathbb{R}^m, \lambda \in \mathbb{R}^l$ denote the KKT multipliers. Let $x^* \in \mathbb{R}^n$ represent a feasible (locally) optimal solution to $\mathcal{P}$ that satisfies a constraint qualification (see [104]). Then, the Lagrangian must satisfy the following KKT first-order necessary optimality conditions:

$$\nabla \mathcal{L}(x^*; \lambda, \mu) = \nabla f(x^*) + J_h(x^*)^\top \lambda + J_g(x^*)^\top \mu = 0 \tag{A.3}$$

$$\mu \cdot (g(x^*) - d) = 0 \tag{A.4}$$

$$\mu \geqslant 0 \tag{A.5}$$

where $(.)^\top$ is the matrix transpose and $J_y(x) \in \mathbb{R}^{p \times n}$ denotes the Jacobian and has the following structure of partial derivatives:

$$J_y(x) = \begin{bmatrix} \frac{\partial y_1}{\partial x_1} & \frac{\partial y_1}{\partial x_2} & \cdots & \frac{\partial y_1}{\partial x_n} \\ \frac{\partial y_2}{\partial x_1} & \frac{\partial y_2}{\partial x_2} & \cdots & \frac{\partial y_2}{\partial x_n} \\ \vdots & \vdots & \ddots & \vdots \\ \frac{\partial y_p}{\partial x_1} & \frac{\partial y_p}{\partial x_2} & \cdots & \frac{\partial y_p}{\partial x_n} \end{bmatrix} \implies J_y(x) = \begin{bmatrix} \nabla y_1^\top(x) \\ \nabla y_2^\top(x) \\ \vdots \\ \nabla y_p^\top(x) \end{bmatrix}. \tag{A.6}$$

Thus, from (A.3), we have that for each variable x_i, where $x = [x_1, \ldots, x_n]^\top$, the following must hold:

$$0 = \left.\frac{\partial f}{\partial x_i}\right|_{x_i = x_i^*} + \sum_j^l \lambda_j \left.\frac{\partial h_j}{\partial x_i}\right|_{x_i = x_i^*} + \sum_j^m \mu_j \left.\frac{\partial g_j}{\partial x_i}\right|_{x_i = x_i^*} \qquad \forall i = 1, 2, \ldots, n. \qquad \text{(A.7)}$$

If $m = 0$ (i.e. no inequality constraints), then λ is denoted the Lagrange multiplier. Geometrically, one can view the KKT constraints by considering only inequality constraints (i.e. $h(x) = b$ becomes $h(x) \leqslant b$ and $-h(x) \leqslant b$) and rearranging (A.3):

$$-\nabla f(x^*) = J_g(x^*)^\top \mu = \sum_j \mu_j \nabla g_j(x^*) \qquad \text{(A.8)}$$

which, with $\mu \geqslant 0$, implies that the largest decrease in objective cost function value $-\nabla f(x^*) \in \mathcal{K}(\{\nabla g_j(x^*)\}_{j=1}^m)$, where $\mathcal{K}(\{\nabla g_j(x^*)\}_{j=1}^m)$ is the convex cone of active constraints at x^* since $g_j(x^*) < d_j \Rightarrow \mu_j = 0$. That is, any optimal solution must exhibit decreasing objective function inside the convex cone of active constraints.

APPENDIX B

Proof of Theorem IV.11

Theorem B.1 (Temperature and Convex Relaxation). *Assume $g_{ij} > 0$ and losses in (4.20f) are fixed to a predetermined value over the duration of the prediction horizon. If the temperature of line $(i,j) \in \mathcal{E}$ exceeds its limit at time $l + 1$, then the convex relaxation is tight with respect to line (i,j) for all previous time-steps. That is, if $\exists\, l \in \mathcal{M}$ and $(i,j) \in \mathcal{E}$ such that $\Delta T_{ij}[l + 1] > 0$, then adjacency conditions are satisfied and $\theta_{ij}^{+}[\kappa]\, \theta_{ij}^{-}[\kappa] = 0$, $\forall\, \kappa \leqslant l$. Hence, the convex relaxation associated with line (i,j) is tight $\forall\, \kappa \leqslant l$ (i.e. relaxation is locally tight).*

Proof. Let $l + 1$ be the predicted time when line (i,j) exceeds its temperature limit. Pick an arbitrary $\kappa \leqslant l$. Since the RHMPC problem reflects that of a QP problem (with linear constraints), it satisfies the Linearity/Concave Constraint Qualification trivially and the Karush-Kuhn-Tucker (KKT) first-order conditions are therefore necessary conditions for (global) optimality [104]. See Appendix A for an overview of the first-order KKT necessary conditions. The KKT conditions relating variables $\{\theta_{ij}^{+}[\kappa], \theta_{ij}^{-}[\kappa], \theta_{ij}^{\mathrm{PW}}(s)[\kappa]\}$ for any $\kappa \leqslant l$ and $\Delta\hat{T}[l + 1]$ give the following:

$$\theta_{ij}^{+}[\kappa]: \qquad 0 = -\lambda_1 + \mu_1 - \mu_2 - \underline{\mu}_5 \tag{B.1}$$

$$\theta_{ij}^{-}[\kappa]: \qquad 0 = -\lambda_1 - \mu_1 + \mu_2 - \underline{\mu}_6 \tag{B.2}$$

$$\theta_{ij}^{\mathrm{PW}}(s)[\kappa]: \qquad 0 = \lambda_1 + \overline{\mu}_3^{s} - \underline{\mu}_4^{s} + \mu_7^{l}\varphi_{ij,l-\kappa}\alpha_{ij}(s) + \alpha_{ij}(s)\zeta_{ij,\kappa} \tag{B.3}$$

$$\Delta\hat{T}_{ij}[l + 1]: \qquad 0 = 2p_o\Delta\hat{T}_{ij}[l + 1] - \mu_7^{l} - \underline{\mu}_8^{l} \tag{B.4}$$

where

- $\lambda_1 \in \mathbb{R}$ – multiplier related to constraint that couples absolute value and PWL variables in (4.20i);

- $\mu_1 \in \mathbb{R}^{+}$ – multiplier related to upper bound for $\hat{\theta}_{ij}$;

- $\mu_2 \in \mathbb{R}^{+}$ – multiplier related to lower bound for $\hat{\theta}_{ij}$;

- $\overline{\mu}_3^{s} \in \mathbb{R}^{+}$ – multiplier related to upper bound for $\theta_{ij}^{\mathrm{PW}}(s)$;

- $\underline{\mu}_4^s \in \mathbb{R}^+$ – multiplier related to lower bound for $\theta_{ij}^{\text{PW}}(s)$;

- $\underline{\mu}_5 \in \mathbb{R}^+$ – multiplier related to lower bound for θ_{ij}^+;

- $\underline{\mu}_6 \in \mathbb{R}^+$ – multiplier related to lower bound for θ_{ij}^-;

- $\mu_7^l \in \mathbb{R}^+$ – multiplier related to temperature dynamics and $\Delta T[l+1] \leqslant \Delta \hat{T}[l+1]$ in (4.24a).

- $\underline{\mu}_8^l \in \mathbb{R}^+$ – multiplier related to $0 \leqslant \Delta \hat{T}[l+1]$ in (4.24b).

- $\varphi_{ij,l-\kappa} \in \mathbb{R}^+$ – constant based on $\Delta T_{ij}[l+1]$-to-$f_{ij}^{\text{loss}}[\kappa]$ transition (see Remark B.2).

- $\zeta_{ij,\kappa} \in \mathbb{R}^+$ – linear combination of multipliers based on $\Delta T_{ij}[l+1]$-to-$f_{ij}^{\text{loss}}[\kappa]$ transition (see Remark B.2).

Remark B.2 (Relating $\theta_{ij}^{\text{PW}}(s)$ and $\Delta \hat{T}_{ij}$). Given the discrete difference equation for temperature dynamics and ignoring effect of Δd on temperature, it is possible to define $\Delta T_{ij}[l+1]$ in terms of the initial condition $\Delta T_{ij}[0]$, prior losses $\{\Delta f_{ij}[\kappa] = \frac{S_b}{3L_{ij}} f_{ij}^{\text{loss}}[\kappa] - f_{ij}^{\text{loss,lim}}\}_{\kappa=0}^l$, and PWL approximation $f_{ij}^{\text{loss}}[\kappa] = \sum_{s=1}^S \alpha_{ij}(s)\theta_{ij}^{\text{PW}}(s)[\kappa]$, as:

$$\Delta T_{ij}[l+1] = \tau_{ij}^{l+1}\Delta T_{ij}[0] + \frac{S_b}{3L_{ij}}\rho_{ij}\left(\sum_{n=0}^l \tau_{ij}^{l-n}\sum_{s=1}^S \alpha_{ij}(s)\theta_{ij}^{\text{PW}}(s)[n]\right) - \chi_{ij,l}, \quad \text{(B.5)}$$

where $\chi_{ij,l} := \rho_{ij}f_{ij}^{\text{loss,lim}}\sum_{n=0}^l \tau_{ij}^{l-n} > 0$. Combining (B.5) with the constraints $\Delta T_{ij}[l+1] - \Delta \hat{T}_{ij}[l+1] \leqslant 0$, yields the following:

$$\sum_{n=0}^l \varphi_{ij,l-n}\left(\sum_{s=1}^S \alpha_{ij}(s)\theta_{ij}^{\text{PW}}(s)[n]\right) - \Delta \hat{T}_{ij}[l+1] \leqslant \chi_{ij,l} - \tau_{ij}^{l+1}\Delta T_{ij}[0] \quad \forall l = 0, \ldots, M-1$$

where $\varphi_{ij,l-n} := \frac{S_b}{3L_{ij}}(\tau_{ij})^{l-n}\rho_{ij} > 0$ is a fixed scalar. Now, it is straightforward to compute coefficients of KKT multipliers $\mu_7^l \in \mathbb{R}^+$ associated with the above inequailty. That is, define

$$h_l(\theta_{ij}^{\text{PW}}(s)) := \sum_{n=0}^l \varphi_{ij,l-n}\left(\sum_{s=1}^S \alpha_{ij}(s)\theta_{ij}^{\text{PW}}(s)[n]\right),$$

then

$$\frac{dh_l}{d\theta_{ij}^{\text{PW}}(s)[\kappa]} = \begin{cases} \varphi_{ij,l-\kappa}\alpha_{ij}(s), & \text{if } \kappa \leqslant l \\ 0, & \text{else} \end{cases},$$

130

which yields the following first-order KKT conditions for $\theta_{ij}^{\mathrm{PW}}(s)[\kappa]$, $\forall \kappa \leqslant l$:

$$0 = \lambda_1 + \overline{\mu}_3^s - \underline{\mu}_4^s + \alpha_{ij}(s) \sum_{m=\kappa}^{M-1} \mu_7^m \varphi_{ij,m-\kappa}$$

$$= \lambda_1 + \overline{\mu}_3^s - \underline{\mu}_4^s + \alpha_{ij}(s)\varphi_{ij,l-\kappa}\mu_7^l + \alpha_{ij}(s) \sum_{\substack{m=\kappa \\ m \neq l}}^{M-1} \mu_7^m \varphi_{ij,m-\kappa}$$

$$\Rightarrow 0 = \lambda_1 + \overline{\mu}_3^s - \underline{\mu}_4^s + \alpha_{ij}(s)\varphi_{ij,l-\kappa}\mu_7^l + \alpha_{ij}(s)\zeta_{ij,\kappa}, \tag{B.6}$$

where $\zeta_{ij,\kappa} := \sum_{\substack{m=\kappa \\ m \neq l}}^{M-1} \mu_7^m \varphi_{ij,m-\kappa} \geqslant 0$ establishes (B.3).

Lemma B.3. *KKT condition* (B.4) *implies that* $\mu_7^l = \beta \Delta \hat{T}_{ij}[l+1] \geqslant 0$ *for some* $\beta > 0$.

Proof. Consider two cases:

1. $\Delta \hat{T}_{ij}[l+1] = 0$: Then, $0 = -\mu_7^l - \underline{\mu}_8^l \Rightarrow \mu_7^l = \underline{\mu}_8^l = 0$ since $\mu_7^l, \underline{\mu}_8^l \geqslant 0$.

2. $\Delta \hat{T}_{ij}[l+1] > 0$: Then, $\underline{\mu}_8^l = 0 \Rightarrow \mu_7^l = 2p_o\Delta \hat{T}_{ij}[l+1] > 0$ as $p_o > 0$.

Thus, $\underline{\mu}_8^l \equiv 0$ and set $\beta = 2p_o > 0$. The proof is concluded. $\qquad \square$

From the KKT conditions associated with $\theta_{ij}^+, \theta_{ij}^-$, it is straightforward to show that,

$$2\lambda_1 = -\underline{\mu}_5 - \underline{\mu}_6 \leqslant 0. \tag{B.7}$$

This relationship will be used in Lemma B.4 to establish tightness of the convex relaxation of the absolute value constraint (i.e. $\theta_{ij}^+ \theta_{ij}^- = 0$).

Lemma B.4. *If line* $(i,j) \in \mathcal{E}$ *is predicted to exceed its temperature limit, then the absolute value complimentarity relaxation is tight for all previous time-steps. That is, if* $\exists l \in \{0, \dots, M-1\}$ *such that* $\Delta \hat{T}_{ij}[l+1] > 0$ *then* $\theta_{ij}^+[\kappa]\,\theta_{ij}^-[\kappa] = 0$, $\forall \kappa \leqslant l$.

Proof. Let $\Delta \hat{T}_{ij}[l+1] > 0$, choose arbitrary $\kappa \leqslant l$, and consider the following two cases:

1. Suppose $\sum_{s=1}^S \theta_{ij}^{\mathrm{PW}}(s)[\kappa] = 0$, then $\theta_{ij}^+[\kappa] = \theta_{ij}^-[\kappa] = 0$ and $\theta_{ij}^+[\kappa]\,\theta_{ij}^-[\kappa] = 0$.

2. Suppose $\sum_{s=1}^S \theta_{ij}^{\mathrm{PW}}(s)[\kappa] > 0$, then $\exists s \in \{1, \dots, S\}$ such that $\theta_{ij}^{\mathrm{PW}}(s)[\kappa] > 0$, so $\underline{\mu}_4^s = 0$. Using Lemma B.3 and (B.3), and re-arranging gives:

$$0 < \beta \Delta \hat{T}_{ij}[l+1]\varphi_{ij,l-\kappa} \leqslant \beta \Delta \hat{T}_{ij}[l+1]\varphi_{ij,l-\kappa} + \zeta_{ij,\kappa} = -\frac{\overline{\mu}_3^s}{\alpha_{ij}(s)} - \frac{\lambda_1}{\alpha_{ij}(s)}. \tag{B.8}$$

Since $\overline{\mu}_3^s \geqslant 0$ this implies $\lambda_1 < 0$. From (B.7), one or both of $\underline{\mu}_5, \underline{\mu}_6 > 0$, which implies that one or both of $\theta_{ij}^+[\kappa]$, $\theta_{ij}^-[\kappa] = 0$, and hence $\theta_{ij}^+[\kappa]\,\theta_{ij}^-[\kappa] = 0$. Because $0 < \sum_{s=1}^S \theta_{ij}^{\mathrm{PW}}(s)[\kappa] = \theta_{ij}^+[\kappa] + \theta_{ij}^-[\kappa]$, only one of $\theta_{ij}^+[\kappa]$ and $\theta_{ij}^-[\kappa]$ can be zero.

Since κ was arbitrary, it has been proven that for positive temperature overload at time $l+1$, the absolute value relaxation is locally tight for all $\kappa \leqslant l$. $\qquad\square$

Next, the goal is to prove that adjacency conditions are upheld in the relaxed formulation for all time-steps $\kappa \leqslant l$ if $\Delta T_{ij}[l+1] > 0$. Chose arbitrary κ. To improve readability of the following argument, the notation "$[\kappa]$" will be dropped, though all notation is with respect to time-step κ.

Suppose $\theta_{ij}^{\text{PW}}(s) > 0$ for some $s > 1$. Then KKT condition (B.3) has $\underline{\mu}_4^s = 0$ and $\overline{\mu}_3^s \geqslant 0$, and so:

$$\mu_7^l \varphi_{ij,l-\kappa} + \zeta_{ij,\kappa} = -\frac{\lambda_1}{\alpha_{ij}(s)} - \frac{\overline{\mu}_3^s}{\alpha_{ij}(s)} \leqslant -\frac{\lambda_1}{\alpha_{ij}(s)}. \tag{B.9}$$

In order to establish a contradiction, suppose $\theta_{ij}^{PW}(s-1) \in [0, \Delta\theta)$. If $\theta_{ij}^{PW}(s-1) = 0$, then $\overline{\mu}_3^{s-1} = 0$ and $\underline{\mu}_4^{s-1} \geqslant 0$, so (B.3) implies that,

$$\mu_7^l \varphi_{ij,l-\kappa} + \zeta_{ij,\kappa} = -\frac{\lambda_1}{\alpha_{ij}(s-1)} + \frac{\underline{\mu}_4^{s-1}}{\alpha_{ij}(s-1)} \geqslant -\frac{\lambda_1}{\alpha_{ij}(s-1)} > -\frac{\lambda_1}{\alpha_{ij}(s)}, \tag{B.10}$$

where the last strict inequality derives from strict monotonicity of $\alpha_{ij}(s) > 0$ over s, and the guarantee that $\lambda_1 < 0$ from Lemma B.4. This contradicts with (B.9). The proof that $\theta_{ij}^{PW}(s-1) \notin (0, \Delta\theta)$ is similar. Hence, $\theta_{ij}^{PW}(s) > 0 \Rightarrow \theta_{ij}^{\text{PW}}(s-1) = \Delta\theta$. Since κ was arbitrary, adjacency conditions are upheld for all $\kappa \leqslant l$. Thus, the convex relaxation is locally tight for all times prior to a line's predicted temperature exceeding its limit. $\qquad\square$

BIBLIOGRAPHY

BIBLIOGRAPHY

[1] M. Geidl, G. Koeppel, P. Favre-Perrod, B. Klockl, G. Andersson, and K. Fröhlich, "Energy hubs for the future," *IEEE Power & Energy Magazine*, vol. 5, no. 1, pp. 24 – 30, 2007.

[2] F. Borrelli, A. Bemporad, and M. Morari, *Predictive Control for linear and hybrid systems.* 2013.

[3] W. A. Wulf, "Great achievements and grand challenges," *National Academy of Engineering - The Bridge*, vol. 30, pp. 5–10, Oct 2000.

[4] Federal Energy Regulatory Commission, "Grid 2030 - a national vision for electricity's second 100 years," tech. rep., U. S. Department of Energy, July 2003.

[5] M. Geidl and G. Andersson, "Operational and topological optimization of multi-carrier energy systems," *International Conference on Future Power Systems*, 2005.

[6] A. del Real, M. D. Galus, C. Bordons, and G. Andersson, "Optimal power dispatch of energy networks including external power exchange," *IEEE European Control Conference*, vol. 9, 2009.

[7] F. Kienzle, P. Favre-Perrod, M. Arnold, and G. Andersson, "Multi-energy delivery infrastructures for the future," *International Conference on Infrastructure Systems and Services*, December 2008.

[8] W. van Gool, A. Hoogendoorn, R. Kümmel, and H. Groscurth, "Energy analysis and optimization of energy systems," *Intersociety Energy Conversion Engineering Conference*, pp. 1923 – 1928 vol.4, 1989.

[9] H. Groscurth, T. Bruckner, and R. Kümmel, "Modeling of energy-services supply systems," *Energy*, vol. 20, pp. 941–958, Jan 1995.

[10] B. H. Bakken, A. Haugstad, K. S. Hornnes, S. Vist, B. Gustavsen, and J. Røynstrand, "Simulation and optimization of systems with multiple energy carriers," *Conference of the Scandinavian Simulation Society*, May 1999.

[11] S. An, Q. Li, and T. Gedra, "Natural gas and electricity optimal power flow," *IEEE Power and Energy Society Transmission and Distribution Conference and Exhibition*, vol. 1, pp. 138–143, 2003.

[12] B. Bakken, "Energy service systems: Integrated planning case studies," *IEEE Power and Energy Society General Meeting*, Jan 2005.

[13] B. Bakken, H. Skjelbred, and O. Wolfgang, "eTransport: Investment planning in energy supply systems with multiple energy carriers," *Energy*, vol. 32, pp. 1676–1689, Jan 2007.

[14] M. Geidl and G. Andersson, "Optimal power flow of multiple energy carriers," *IEEE Transactions on Power Systems*, vol. 22, no. 1, pp. 145 – 155, 2007.

[15] M. Geidl and G. Andersson, "A modeling and optimization approach for multiple energy carrier power flow," *IEEE PowerTech*, 2005.

[16] F. Kienzle and G. Andersson, "Location-dependent valuation of energy hubs with storage in multi-carrier energy systems," *International Conference on the European Energy Market*, 2010.

[17] M. Arnold, R. Negenborn, G. Andersson, and B. D. Schutter, "Multi-area predictive control for combined electricity and natural gas systems," *IEEE European Control Conference*, Jun 2009.

[18] M. Arnold and G. Andersson, "Decomposed electricity and natural gas optimal power flow," *Power Systems Computation Conference*, 2008.

[19] M. Arnold, R. Negenborn, G. Andersson, and B. D. Schutter, "Distributed predictive control for energy hub coordination in coupled electricity and gas networks," in *Intelligent Infrastructures*, pp. 235–273, Springer, Jan 2010.

[20] M. D. Galus and G. Andersson, "Power system considerations of plug-in hybrid electric vehicles based on a multi energy carrier model," *IEEE Power and Energy Society General Meeting*, 2009.

[21] K. Heussen, S. Koch, A. Ulbig, and G. Andersson, "Energy storage in power system operation: The power nodes modeling framework," *IEEE Power and Energy Society Innovative Smart Grid Technologies Conference*, vol. October, Oct 2010.

[22] T. Krause, G. Andersson, K. Fröhlich, and A. Vaccaro, "Multiple-energy carriers: Modeling of production, delivery, and consumption," *Proceedings of the IEEE*, 2010.

[23] S. Rinaldi, J. P. Peerenboom, and T. K. Kelly, "Identifying, understanding, and analyzing critical infrastructure interdependencies," *IEEE Control Systems Magazine*, vol. 21, no. 6, pp. 11 – 25, 2001.

[24] P. Stluka, D. Godbole, and T. Samad, "Energy management for buildings and microgrids," *IEEE Conference on Decision and Control and European Control Conference*, pp. 5150–5157, Dec 2011.

[25] J. Carpentier and A. Merlin, "Optimization methods in planning and operation," *International Journal of Electric Power and Energy Systems*, vol. 4, pp. 11–18, Jan 1982.

[26] J. Carpentier, "Optimal power flows," *International Journal of Electrical Power and Energy Systems*, vol. 1, pp. 3–15, Apr 1979.

[27] G. Hug-Glanzmann and G. Andersson, "N-1 security in optimal power flow control applied to limited areas," *IET Generation, Transmission & Distribution*, vol. 3, pp. 206 – 215, Feb 2009.

[28] U.S.-Canada Power System Outage Task Force, "Final report on the August 14, 2003 blackout in the United States and Canada: Causes and recommendations," tech. rep., U. S. Department of Energy, Apr 2004.

[29] J. Salmeron, K. Wood, and R. Baldick, "Worst-case interdiction analysis of large-scale electric power grids," *IEEE Transactions on Power Systems*, vol. 241, pp. 96–104, Jan 2009.

[30] D. Bienstock and A. Verma, "The N-k problem in power grids: New models, formulations, and numerical experiments," *SIAM Journal on Optimization*, vol. 20, p. 2352, 2010.

[31] A. Verma, *Power Grid Security Analysis : An Optimization Approach.* PhD thesis, Columbia University, Nov 2009.

[32] A. Pinar, J. Meza, V. Donde, and B. Lesieutre, "Optimization strategies for the vulnerability analysis of the electric power grid," *SIAM Journal on Optimization*, vol. 20, pp. 1786–1810, Feb 2010.

[33] D. Bienstock and S. Mattia, "Using mixed-integer programming to solve power grid blackout problems," *Discrete Optimization*, vol. 4, pp. 115–141, Mar 2007.

[34] B. Carreras, V. Lynch, M. Sachtjen, and I. Dobson, "Modeling blackout dynamics in power transmission networks with simple structure," *International Conference on System Sciences*, Jan 2001.

[35] J. B. Rawlings, "Tutorial overview of model predictive control," *IEEE Control Systems Magazine*, vol. 20, pp. 38–52, June 2000.

[36] D. Mayne, J. Rawlings, C. V. Rao, and P. O. M. Scokaert, "Constrained model predictive control: Stability and optimality," *Automatica*, pp. 789–814, Jan 2000.

[37] A. Bemporad and M. Morari, "Control of systems integrating logic, dynamics, and constraints," *Automatica*, vol. 35, pp. 407–427, Feb 1999.

[38] E. F. Camacho and C. Bordons, *Model Predictive Control.* London: Springer-Verlag, second ed., 2004.

[39] B. Stott and E. Hobson, "Power system security control calculations using linear programming, part I," *IEEE Transactions on Power Apparatus and Systems*, vol. 97, pp. 1713–1720, Oct 1978.

[40] B. Stott and E. Hobson, "Power system security control calculations using linear programming, part II," *IEEE Transactions on Power Apparatus and Systems*, vol. 97, pp. 1721–1731, Oct 1978.

[41] J. Zaborszky, G. Huang, and S. Y. Lin, "Control of reactive power and voltage in emergencies," *Automatica*, vol. 21, pp. 237–246, May 1985.

[42] B. H. Krogh, "Multi-stage rescheduling of generation, load shedding and short-term transmission capacity for emergency state control," *IEEE Transactions on Power Apparatus and Systems*, vol. 102, pp. 1466–1472, May 1983.

[43] B. H. Krogh and P. V. Kokotovic, "Feedback control of overloaded networks," *IEEE Transactions on Automatic Control*, vol. 29, pp. 704–711, Aug 1984.

[44] M. Larsson, D. J. Hill, and G. Olsson, "Emergency voltage control using search and predictive control," *Electrical Power and Energy Systems*, vol. 24, pp. 121–130, Feb 2002.

[45] M. Zima, P. Korba, and G. Andersson, "Power systems voltage emergency control approach using trajectory sensitivities," *IEEE Conference on Control Applications*, vol. 1, pp. 189 – 194 vol.1, 2003.

[46] I. A. Hiskens and B. Gong, "Voltage stability enhancement via model predictive control of load," *Bulk Power System Dynamics and Control VI*, Aug 2004.

[47] I. A. Hiskens and B. Gong, "MPC-based load shedding for voltage stability enhancement," *IEEE Conference on Decision and Control and the European Control Conference*, Dec 2005.

[48] H. Banakar, N. Alguacil, and F. D. Galiana, "Electrothermal coordination part I: Theory and implementation schemes," *IEEE Transactions on Power Systems*, vol. 20, pp. 798–805, May 2005.

[49] N. Alguacil, H. Banakar, and F. D. Galiana, "Electrothermal coordination part II: Case studies," *IEEE Transactions on Power Systems*, vol. 20, pp. 1738–1745, Nov 2005.

[50] B. Otomega, A. Marinakis, M. Glavic, and T. V. Cutsem, "Emergency alleviation of thermal overloads using model predictive control," *IEEE PowerTech*, pp. 201–206, Jun 2007.

[51] J. Carneiro and L. Ferrarini, "Preventing thermal overloads in transmission circuits via model predictive control," *IEEE Transactions on Control Systems Technology*, vol. 18, no. 6, pp. 1406 – 1412, 2010.

[52] P. D. Hines, *A Decentralized Approach to Reducing the Social Costs of Cascading Failures*. PhD thesis, Carnegie Mellon University, Aug 2007.

[53] P. Giselsson and A. Rantzer, "Distributed model predictive control with suboptimality and stability guarantees," *IEEE Control and Decision Conference*, pp. 7272–7277, Dec 2010.

[54] A. Venkat, I. A. Hiskens, and J. Rawlings, "Distributed MPC strategies with application to power system automatic generation control," *IEEE Transactions on Control Systems Technology*, vol. 16, pp. 1192–1206, Jan 2008.

[55] D. S. Callaway, "Tapping the energy storage potential in electric loads to deliver load following and regulation, with application to wind energy," *Energy Conversion and Management*, Jan 2009.

[56] D. S. Callaway and I. A. Hiskens, "Achieving controllability of electric loads," *Proceedings of IEEE*, vol. 99, pp. 184–199, Jan 2011.

[57] K. Clement-Nyns, E. Haesen, and J. Driesen, "Coordinated charging of multiple plug-in hybrid electric vehicles in residential distribution grids," *IEEE Power Systems Conference and Exposition*, Mar 2009.

[58] E. Sortomme, M. M. Hindi, S. D. J. MacPherson, and S. S. Venkata, "Coordinated charging of plug-in hybrid electric vehicles to minimize distribution system losses," *IEEE Transactions on Smart Grid*, vol. 2, pp. 198–205, Dec 2011.

[59] M. D. Galus, R. A. Waraich, and G. Andersson, "Predictive, distributed, hierarchical charging control of phevs in the distribution system of a large urban area incorporating a multi agent transportation simulation," *Power Systems Computation Conference*, Aug 2011.

[60] Z. Ma, D. S. Callaway, and I. A. Hiskens, "Decentralized charging control of large populations of plug-in electric vehicles," *IEEE Transactions on Control Systems Technology*, pp. 67–78, Jun 2011.

[61] L. Gan, U. Topcu, and S. Low, "Optimal decentralized protocol for electric vehicle charging," *IEEE Control and Decision Conference*, pp. 5798–5804, Dec 2011.

[62] S. Stüdli, E. Crisostomi, R. Middleton, and R. Shorten, "A flexible distributed framework for realising electric and plug-in hybrid vehicle charging policies," *International Journal of Control*, Apr 2012.

[63] R. K. Ahuja, T. L. Magnanti, and J. B. Orlin, *Network flows: theory, algorithms, and applications*. Upper Saddle River, NJ, USA: Prentice-Hall, Inc., 1993.

[64] S. Boyd, "Convex optimization of graph Laplacian eigenvalues," in *International Congress of Mathematicians*, pp. 1311–1319, 2006.

[65] A. Bergen and V. Vittal, *Power Systems Analysis.* Pearson Education Taiwan, 2006.

[66] G. Andersson, "Modelling and analysis of electric power systems." Lecture Notes, Aug 2008.

[67] A. Wood and B. Wollenberg, *Power Generation, Operation, and Control.* Wiley-Interscience, second ed., 1996.

[68] C. Grigg, P. Wong, P. Albrecht, R. Allan, M. Bhavaraju, R. Billinton, Q. Chen, C. Fong, S. Haddad, S. Kuruganty, W. Li, R. Mukerji, D. Patton, N. Rau, D. Reppen, A. Schneider, M. Shahidehpour, and C. Singh, "The IEEE reliability test system," *IEEE Transactions on Power Systems*, vol. 14, no. 3, pp. 1010 – 1020, 1999.

[69] A. L. Motto, F. D. Galiana, A. J. Conejo, and J. M. Arroyo, "Network-constrained multiperiod auction for a pool-based electricity market," *IEEE Transactions on Power Systems*, vol. 17, pp. 646–653, Aug 2002.

[70] R. Palma-Benhke, A. Philpott, A. Jofré, and M. Cortés-Carmona, "Modelling network constrained economic dispatch problems," *Optimization and Engineering*, pp. 1–14, Oct 2012.

[71] J. Lee, *A first course in combinatorial optimization*, vol. 36. Cambridge University Press, 2004.

[72] M. Gaggero, M. Parodi, and M. Storace, "Multiresolution PWL approximations," *European Conference on Circuit Theory and Design*, vol. 3, pp. 393–396, Aug 2005.

[73] S. Kundu and I. A. Hiskens, "Hysteresis-based charging control of plug-in electric vehicles," in *Conference on Decision and Control*, pp. 5598–5604, 2012.

[74] J. L. Mathieu, P. N. Price, S. Kiliccote, and M. A. Piette, "Quantifying changes in building electricity use, with application to demand response," *IEEE Transactions on Smart Grid*, vol. 2, no. 3, pp. 507–518, 2011.

[75] P. Kundur, N. J. Balu, and M. G. Lauby, *Power System Stability and Control.* McGraw-Hill Education, first ed., 1994.

[76] IEEE Standard 738, *IEEE Standard for Calculating the Current-Temperature of Bare Overhead Conductors*, 2007.

[77] D. M. Marsh, *The Water-Energy Nexus: a Comprehensive Analysis in the Contex of New South Wales.* PhD thesis, University of Technology, Sydney, Aug 2008.

[78] M. Almassalkhi and I. A. Hiskens, "Optimization framework for the analysis of large-scale networks of energy hubs," *Power Systems Computation Conference*, Aug 2011.

[79] A. Osiadacz, *Simulation and Analysis of Gas Networks*. Gulf, first ed., 1987.

[80] Z. Wang, R. J. Thomas, and A. Scaglione, "Generating random topology power grids," *International Conference on System Sciences*, pp. 183–191, 2008.

[81] J. Ellson, E. Gansner, L. Koutsofios, S. North, G. Woodhull, S. Description, and L. Technologies, "Graphviz open source graph drawing tools," in *Lecture Notes in Computer Science*, pp. 483–484, Springer-Verlag, 2001.

[82] M. Almassalkhi and I. A. Hiskens, "Cascade mitigation in energy hub networks," *IEEE Conference on Decision and Control*, Dec 2011.

[83] M. Almassalkhi and I. A. Hiskens, "Impact of energy storage on cascade mitigation in multi-energy systems," *IEEE Power and Energy Society General Meeting*, July 2012.

[84] M. Almassalkhi and I. Hiskens, "Temperature-based model-predictive cascade mitigation in electric power systems," *IEEE Conference on Decision and Control*, in review, 2013.

[85] M. Almassalkhi and I. Hiskens, "Model-predictive cascade mitigation in electric power systems with storage and renewables part I: Theory and implementation scheme," *IEEE Transactions on Power Systems*, submitted, 2013.

[86] M. Almassalkhi and I. Hiskens, "Model-predictive cascade mitigation in electric power systems with storage and renewables part II: Case-study," *IEEE Transactions on Power Systems*, submitted, 2013.

[87] D. Braess, "Über ein paradoxon aus der verkehrsplanung," *Unternehmensforschung*, no. 12, pp. 258–268, 1968.

[88] D. Mohanty, "Jumbo deaths: It is time to act." *The Indian Express*, Available: http://www.indianexpress.com/news/jumbo-deaths-it-is-time-to-act/1053724/ [Last accessed: 15 May 2013].

[89] L. Bahiense, C. Oliveira, M. Pereira, and S. Granville, "A mixed integer disjunctive model for transmission network expansion," *IEEE Transactions on Power Systems*, vol. 16, no. 3, pp. 560–565, 2001.

[90] S. S. Keerthi and E. G. Gilbert, "Optimal infinite-horizon feedback laws for a general class of constrained discrete-time systems: Stability and moving-horizon approximations," *Journal of Optimization Theory and Applications*, vol. 57, pp. 265–293, May 1988.

[91] W. H. Kwon and D. G. Byun, "Receding horizon tracking control as a predictive control and its stability properties," *International Journal of Control*, vol. 50, pp. 1807–1824, May 1989.

[92] M. Thomas, J. Kardos, and B. Joseph, "Shrinking horizon model predictive control applied to autoclave curing of composite laminate materials," *American Control Conference, 1994*, vol. 1, pp. 505 – 509 vol.1, 1994.

[93] F. Metzger (of Kinder-Morgan). Personal communication, November 4th 2011.

[94] B. Lesieutre, D. Molzahn, A. Borden, and C. L. Demarco, "Examining the limits of the application of semidefinite programming to power flow problems," *Allerton Conference*, vol. 1, pp. 1492–1499, Oct 2011.

[95] Operations Support Division, "Manual on transmission operations," tech. rep., PJM, Dec 2012.

[96] H. Chavez and R. Baldick, "Inertia and governor ramp rate constrained economic dispatch to assess primary frequency response adequacy," *International Conference on Renewable Energies and Power Quality*, Mar 2012.

[97] T. J. Overbye, X. Cheng, and Y. Sun, "A comparison of the AC and DC power flow models for LMP calculations," *Hawaii International Conference on System Sciences*, Jan 2004.

[98] R. M. Hermans, M. Almassalkhi, and I. A. Hiskens, "Incentive-based coordinated charging control of plug-in electric vehicles at the distribution-transformer level," *American Control Conference*, Sep 2012.

[99] D. P. Bertsekas, *Nonlinear Programming*. Belmont, MA, USA: Athena Scientific, 1999.

[100] N. Z. Shor, *Minimization methods for nondifferentiable functions*. Berlin: Springer, 1985. Translated from Russian.

[101] D. Angeli, R. Amrit, and J. Rawlings, "On average performance and stability of economic model predictive control," *IEEE Transactions on Automatic Control*, vol. 57, no. 7, pp. 1615–1626, 2012.

[102] V. M. Zavala and A. Flores-Tlacuahuac, "Stability of multiobjective predictive control: A utopia-tracking approach," *Automatica*, pp. 2627–2632, Jul 2012.

[103] G. Hug-Glanzmann and G. Andersson, "Decentralized optimal power flow control for overlapping areas in power systems," *IEEE Transactions on Power Systems*, vol. 24, pp. 327 – 336, Feb 2009.

[104] M. S. Bazaara, H. D. Sherali, and C. M. Shetty, *Nonlinear Programming*. Wiley-Interscience, third ed., 2006.